The University Of Sheffield.

Imaging Based Studies of Premixed Flame Propagation in Tubes

Houshi Jiang

Combustion and Flow Diagnostics Research Group

Department of Mechanical Engineering

This thesis is submitted to the University of Sheffield for the degree

of Doctor of Philosophy, 2020

DECLARALATION

I declare that this thesis has been composed by myself and it has not been submitted in any previous application for a degree at University of Sheffield or other university or institute of learning.

ABSTRACT

The dynamics of flames occurring in a confined space represent a typical combustion process in an internal combustion engine, as well as the process of flame acceleration and the transition from deflagration to detonation in the development of detonation waves. Therefore, these dynamics have significant applications in the areas of combustion engineering and explosion safety. Due to a global desire for clean energy resources—and because combustible gases are clean and come from a wide range of sources—these gases are beginning to play an indispensable role in industrial modernisation and in people's daily lives. Hydrogen, especially, can be produced using renewable electricity such as offshore wind power. This increases the availability of hydrogen resources and reduces their cost.

This research will major on the hydrogen effects of premixed flame propagation in a confined space: a tube. It will utilise optical measurement methods to investigate how the dynamic characteristics of premixed flame propagation change, within a tube. The experiment provides a safe and controlled way to understand the process of flame propagation. The originality of this research comes from studying how hydrogen affects the flame propagation interaction in a classic hydrocarbon mixture of methane/air, in both horizontal and vertical tubes. Another innovation is that of applying two different optical measurement methods (flame chemiluminescence and schlieren imaging) at the

same time, to capture both flame chemistry and flame flow.

First, the interesting interaction between the C_2^* emissions and pressure, with hydrogen addition, was found in the horizontal tube. The measured C_2^* emissions had similar fluctuations with the measured pressure, as the flame traversed down the tube. The results indicated a coupling interaction between the C_2^* flame chemiluminescence and the pressure.

Second, hydrogen concentration, affecting flame speed at the second stage of flame propagation in a vertical tube, was also discussed. The flame propagation speed was faster, with higher hydrogen concentrations, at the same equivalence ratios in fuel-rich conditions. The ratio of two oscillation gradient stage (oscillation gradient stage to the initial gradient stage), decreased linearly as the hydrogen concentration increased.

Finally, to develop the mechanisms of flame formation, schlieren imaging techniques were applied at flame propagation in a square tube. Following the results of the schlieren images and pressure signals, periodic propagation characteristics were observed around the middle length of the tube. Each cycle included a flat or curved flame front, a cellular or cells flame front, two near-boundary sides of the tulip flame, a flat or curved flame at the front again, a cellular or cells flame at the front again and a tulip flame in the middle of the tube.

ACKNOWLEDGEMENTS

I must firstly express my immense appreciation for my supervisor Prof Yang Zhang for allowing me to study under him and for his continuous guidance and encouragement over the years. I am also extremely grateful for the things that he has taught me outside the research arena. My gratitude also goes to my second supervisor Dr Robert Woolley for his additional support.

Many thanks go to the department technician Mr. Oliver Cooper, who always helped me solve rig issues. I am also grateful to my friend and colleague Mr Nazrein Amaludin for his support regarding both my experiment and my life and to Mr Abdullah Alsharif for his work on my experiments. To all the colleagues in my research group—Jiansheng Yang, Hussain Saeed, Paco Carranza Ch, Zhen Ma, Shuaida Ji, Lukai Zheng, Yiran Wang, Hangxu Zhou, Yufeng Lai, Xiao Wang, Ahmad Fuad, Ahmad Albadi, Muyi Pan, Yuchen Zhang, Jing Zhang and Xuanqi Liu—thank you for your helpful comments on my research.

Finally, I must express my greatest thanks to my wife Jue Yan and my parents, who always support and encourage me in everything I do. I could neither have come this far nor achieved what I have without the tremendous support of my wonderful family.

PUBLISHED WORK

1. **Houshi Jiang,** Amaludin N.A, Woolley, R and Yang Zhang, "Premixed Methane/Air/Hydrogen Flame Oscillations in Horizontal Open-End Tubes", in 27th International Colloquium on the Dynamics of Explosions and Reactive Systems, Beijing, CHINA, 2019. Oral Presentation.

LIST OF CONTENTS

LIST OF FIGURES

LIST OF TABLES

NOMENCLATURE

Symbol	Definition
CCD	Charge-coupled device
CMOS	Complementary metal-oxide semiconductor
CFA	Colour filter arrays
RGB	Red, Green, Blue
HSV	Hue, Value, Saturation
ISO	International Organization for Standardization
JPEG	Joint Photographic Experts Group
h	Planck constant
ν	frequency of the generated photon
R^*	excited radical
OH^*	OH radical chemiluminescence
C_2^*	C_2 radical chemiluminescence
CH^*	CH radical chemiluminescence
RT	Rayleigh-Taylor
Le	Lewis number
α	thermal diffusivity
D	mass diffusivity
DDT	deflagration to detonation

PIV	particle image velocimetry
LIF	laser-induced fluorescence
LDV	laser doppler velocimetry
fps	Frame per second
α	conversion rate, refer to calculate intensity, for Equation 3.1 to 3.11
f	frequency
FFT	fast Fourier transform
ϕ	Equivalence ratio
R_H	Hydrogen concentration
λ	wavelength
T	temperature.
ε	Emissivity
CH_4	Methane
C_3H_8	Propane
$V_{C_3H_8}, V_{O_2}, V_{air}$	Volume of the fuel (C_3H_8), Oxygen, air.

1 CHAPTER ONE: INTRODUCTION

1.1 Motivation

The dynamics of flames occurring in a confined space represent a typical combustion process in an internal combustion engine, as well as the process of flame acceleration and the transition from deflagration to detonation in the development of detonation waves. Therefore, these dynamics have significant applications in the areas of combustion engineering and explosion safety. Due to a global desire for clean energy resources—and because combustible gases are clean and come from a wide range of sources—these gases are beginning to play an indispensable role in industrial modernisation and in people's daily lives. Hydrogen, especially, can be produced using renewable electricity such as offshore wind power. This increases the availability of hydrogen resources and reduces their cost. Hydrogen production also offers the advantage of low emissions (Benjamin 2019). It is thus increasingly vital to gain a better understanding of hydrogen.

Hydrogen is one of the typical combustible gases; the others include carbon monoxide, methane and propane (Airtest 2008). Due to these gases' high risk of leakage, combustion and explosion, it is necessary to take appropriate measures to prevent disasters—as well as to mitigate the damage and reduce the loss of life and property that can be caused by explosions (Xiao et al. 2013). Combustible gases normally travel

through pipelines in industrial applications. Worldwide, the difficulty of controlling combustible gases causes major fires and explosions every year. In one of the earliest studies of premixed flame propagation in a confined space, Mallard and Le Chatelier (1883) ignited flames in tubes to examine the problem of coal mining explosion accidents. The images were later captured using photographic techniques (Ellis 1928).

Photographic techniques are important methods for optical diagnostics; they can provide a non-contact method for continuous monitoring of the flame. During combustion, high-speed cameras can capture light emissions from the excited species that are formed during chemical reactions, known as flame chemiluminescence. This can provide useful information without disturbing the flame. Additional parameters from the captured images—such as temperature, flame speed and flame dynamics—can be also be further analysed.

In terms of applications, premixed flame propagation is always one of the main research topics concerning combustion and explosion. This is due to the complexity of premixed combustion. Although early research mainly aimed to eradicate coal mine explosions, it also provided fundamental knowledge of flame propagation (Mallard & Chatelier 1883). The rapid development of the engine and of rocket propulsion greatly contributed to follow-up studies on flame propagation, from which many new experimental technologies and types of equipment were developed. A significant

number of new flame phenomena during propagation, such as the tulip flame, were also revealed. Tulip flame is a special phenomenon that the finger-shaped flame bulging towards the unfired gas would suddenly reverse. Dunn-Rankin (1998) proposes that the tulip flame may be the product of joint actions among different mechanisms, which means that the tulip flame is actually a combination of flame propagation processes. Xiao et al. (2013) suggest that the pressure wave, which is induced by the flame, touches the shell surface and plays a determining role in the process of deformation in the tulip flame. Clanet and Searby (1996) divided the propagation process of premixed flame in a half-opened end pipeline into four characteristic stages: 1) semi-spherical (spherical) expansion that is not affected by the wall, 2) finger-shaped flame with exponential growth, 3) flame contacting the shell surface and 4) the classic tulip deformation found in a closed pipe. Xiao et al. (2013) discovered significant deformation of the tulip flame, in premixed hydrogen/air flames, and defined this as the fifth stage of tulip formation: after the initial tulip flame formation, the classic tulip flame front will continue to grow, finally forming the secondary tulip structure. However, a reliable prediction model for flame propagation—one that includes the mechanism of tulip flame formation—has yet to be established.

Therefore, this research will major on the hydrogen effects of premixed flame propagation in a confined space: a tube. It will utilise optical measurement methods to investigate how the dynamic characteristics of premixed flame propagation change,

within a tube. The experiment provides a safe and controlled way to understand the process of flame propagation. The originality of this research comes from studying how hydrogen affects the flame propagation interaction in a classic hydrocarbon mixture of methane/air, in both horizontal and vertical tubes. Another innovation is that of applying two different optical measurement methods (flame chemiluminescence and schlieren imaging) at the same time, to capture both flame chemistry and flame flow.

1.2 Aim and Objectives

The aim of this thesis is to investigate how hydrogen concentration changes affect the methane/air/hydrogen mixture's flame propagation behaviour in a tube. The experiment utilises high-speed optical measurements. This was achieved via a set of processes, including: verification work for the flame chemiluminescence method, applying the method to establish the connection of flame dynamics, then verifying the established connection through different tube conditions and, finally, combining the two optical measurement methods to be further explored. The main objectives of this research are:

1. To verify the flame chemiluminescence method needs, as well as to investigate the relationship between the camera sensor and flame chemiluminescence. To develop the connection between camera sensor spectral sensitivity and the image colour model.
2. To apply the method developed, two typical hydrocarbon fuels, C_3H_8 and CH_4,

are compared to investigate flame behaviour on a Bunsen burner. The method used to utilise the intermediate products (which are CH^* and C_2^* chemiluminescence) produced during the combustion process.

3. To establish the impact of flame chemistry (in this case used C_2^* chemiluminescence to present) and pressure through experimenting with flame propagation in a horizontal tube, adding specific amounts of hydrogen.
4. To develop the hydrogen concentration effects of flame propagation in a vertical tube through multi condition experiments, showing how the experimental evidence of hydrogen concentration influences flame speed and pressure of the propagated flame.
5. To compare the flame chemistry of calculated C_2^* chemiluminescence emissions on oscillating flame, to establish the effects of different hydrogen concentrations.
6. To investigate the impact of flame shape on flame oscillation, via the observed schlieren imaging.

1.3 Thesis outline

This thesis is comprised of eight chapters, including an introduction, a literature review, the methodology applied, four test cases and conclusions. These are followed by a list of references and the appendices.

Chapter ONE introduces the motivation and objectives of this work, and the thesis outline.

Chapter TWO is a literature review of the most important topics related to this work. The key subjects are: the conception of combustion and flame, digital imaging processing, chemiluminescence based on digital imaging processing and flame propagation in tubes.

Chapter THREE verifies the methodology that was used in this thesis. Includes schlieren image system and image colour-based flame chemiluminescence measurement system. In this chapter, the connection between camera sensor spectral sensitivity and the image colour model has been developed.

Chapter FOUR presents a test case of the flame chemiluminescence technique on two different typical hydrocarbon fuel (methane and propane) cases. It applies premixed flames using a Bunsen burner, which provides fundamental knowledge regarding calculated C_2^* chemiluminescence and its relation to flame chemistry conditions.

Chapter FIVE presents a test case of flame propagation in a horizontal tube. The fluctuations between the measured C_2^* emissions with the measured pressure are also proven.

Chapter SIX presents a second test case of flame propagation, in a vertical tube. The experimental work regarding the influence of hydrogen concentrations on the flame speed of propagated flames is discussed. Fluctuations between the measured C_2^* emissions, with the measured pressure, were also discussed.

Chapter SEVEN presents a test case of the flame propagation in a horizontally placed square tube. Two different imaging methods (flame chemiluminescence and the schlieren imaging method) were applied, the correlation between fluctuations of measured C_2^* emissions and measured pressure was discussed.

Conclusions were drawn in **Chapter EIGHT** and summaries of the present study. The recommendations of potential future work are slow present in this chapter.

2 CHAPTER TWO: LITERATURE REVIEW

2.1 Conception of Combustion and Flames

2.1.1 History of Combustion

For much of recorded history, people believed that the burning of material depended on a special substance, referred to as 'phlogiston' (Victor 2016). Phlogiston was believed to be comprised of small flame particles, which were key to combustion. In the mid-eighteenth century, however, the French chemist Antoine Lavoisier and the Russian scientist Mikhail Lomonosov carried out combustion experiments that challenged the prevailing theories. They hypothesised that combustion relied on oxygen, resulting in the oxygen theory of combustion (Kanury 1975).

In the early nineteenth century, scientists used thermochemistry and thermodynamics to discover the features of combustion. These included the heat of combustion, the temperature of adiabatic combustion and the balance components of combustion products. In 1842, Joule proved that 'heat' is not a product, but an energy state. In 1855, Robert Bunsen developed an experiment to successfully measure flame temperature and speed. Ernest-François Mallard and Le Chatelier built the first flame propagation model and studied flame propagation (1883). In 1900, David Chapman and Émile

Jouguet identified the difference between deflagration and detonation and calculated the speed of explosion (Jarosinski, J. and Veyssiere, B. 2009). At the beginning of the twentieth century, the Soviet chemist Nikolay Nikolayevich Semyonov and the American chemist Gilbert Newton Lewis found that reaction kinetics are important factors that influence the burning rate (Ptáček, P. 2018). In the 1920s, scientists Yakov Borisovich Zeldovich, Frank Kamenetzki and Lewis discovered that the burning phenomenon is a reaction between chemical kinetics and physical factors, such as heat and mass transfer. This is true whether it is in the state of being on fire, during flameout, during propagation or in a slow combustion and detonation state (Kanury 1975).

Due to the development of the aviation and aerospace technology in the 1940s and 1950s, combustion research rapidly expanded from general machinery into jet engines, rockets and spacecraft head ablation. At that time, Hungarian-American Theodore von Kármán and Chinese scientist Qian Xuesen proposed studying combustion using continuum mechanics methods; they developed the terminology ‘chemical fluid mechanics’. Further quantitative analyses on the problems of laminar and turbulent combustion, ignition, flame stabilisation and combustion oscillation were conducted, employing viscous fluid mechanics and the boundary layer theory (Jianfeng, P. et al, 2010). Since the mid-1970s, the application of laser technology has allowed for measuring speed, temperature and the concentration of gases and particles in the process of burning. This research has deepened the understanding of combustion

phenomena.

2.1.2 Diffusion and Premixed Flame

Diffusive combustion is a process in which fuel and an oxidising agent are added to a combustion chamber and mixed together during combustion. The chemical reaction is a quick process in a combustion chamber at a high temperature, yet mixing the two substances takes longer. Therefore, it is the duration of the mixing that controls the combustion velocity; this is the basic quality of diffusive combustion.

According to the combustion theory proposed by Forman A. William in 1985, a diffusion flame can be defined as a flame that is non-premixed, almost isobaric and in a quasi-steady state (William 1985). The diffusion flame has a wide application in combustion equipment, such as boilers and turbines. This is due to its inherent advantages, including advantages on the security side—such as the lack of tempering (fuel is not premixed with air or oxidant before ignition, hence there is no chance of tempering happened), steadiness (only flow rate needed to be controlled) or the need to premix the fuel and oxidising agent—as well as a wide scope of operation (William 1985).

Mixing combustible gas with an oxidising agent before ignition is called 'premixed

combustion'. Premixed combustion is widely used in many industrial applications such as aero engines, gas turbines and industrial energy supply boilers. The combustible gas mixes with air or an oxidising agent and is then ignited; the flame will spread quickly and accelerate to the unburned mixture. The premixed gas propagates from the ignition source to the unburnt gas. This forms a combustion wave and, after the process of acceleration, the combustion wave may lead to detonation under certain conditions (Liberman et al. 2012).

Premixed combustion involves flame propagation, flame acceleration and pressure wave interactions. The premixed flame in pipelines usually undergoes typical processes such as ignition, laminar flame, disturbance flame, the transformation from laminar to turbulent flow and even detonation (Xiao et al. 2013).

2.1.3 Laminar and Turbulent Flame

Premixed flame is the most basic combustion phenomenon. It can be classified as either laminar flow or turbulent flow, according to the combustion mechanism (Clavin 1985). Laminar premixed flame is well understood as a premixed combustible mixture ignited by a light source, which then forms a flame layer that can separate the combustion products or unburned gas. Combustion in the laminar flame state is steady, due to the low combustible mixture flow. The surface of the flame is smooth. By means of heat

conduction, molecular diffusion, and an activation centre, generally, a thin flame layer between the flame surface and unburned combustible mixture. (The laminar flame layer is typically smaller than 1 mm). This thin flame layer keeps the flame propagate. The movement of the flame front in the laminar burning of premixed gas is mainly caused by two processes: the transfer of heat in the reaction zone to the fresh mixture, and heat being transferred from the reaction zone—which indicates the outcome of the interaction between thermal conductivity and diffusion from chemistry reaction zone. (Wang 2006).

The Reynolds number can also be used to determine whether the flow is laminar or turbulent. A laminar flame or flow has a small Reynolds number (typically below 2100 in pipeline). A variation in flow state can significantly influence the combustion process. When the velocity of the combustible mixture or the flow area and the flow increases, the fluid will produce many fluid vortexes of different sizes. These rotate and move in random ways. In the process of flow, a vortex will pass through the streamline and create a disturbance on all sides. The surface of the flame is deformed then flame surface becomes thicker and shorter, and makes noise. This is called a turbulent flame (Ashurst 1994).

Due to improved experimental methods and increased computational ability, combustion researchers have developed the area from laminar combustion to turbulent

combustion. The combustion process of various combustion devices often occurs under such turbulent flow conditions in practical engineering, such as in aero engines and gas turbines, etc.

2.2 Digital imaging processing

2.2.1 Digital Camera Sensor Types

The sensor is a device that converts optical images into electronic signals; it is the heart of the digital camera. The sensor technology determines the overall development level of the digital camera. There are currently two types of sensor: the charge-coupled device (CCD) and the complementary metal-oxide semiconductor (CMOS). Both CCD and CMOS use light-sensitive elements as the basic means of capturing images, and the core of each sensor is a photodiode. This diode can generate a current after receiving light, and the current's intensity corresponds to the intensity of the light.

Willard Sterling Boyle and George E. Smith first invented the CCD sensor in 1969, at Bell Laboratories in the United States—an invention for which they won the Nobel Prize in Physics in 2009. CCD replaces traditional film with sensors made from high-sensitivity semiconductor material. This converts light into an electric charge; converts this charge into a digital signal, via an analogue-to-digital converter chip; and then

sends the electric charge signal to a storage medium. The basic working principle of a CCD sensor is that light illuminates each pixel to generate a charge, which accumulates. Since the CCD has only one signal output port, the charge of each pixel needs to be transferred serially from pixel to output port. Finally, the charge is converted into a voltage, and the voltage is amplified and then converted to obtain an image. Compared with traditional filming methods, CCDs are closer to how the human eye works. It differs, however, in that the retina of the human eye is composed of rod cells responsible for light intensity sensing and cone cells for colour sensing. There are many indicators for evaluating the quality of a CCD sensor, such as the number of pixels, the CCD size and the signal-to-noise ratio. The number of pixels and the size of the CCD are the most important indicators. The number of pixels refers to the number of photosensitive elements on the CCD. Pictures can be understood as consisting of many small dots, with each dot a pixel. The greater the number of pixels, the sharper the picture. However, increasing the number of CCD pixels to obtain better image quality will inevitably lead to an increase in the manufacturing cost of the CCD and a decrease in the rate of qualified products.

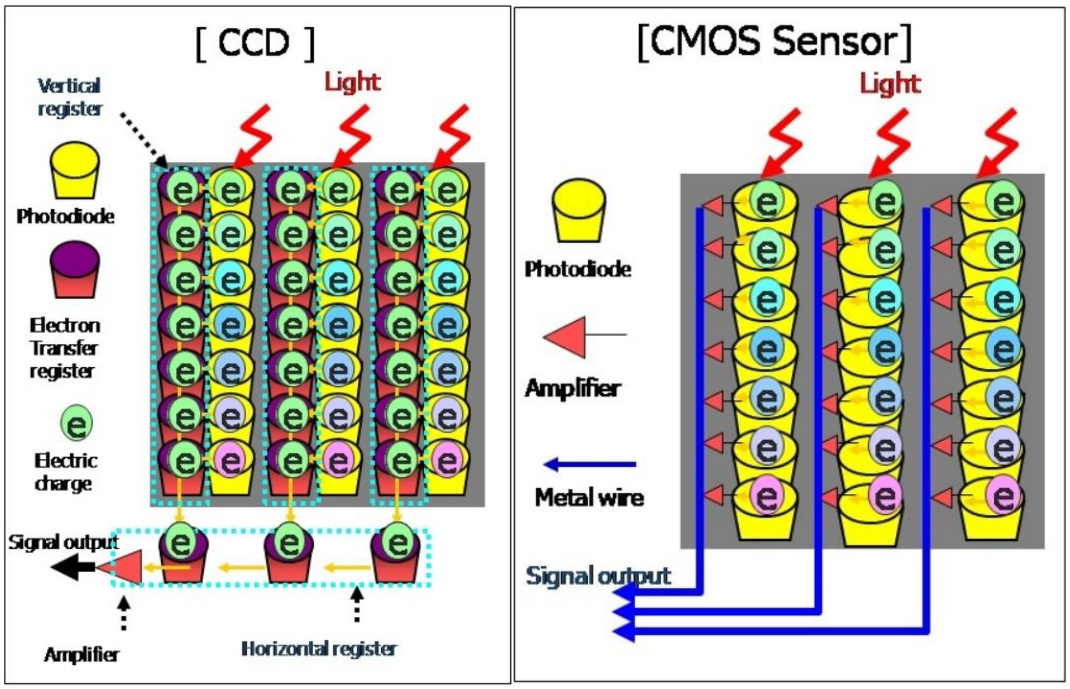

Figure 2-1 CCD sensor (left); CMOS sensor (right) (Siniša Kekez 2018).

To tackle problems such as cost, a CMOS sensor with lower power consumption and high integration has been developed. The core of the CMOS sensor is a photodiode and the photoelectric information conversion function of CMOS is similar to that of CCD. However, the other components lead to a difference in information transmission after photoelectric conversion. As shown in Figure 2-1, CMOS image sensors are a class of active pixel sensors that use CMOS semiconductors. There are corresponding circuits near each photoelectric sensor to directly convert light energy into voltage signals. Unlike CCD, it does not involve a digital signal charge. Due to the continuous improvement of CMOS technology, CMOS has the advantages of a faster output information rate, of lower power consumption, of a small size and light weight, of a low cost and of being a simpler way to read information. As the cost of industrial production is lower than CCD, digital cameras using CMOS as sensors are currently

flooding the market. Sony, a major digital camera manufacturer, discontinued its production of CCD digital cameras in 2017.

2.2.2 Colour Filter Array

Each pixel on a digital camera has a light sensor that measures the brightness of light. Since the photodiode is a device that supports just one single colour, it cannot distinguish between different wavelengths of light. Digital camera engineers thus installed a set of mosaic colour filters called colour filter arrays (CFA), to allow the sensor to distinguish the three basic colours of red, green and blue that make up visible light. The CFA filters light according to the wavelength range, so that the individual filtering intensity includes information about the colour of the light.

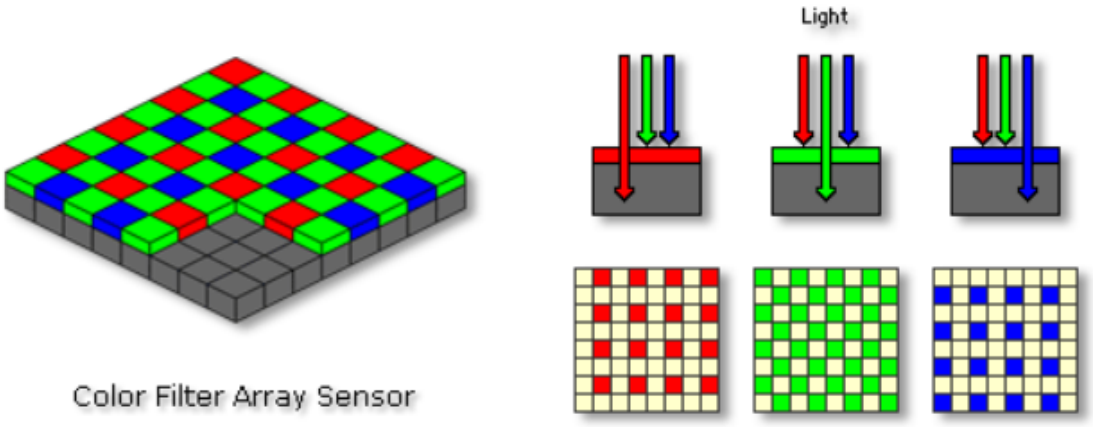

Figure 2-2 Colour filter array sensor.

There are many kinds of colour filter arrays. The most widely used is the Bayer format filter array, which meets the GRBG rule stating that the number of green pixels is twice

the number of red or blue pixels. This is because the peak of the human eye's sensitivity to the visible light spectrum lies in the middle—the band that corresponds to the green spectral component. The other types of colour filter arrays, such as the RGBE filter, RYYB filter and RGBW Bayer, have different purposes.

2.2.3 Colour Model

Figure 2-3 shows the RGB colour space that represents colours by using a unit of length of the cube. Black, blue, green, cyan, red, yellow and magenta are located in the eight vertices of the cube respectively. Black is usually regarded as the origin point of the three-dimensional rectangular coordinate system, and red, green and blue are located in the three axes respectively. The value scope for each parameter of R, G or B is 0 - 255. The parameter value is also known as the three-colour coefficient, base colour coefficient or colour value. It can be calculated by being divided by 255 and then being normalised between 0 and 1.

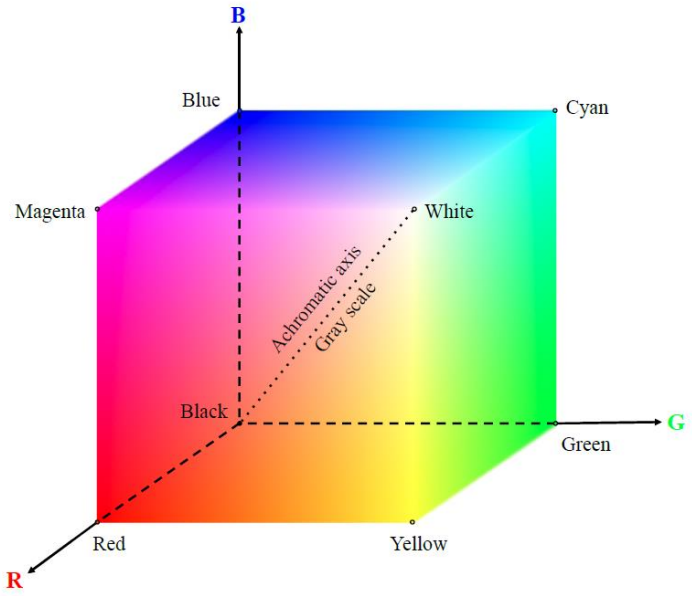

Figure 2-3. 3D representation of the RGB colour model (Gonzalez 2008).

RGB and HSV (hue, value, saturation) are two different representational approaches to colour space. The values of R, G and B have no direct relation to the three attributes of colours. HSV uses these three attributes—hue, saturation and value—to represent colours, and this colour model faces visual perception. HSV is more suitable for image processing.

Figure 2-4 shows that the HSV colour space model corresponds to a conical subset in the cylindrical-coordinate system. The top surface of the cone corresponds to V=1. It contains three surfaces of R=1, G=1 and B=1 in the RGB model. Hue is decided by the rotation angle around the value axis. The red colour corresponds to 0°, the green colour corresponds to 120° and the blue colour 240°. In the HSV colour model, each colour has a gap of 180° to its complementary colour. The saturation is valued from 0 to 1. At

the top point of the cone (the origin point), V=0, yet H and S have no definitions, so they represent the colour black. At the central point of the top surface of the cone, S=0, V=1, yet H has no definition, so it represents the colour white. It also represents the colour grey that becomes dimmer from the point to the origin point; that is to say, the grey colour is at different grey levels.

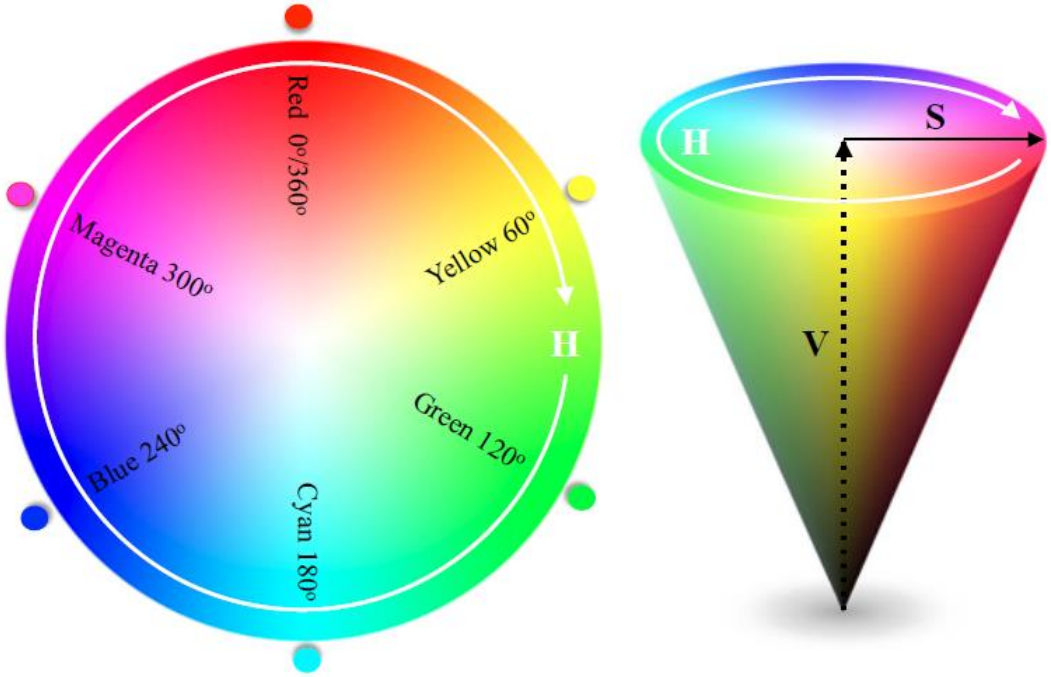

Figure 2-4. The HSV model (Gonzalez 2008).

2.2.4 Exposure Control

An aperture is the part of a camera lens that is used to control the amount of light accessible to the camera sensor. When taking a picture, the first threshold for light to enter the camera sensor is through the lens aperture. The larger the opening in the

aperture, the greater the amount of light is available to the camera sensor. The aperture is represented as an F+ number, and the smaller the F number, the larger the aperture opening—as illustrated in Figure 2-5.

Figure 2-5. Example of Aperture.

Shutter speed is also an important parameter for digital cameras. The shutter speed in the camera indicates how long the shutter remains open, which controls the exposure time. In addition to changing the exposure, the shutter speed can also change the form of motion. High-speed shutters can be used to freeze fast-moving objects, such as when shooting sports. Slow shutters can blur objects and are often used to produce artistic effects. A high-speed shutter means a short exposure time, while a slow shutter means a long exposure time. For shooting flames, the high speed of flame propagation in a tube requires a much shorter exposure time than a stable burning Bunsen flame, to

ensure all details can be tracked.

2.2.5 Camera Noise

Camera noise generally refers to tiny dots created when light passes into the camera sensor and is then converted into signal. Noise can be generated by several causes. For example, noise from electrical signals is caused by the sensor generating more noise as the sensitivity of the image sensor (ISO) increases. This kind of noise is coloured and will affect the picture details.

During long exposures, the sensor will heat up due to poor heat dissipation and cause thermal noise. This kind of noise generally takes the form of bright dots and will be amplified during post-processing. For CMOS sensors, the impact of high ISO noise is far greater than the long-term exposure. Thermal noise can be eliminated by giving the sensor a short break to allow for heat dissipation.

Image noise is also generated by compressing images using the JPEG format. Images in this format still look natural after reducing their size, and special methods can be used to reduce the image data. Units of 8 × 8 pixels are resized and noise occurs at the edge of the 8 × 8 pixel blocks; this type of noise generated by JPEG compression is called block noise as a result. The image noise is more obvious, the greater the

compression ratio. Although the noise is invisible when the image size is reduced, it becomes apparent as soon as colour compensation is performed. Block noise can be solved by using the highest possible image quality or recording the image using methods other than the JPEG format.

There are three common storage formats for digital cameras, each of which has different characteristics. The RAW format is the raw data that is directly obtained by the camera sensor and is unique to digital cameras. RAW files require the largest storage space but offer more shades of colour and the highest level of image detail. However, the RAW format requires special software to access the files. JPEG is a lossy compression format, with the amount of the image quality lost depending on the compression ratio. The TIFF format is a non-compression format, with a similar file size to RAW, and it also maintains the maximum amount of colour and image details. TIFF can be used for publishing and printing, and is suitable for large-format printers to produce high-quality images.

2.2.6 Applications Based on Digital Image Processing

More information about flame can be obtained through digital flame images, which reveal more than can be seen by the human eye. The main advantages of digital images are that they can show the shape, brightness, and colour of the flame—as well as obtain

information for each pixel by using powerful computer processing abilities to provide quantitative analyses.

2.2.6.1 Flame Shape

Research on flame shape primarily includes obtaining the flame edge and geometric parameters of contour extraction through edge detection technology. By combining the separated flame layer technology with robust estimation, Marques, J.S. & Jorge, P.M. (2000) extracted the edge of the flame and obtained the flame shape. This technology was tested in a power plant boiler. Zheng (2018) used digital image processing technology and the optical radiation theory to detect the edge of the flame and successfully extracted the flame contour. The flame edge extraction separates flame from the digital image, focusing the subsequent extraction and processing of flame information on just the flame itself—rather than extraneous information. As a consequence, it improves the processing efficiency and relevance.

Hernandez, R. & Ballester, J. (2008) has also measured the geometric parameters of flame. Based on judging the flame range by means of the strength function, he achieved the extraction of the flame edge and the measurement of the geometric parameters. These include the flame length, the maximum width, the centre of mass, the geometric centre, the direction and the extension angle.

2.2.6.2 Flame Brightness

Research on flame brightness refers to the study of overall average brightness and of a single pixel of brightness in the flame image. As an important characteristic of the flame, flame brightness plays a vital role in flame detection because it can determine the presence of flame and evaluate the stability of combustion.

A number of studies have explored how imaging technology can enhance flame research. For example, Intajag, S. et al. (2009) used the characteristics of colour images to adopt the method of multi-channel brightness threshold value and combined it with a neural network to judge the presence of flame. Marbach et al. (2006) developed the system of automatic time-domain flame detection, using the principle of luminance threshold. Wei et al. (2003) extracted the mean value and variance of the flame brightness from the flame image. Wei also evaluated combustion stability by judging the brightness of the flame front and combining the figure with the neural network.

2.2.6.3 Flame Colour

Through colour analysis of the flame image, Huang et al. (1999) suggest that the colour distribution of the diffusion combustion flame and the premixed combustion flame are different. The flame image can be used to indicate the production of carbon soot and

free radicals in the flame, which is caused by the RGB channel value (Huang, H. W., et al. 2012). As for the ratio of channel B to G, it correlates with the combustion equivalence ratio (Huang, H. W., & Zhang, Y. 2011).

In the principal component analysis of the flame image, Sbarbaro et al. (2003) show that the first principal component of the flame image's channel values correlates with the combustion equivalence ratio. Louër, D. & Langford, J.I., (1988) uses monochromatic and decomposed images of R, G and B from the flame colour image to measure the particles' radiation parameters—including emissivity, absorption coefficient and scattering coefficient—in the coal-fired boiler flame.

2.2.6.4 Flame Temperature

For flame which produced soot, the most important achievement in image colour research is the measurement of the spatial distribution of flame temperature via the two-colour method. Huang et al. (2000) achieved continuous measurement of the flame temperature distribution by adopting the two-colour method and presenting temperature distribution with the colour map. Their research was compared to thermocouple measurements, to demonstrate accuracy and applicability. Ma (2016) detected the local temperature of flame propagation in a tube utilising a single fibre; this proved the possibility of detecting the whole flame temperature using a single fibre. The details of

Ma's method are shown in Appendix 10.1 which was applied but not succussed to this thesis due to technical reason.

2.3 Chemiluminescence Based on Digital Image Processing

2.3.1 Introduction to Chemiluminescence

Pre-combustion reactants are a mixture of fuel and air or oxidant, and the combustion products are carbon dioxide and water for hydrocarbon fuels. Combustible mixture can be ignited then generated the flame, then produced combustion products. There are, however, other small yet critical intermediate products in the flame, and these intermediate products are what allow the existence of the perceived flame to be seen. This combustion phenomenon is related to free radicals during combustion and is called chemiluminescence. During the combustion process, the energy levels of various free radicals will generate chemiluminescence. The information contained in flame chemiluminescence is closely related to the flame temperature, mixture concentration, and heat release parameters (Yang et al. 2015). Based on the characteristics of flame chemiluminescence, flame dynamics can be studied in depth, the combustion characteristics can be understood and the understanding of combustion can be improved.

2.3.2 Electron Transition

Electron transition is when the electron on the outermost layer of a particle can absorb energy while transitioning from a lower level to a high-energy level, and it emits energy when transitioning from a high level to a lower one. In the process, energy is the absolute value between the two levels. Energy is absorbed and emitted in various forms. When the form has no relation to radiation, it is called non-radiative transition; the opposite is called radiative transition (Yang et al. 2015).

Radiative transition can be divided into three categories—stimulated absorption, spontaneous emission, and stimulated radiation—as first proposed by Albert Einstein (Masters, B.R., 2012). The radiation light shines into a substance, and the electron absorbs photon energy. The transition from a low level to a high level is called stimulated absorption.

The process of electrons transitioning from high to lower levels and emitting photons under the excitation of the external radiation light is called 'excited radiation' (Mitchell, A.C. and Zemansky, M.W., 2009). The incident light shining on photon can caused radiation excited, so photons generated from electron transition are relevant to the incident photon. Planck (1913) thought photon energy was isolated, so that the transition absorption or the emitted photon energy can be described as follows:

$$E_{photon} = h\nu = E_2 - E_1 \quad (2.1)$$

where h means Planck constant $6.626196\times10^{(-34)}$ J·s and ν is the frequency of the generated photon.

2.3.3 Hydrocarbon Flame Chemiluminescence

There are generally two types of flame colours: blue flames and yellow flames. The flame of a gas stove is a blue flame. This is the radiation emitted by the CH radicals and OH radicals excited by the high temperature in the flame. The characteristic wavelength of the CH radical is blue-green and the OH radical is blue-purple; blue flames are the result. Yellow flame is due to excessive fuel, insufficient oxidation, and the radiation of carbon particles produced by the cracking of hydrocarbon fuel (Huang, H.W. and Zhang, Y., 2011).

Excited molecules in the flame are formed by thermal excitation and chemical reactions. There are typically two steps to this. First, two species react to form excited molecules:

$$A + B \rightarrow R^* + other \quad (2.2)$$

where R^* is an excited radical. The spontaneous loss of excess energy then reaches their ground state through the release of a photon.

$$R^* \rightarrow R + h\nu \quad (2.3)$$

The wavelength of electromagnetic radiation depends on the molecule R and its specific

step. Each radical R is characterised by one or more emission lines, which can be divided into specific spectral bands. Combined with various free radicals, the chemiluminescence spectrum of a specific flame is generated (Adamovich, I.V. et al. 2015).

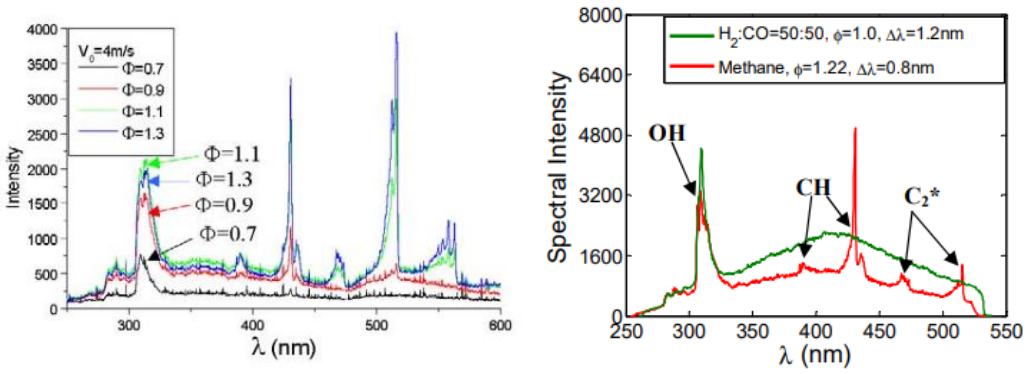

Figure 2-6. Flame spectra measured at different equivalence ratios (Hardalupas, Y. & Orain, M, 2004); typical flame spectra in syngas and methane fuels (Nori, V. and Seitzman, J., 2007).

Flame chemiluminescence radiation characteristics have been widely used as combustion diagnostic methods, as illustrated in Figure 2-6 (left). This shows the measured chemiluminescence emissions at different equivalence ratios. As demonstrated, OH^* radicals are excited between 300 to 320 nm, CH^* radicals are excited at around 430 nm and C_2^* radicals are excited at around 430 and 516 nm for all equivalence ratios. The work shown in Figure 2-6 (right) illustrates the peak of OH^* radicals excited at 309 nm, and the peak of CH^* radicals excited at 430 nm. Many researchers (Hardalupas, Y. & Orain, M, 2004 & Nori, V. and Seitzman, J., 2007) have used the radiation properties of excited molecules at specific wavelengths to characterise the flame and the combustion heat release rate, or have used flame

chemiluminescence to relate to the equivalence ratio (Yang, J. et al. 2015). The potential for using flame chemiluminescence as a flame characteristic is well established (Jiansheng, Yang. 2015).

2.4 Flame Propagation in Tubes

2.4.1 Background of Flame Propagation

When a hot object or an electric spark lights the combustible mixed gas, a thin layer of flame will form (Phillips, H., 1965 & De Goey, et al., 2011). When the combustion rate is small, the combustion products can freely expand in any direction. This means that flame propagation can completely rely on the heat transfer from the flame surface, and it will heat the unburned mixed combustible gas in the adjacent layer and increase its temperature to the burning point. The phenomenon of a flame propagating, layer by layer, to the unburned mixed combustible gas and gradually extending to the whole mixture of combustible gas is called flame propagation (Zeldowitsch et al. 1988).

Combustible gases normally refer to various gases that can be ignited in an oxygen-rich environment. Combustible gases have a wide range of applications in industrial areas and are important resources (Baukal Jr, C.E., 2000). Examples of combustible gases include hydrogen, methane and propane. All of these will be used in this thesis, to

investigate the hydrogen concentration effect of flame propagation in a tube at different fuel mixture conditions.

Hydrogen is an extremely flammable gas, under normal temperature and at room pressure (Xiao, H., Duan, Q. and Sun, J., 2018). At only 1/14 the density of air, hydrogen is the least dense combustible gas. Therefore, hydrogen was previously used as a gas to fill airships and children's balloons. This usage was later changed to helium gas, because hydrogen is extremely flammable. Methane is the simplest organic molecule and can be extracted from many resources, including natural gas, oil field gas and biogas (Noorollahi, Y., et al., 2015). Methane can be used as a fuel directly, due to its flammability, or hydrogen can be extracted from methane as a raw material (Olah, G.A., 2005). There are many advantages to the study of methane. These include its ease of storage, allowing it to provide energy for decades, as well as the fact that methane is a strong greenhouse gas which burning it can help reduce air pollution. Propane is one of the most common fuels used by the general population, and can be found in applications ranging from fuel for heaters to barbeque fuel tanks. All these combustible gases share common characteristics, such as being colourless, tasteless and difficult to dissolve in water.

In combustion science, flame can be classified into static flame and propagating flame. The explosion flame of mixed gas in pipelines comprises not only premixed flame, but

also propagating flame. The theoretical research about static flame is relatively mature. Yet research into flame propagation, which requires special testing and analysis methods, is insufficient. In the propagation process of flame acceleration, flame frequently becomes instable (Dorofeev 2011). Although research exists regarding the steady state of premixed flame instability, few studies have been carried out about the change of the flame structure and the instability mechanism in the process of flame propagation (Dorofeev 2011; Ciccarelli, et al. 2008; Xiao, et al. 2012). There is also no in-depth research into the nature of turbulence formation, the influence of combustible gas, or gas interface instability on flame acceleration in the flame propagation process (Ebieto, C.E. et al. 2015 & Yang, et al. 2015).

2.4.2 Characteristics of Flame Propagation in Tubes

Early combustion researchers began studying flame propagation in a tube more than a hundred years ago (Mallard E. F. & Le Chatelier, H. 1883). Yet its mechanics have yet to be fully explained, due to the multiple characteristics involved. The propagation of flame is mainly influenced by ignition energy, wall constraints, instability, and the effect of radiant heat (Dune et al. 1988). The propagation of premixed laminar flame in a closed pipeline is more complex, as it is influenced by the both effect of the shell and boundary layer, pressure wave effect and flame instability, as well as changes in the flow field (Xiao et al. 2013). In the initial stage of development, flame cannot maintain

its spherical expansion. When propagation occurs in the pipeline, it is difficult for the flame shape to retain smooth surface movement. It folds and deforms easily, and then it develops into turbulent flame or even deformed flame (out of normal curved flame). The flame propagation dynamics and flow field structure (including the flow and vortex induced by flame, and the overpressure dynamic) of laminar flame and turbulent flame are obviously different (Akkerman et al. 2016; Searby, G. & Rochwerger, D. 1991).

The effect of turbulence on flame propagation was discovered through experiments with a long tube. Flow increases with the size of the pipe diameter. As a result, the turbulent combustion rate is not within the characteristic parameters of the reaction mixture, but is instead closely related to the pipe size. The transfer of heat and mass in turbulent flame is associated with the distribution of the geometric size of the vortex. The laminar burning velocity is the characteristic parameter of the fuel mixture, and is not affected by pipe diameter (Lipatnikov 2012).

In most cases, the chemical reaction occurs in the location of the laminar flame, yet the overall flame is a turbulence combustion. The turbulence mainly works on the disturbed laminar flame and causes the flame front to wrinkle. Fristrom and Westenberg (1965) provided a comprehensive report on the structure of laminar flame. They stated that the chemical reaction kinetics, thermophysical properties and transport properties of the components within the flame are the key effects for the internal structure of the flame

and for the combustion rate of laminar flames. Since then—with the growth of computational power—the structure and combustion rate of laminar flames have been primarily studied through numerical methods, because all thermochemical and transport properties of the components are saved in the software database.

2.4.3 Flame Instabilities

The instability of premixed flame refers to the deformation and fold amplitude of the ideal flat flame, which results from tiny, injected disturbances (Matalon, M., 2007). In the propagation process of premixed flame, unstable propagation will frequently appear (Yang et al. 2015). Flame instability will trigger the mutation of the flame speed and pressure. Although the combustion process is complex, the basic theory of flame instability is simple. If the combustion process takes place in a free space, the sound wave will vanish through radiation and dissipation. However, if is in a confined space—such as in a pipeline—the sound wave may be reflected by the pipeline shell and then interact with the combustion process (Morgan, M.D., et al. 2004). At the root of flame instability is the fact that chemical reactions and flow are in unstable equilibrium states, and these equilibrium states will be broken even by tiny disturbances. They are also sensitive to flow field changes and combustion instabilities may occur as a consequence. Factors such as gas expansion in the flame flow field, diffusion-thermal effect, gravity and buoyancy may all cause instability (Fleifil et al. 1996).

A considerable number of factors can affect flame propagation and stability. Among these factors, the mutual interference effect between the pressure wave and combustion flame is the most common; it will induce turbulence combustion and growth (Xiao, et al. 2018). In industrial disasters such as the Hydro Agri explosion (Pande et al. 2000), the pressure wave acts on the flame and further quickens the burning speed of the flame. At the same time, the flame becomes unsteady and induces turbulence. As a result, the phenomenon of burning that turns into detonation may occur.

There are several different types of flame instability that may be affected during flame propagation in a tube, such as hydraulic instability, thermal diffusion instability and Rayleigh-Taylor instability (Matalon, M., 2007). Studying how these instabilities affect the flame is always a key area of research. Hydraulic instability was proposed by Georges Jean Marie Darrieus in 1938 and by Lev Davidovich Landau in 1944. Thus, hydraulic instability is also called Darrieus-Landau (DL) instability. Hydraulic instability is the result of the thermal expansion of a gas. In hydraulic instability, it is assumed that the flame front is infinitely thin and that the flame propagates at a constant speed to the unburned areas, which are not affected by hydraulic instability in this process. For a slightly curved flame surface, as Figure 2-7 shows, the flow lines of the flammable gas behind the convex portion of the flame surface converge with each other, and the flammability of the flammable gas behind the flame surface depression portion

is divergent. The perturbed flame surface is equivalent to a flat gyroplane, which makes the curvature of the curved portion of the flame surface larger and causes a pressure gradient. This makes the flame deformation more obvious (Matalon 2009). It is worth noting that this conclusion is based on the assumption that the flame surface is infinitely thin. The diffusion process of various substances in the flame usually inhibits or strengthens the effect of hydraulic instability.

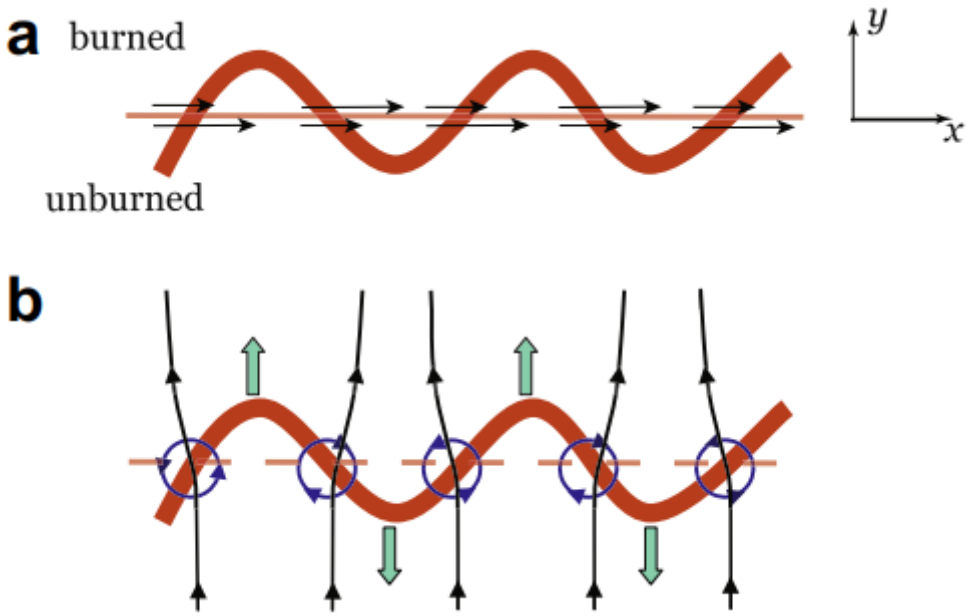

Figure 2-7 Schematic showing the physical origin of the DL instability (Matalon, 2009)

Thermal diffusion instability is caused by the difference between the molecular thermal conductivity of the gas mixture and the molecular diffusivity of the reactants with a small volume fraction (Elperin et al. 1997). It is mainly caused by the thermal diffusion and mass diffusion imbalance inside the flame front, which makes the flame front disturbed and wrinkled. It is usually indicated by the Lewis number:

$$Le = \frac{\alpha}{D} \tag{2.4}$$

where α is thermal diffusivity and D is mass diffusivity.

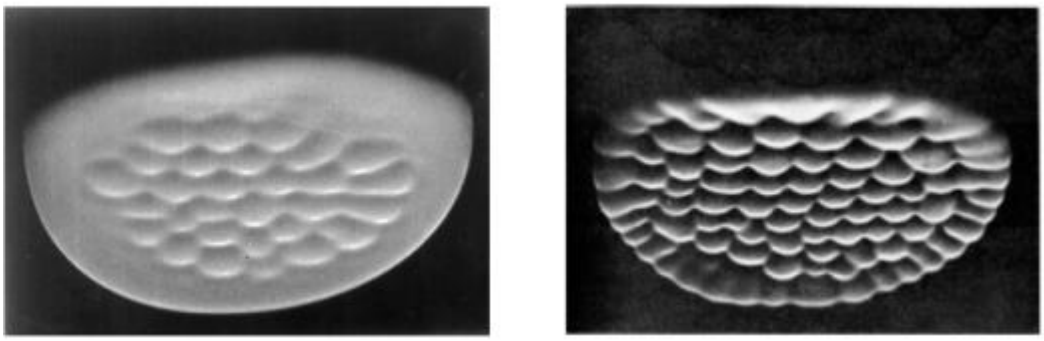

Figure 2-8. Cellular flame affected by thermal diffusivity (Matalon 2009)

When the Lewis number is smaller than one, the thermal diffusivity instability also makes the flame unstable and the flame front disturbed and wrinkled. When the Lewis number is equal to one, the thermal diffusivity and mass diffusivity will be balanced inside the flame, which means there will be no thermal diffusivity instability effect. With a Lewis number larger than one, thermal diffusivity instability makes the flame front wrinkled and more stable (Sivashinsky 1979). Figure 2-8 shows how the cellular flame is affected by thermal diffusivity.

The flame propagating in a confined space will generate a pressure or sound wave, which can be reflected by the wall or other obstacles; the reflected wave can interact with the flame front, disturbing the resulting flame front. To summarise, the interaction between the flame and the pressure wave creates a vortex, and this causes changes to the flame shape and increases the flame area. In confined flame propagation, Rayleigh-Taylor instability has a large impact on the flame (Keenan et al. 2014). Rayleigh-Taylor

instability is usually produced when a low-density fluid is accelerated to a high-density fluid. As for the simulation of large pipelines, research findings show that pressure waves exist in front of the flame; the flame pursues the pressure wave, and it then stacks to enhance the impact effect. Experiments indicate that, for small pipelines, there is no significant spatial difference (Lieuwen 2003).

2.4.4 Deflagration and Detonation

The slow combustion of flame (i.e., normal flame propagation) is propagation caused by the flame front transferring heat to the combustible mixture in the form of heat conduction and convection. The speed is low (from 1 to 3 m/s) in slow combustion flame propagation (Bradley, D., et al. 2007), which is much slower than the speed of sound. The flame propagation process is steady. General engineering combustion is classified as slow combustion.

Deflagration is a type of flame propagation that is caused by adiabatic compression. Deflagration is also a chemical reaction, which arises owing to the increased temperature of the unburned mixed gas resulting from the compression effect of the shock wave (Zhang, Q., et al. 2020). As the combustion waves approach the unburned gas and the propagation speed exceeds 1000 m/s, the velocity is greater than the speed of sound. Explosions and the flame propagation of compression ignition engines are

also regarded as deflagration.

The propagation and acceleration of the premixed flame in a pipeline may lead to the transition from laminar combustion to turbulent combustion. It may even lead to the transition from deflagration to detonation (DDT) (Liberman et al. 2012). Deflagrations can be divided into two types: laminar combustion and turbulent combustion. Deflagration waves propagate at subsonic speed relative to the front unfired gas. They are mainly controlled by molecular, turbulent transportation and heat conduction. Detonation waves, in contrast, propagate towards the unfired gas at a supersonic speed. Detonation waves consist of leading shock waves and chemical reaction zones, which interact with each other and lead to shock waves compressing and heating the front unfired gas (Shepherd, J.E. and Lee, J.H., 1992). Afterwards, the high-temperature unfired gas burns and releases energy into the reaction zones, through which detonation waves achieve self-sustainability and propagation (Bai et.al, 2011). Figure 2-9 shows how flame acceleration and DDT occur, illustrating that all flame propagation can potentially become DDT under certain conditions. The details of DDT will not be provided in this thesis because of the experiment environment limit.

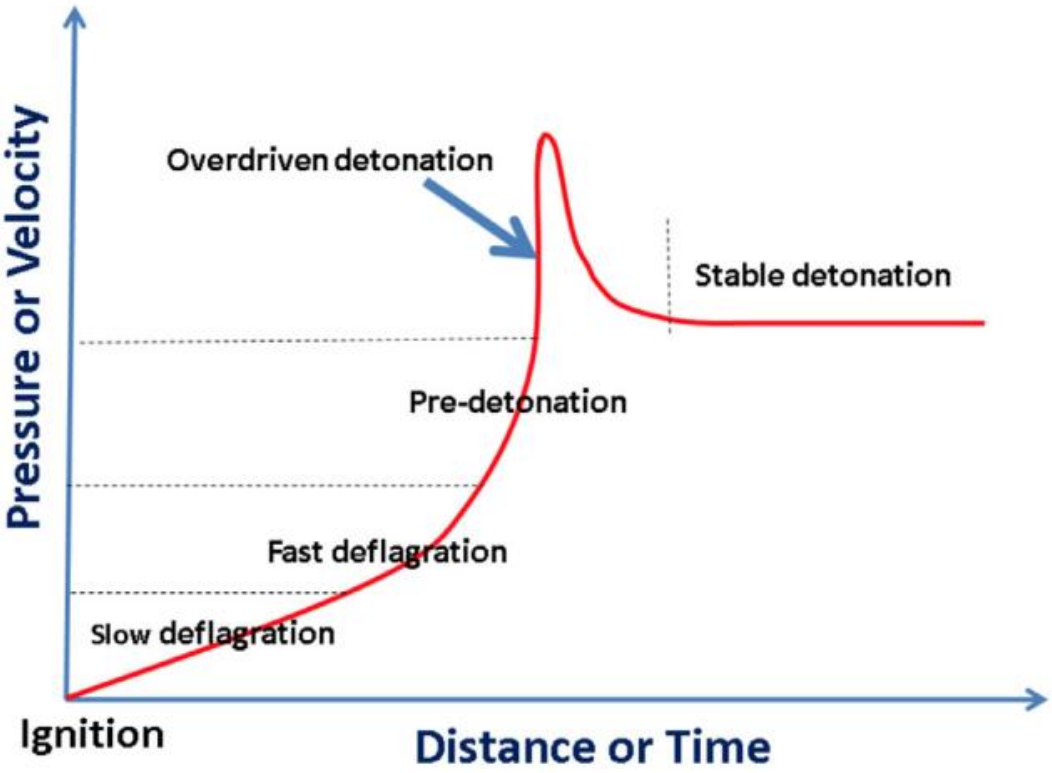

Figure 2-9. Schematic showing the phases in the evolution of a combustion system from a deflagration to a detonation.

It is generally believed that the mixed combustible gas in pipelines becomes laminar flame in the initial period of ignition. Assuming that the pipe is long enough, with repeated obstacle components, it is then generally accepted that the process develops into deflagration or detonation after the stages of initial laminar, local turbulence, turbulence increase, mutual stimulation between turbulence and flame and sharp acceleration (Hirschfelder et al. 1949). To accurately determine the variation trend of flow field parameters in the process of flame propagation, there must be an in-depth study on the mechanism of flame propagation in pipelines. Thus far, most determination of flame propagation parameters is still based on experiments and experience. Yet this

determination requires a more rational and more scientific theory, to explain such complex practical problems. Therefore, further study on the mechanism of pipeline flame propagation and on the relative spatial relationship between flame and pressure waves is vital (Markstein 1957). To summarise, the propagation of premixed flame in confined spaces is an important technical issue in the fields of combustible gas safety, internal combustion engine applications and detonation wave theory. To understand the optimisation and improvement of a combustor's structure—as well as the performance evaluation of alternative fuel—fundamental flame propagation data and detailed chemical reaction mechanisms are also needed, to build a combustion model in the field of combustion.

Previous research has primarily focused on detonation, and on the transition of deflagration to detonation. Research is inadequate regarding the behaviour and the mutation mechanism of flame propagation in pipelines at the early stage and transition stage. Yet this early stage has an important and practical reference value, in terms of developing the law of explosion processes—especially regarding the formulation of timely and effective measures to suppress flame explosion.

2.4.5 Tulip Flame

The propagation of a premixed flame in a pipeline is a complicated issue. The surface

of the flame becomes unsmoothed due to the influence of body force, hydraulic instability, thermal diffusion instability and the boundary layer effect (Ciccarelli & Dorofeev 2008). In the late nineteenth century, scientists Mallard and Le Chatelier were among the first to research premixed combustible gas explosions in pipelines (Mallard & Chatelier 1883). They found that the flame surface propagating towards the pipeline opening would flip several times in the direction of the pipeline axis, in semi-closed pipelines.

In 1928, Ellis O.d.C captured the first image of a wrinkled flame. This image indicated that—in the late stage of combustion—the finger-shaped flame bulging towards the unfired gas would suddenly reverse, under the premise that the length-width ratio of the pipeline was large enough (i.e., larger than 2). In 1958, G.D Salamandra named this the 'tulip flame'. A considerable number of experiments and research have been conducted on the simulation of basic flame kinetics, aiming to explain the change and formation mechanism of the tulip flame. Nevertheless, a unified consensus has yet to be reached, regarding how the chemical reaction and pressure wave generated by flame itself affect the formation of a tulip flame.

Dunn-Rankin et al. (1988) explored the effects of pipe length, equivalence ratio and different types of ignition methods, while trying to explain the relationship between pressure wave and flame shape changes. The radial gradient of the compressed unfired

gas axial velocity is the main reason for the cause of the tulip flame phenomenon, and the distortion of the flame will grow and increase in response to hydraulic instability. Through numerical simulations, Gonzalez et al. (1992) found that the transverse velocity gradient of the flat flame surface arising from the wedge-shaped extrusion flow, the deceleration of the flame in axis and its hydraulic instability are significant in terms of the formation of the tulip flame. In the research conducted by Dunn-Rankin and Gonzalez et al. (1988, 1992), the influence of the pressure wave effect (i.e., the sound wave effect) and vortex motion in the fired gas are denied or ignored. In Markste's (1957) interaction experiment between laminar flames and shock waves, he finds that the sunk (converse) shape is similar to the tulip flame. He explains this via the modified Taylor instability theory, and pinpoints the pressure wave mechanism for the tulip flame formation. However, an experimental environment without shock waves verified the contribution of Taylor instability to flame development. This means that the tulip flame is not driven by pressure waves, but instead results from the deceleration of the flame front surface.

Generally speaking, the propagation mechanism of the premixed flame in the pipeline is the result of multiple parameter interactions, including initial temperature, pressure, the equivalence ratio, the pipe size and the ignition mode. There is no single mechanism that can properly explain the characteristics and behaviours of premixed flame propagation in the pipeline. Therefore, Dunn-Rankin (1998) proposes that the tulip

flame may be the product of joint actions among different mechanisms. This means that the tulip flame is actually a combination of a series of flame propagation processes.

In addition to traditional research about the tulip flame, recent research has discovered new flame phenomena (Xiao et al. 2013). In the 1990s, Clanet and Searby (1996) divided the propagation process of premixed flame in a half-opened end pipeline into four characteristic stages: 1) semi-spherical (spherical) expansion that is not affected by the wall, 2) finger-shaped flame with exponential growth, 3) flame contacting the shell surface and 4) the classic tulip deformation found in a closed pipe. Bychkov et al. (2007) propose that the tulip flame is not about the Reynolds number, at the early stage of flame acceleration and formation of the tulip shape. Gonzalez (1996) found the interaction between the flame front and the acoustic wave in a closed pipeline using numerical simulation. This simulation shows that changes to the flame shape and the periodic oscillations in the later stages are actually caused by the interaction of the flame front and the sound waves. The essential cause of these phenomena is Rayleigh-Taylor instability. This conclusion is similar to Markstein's (2014) flame shock experiment exploring the interaction between a laminar premixed flame and a shock wave, using the schlieren technique. Xiao et al. (2012) discovered a significant deformation of the tulip flame in a premixed hydrogen-air flame; they defined it as the fifth stage of Clanet's and Searby's theory (1996). After the initial tulip flame formation, the classic tulip flame front will continue to grow, finally forming the secondary tulip

structure.

In terms of modelling, Clanet and Searby (1996) have built an experimental model of premixed flame propagation at characteristic stages, to estimate time and flame front positions. Bychkov et al. (2007) further analyse the basics of this model. They have proposed an analysis theory of the flame acceleration process and early flame propagation in half-opened cylindrical pipeline conditions. This theory demonstrates that it is suitable for early flame propagation of a limited range of equivalence ratio conditions for premixed propane-air. Xiao et al. (2013) suggest that the pressure wave, which is induced by the flame, touches the shell surface and plays a determining role in the process of deformation in the tulip flame. They also believe that the initial conditions and boundary conditions have a significant impact on the premixed flame propagation—including initial temperature, initial pressure, wall effect, heat loss, etc.

In recent years, most studies about this topic have focused on the formation of tulip flames and deformed tulip flames. Although many possible formation mechanisms of tulip flames have been proposed, no unified consensus has been drawn. Many studies have been carried out regarding the effects of equivalence ratios, boundary conditions, the geometry of tubes and flame instability on premixed flame behaviour and flame dynamics. These experiments have led to the analysis of subjects including flame fronts, pressure waves, flame induced flows and vortexes. However, most experiments or

simulations have used a single combustible gas like pure methane, pure propane or pure hydrogen. There are relatively few studies about multiple combustible gases. At present, there is still a lack of adequate experimental research on the premixed flame propagation of hydrocarbons in the tulip flame. It is essential to carry out these experiments and conduct research—both to fully understand the phenomena of tulip deformation and the effect of pressure waves, and to understand the mechanism of tulip flame formation.

2.4.6 Flame Burning Velocity

Flame propagation velocity is the speed of movement of the flame front relative to the observer—i.e., the speed relative to the ground or stationary coordinate system (YAKHOT, V., 1988). The speed of flame propagation is related to the speed of airflow, the constraints of the pipeline, the opening and closing rate of the structure ends, etc. It is not the characteristic quantity of the flame. The average value of the flame propagation speed in different mortar systems is generally regarded as the typical flame propagation parameter. The flame burning velocity is different from the flame propagation speed. The flame burning velocity is related to the burning rate of fuel consumption (Ebieto, C.E. 2017). Its magnitude characterises the fuel combustion release rate, which is one of the flame characteristics. Although the flame burning rate is related to the initial temperature and pressure, the common gas mixtures with air at

normal pressure and room temperature were systematically measured and can be found in the book. Laminar flame burning velocity is the most basic parameter and is also the basic attribute of combustible gases. Therefore, laminar flame burning velocity is the basic element for research on complex combustion systems. In turbulent combustion, for example, it is believed that all chemical reactions occur in the internal part of a small laminar flame, but the flow will disturb the laminar flame and make it fold. The laminar flame burning velocity mainly depends on the thermodynamic properties of the mixture, its transport properties, and its chemical kinetics (Rhodes et al. 1985).

In recent years, researchers have carried out numerous experiments on the laminar burning velocities of different combustible gases under different initial conditions. However, due to inconsistent experimental conditions and theoretical methods—especially in the early years of this research when experimental devices and theoretical analyses were insufficient—it is predicted that there are some differences and even significant mistakes in the measurement results.

Flame burning velocity is an important parameter for combustion characteristics. From a practical perspective, it influences the combustion and efficiency of fuel in the burner flame. It can also be used to verify the chemical reaction mechanisms of various fuels. Flame burning velocity is also an important input parameter for the simulation of turbulent premixed flame propagation.

2.5 Summary of Review

Flame propagation is constrained and influenced by several factors. These include the structure and size of the confined space, the property of the combustible gas, the instability of the flame, the pipeline shell, the boundary layer effect and the pressure wave. The flame will propagate to the unburned gas once it is ignited; this will form a combustion wave. Premixed flame propagation in a tube will typically follow these processes from ignition to laminar flame, disturbed flame, transition from laminar flame to turbulent flame (Yang et.al, 2015) and even deflagration to detonation, if the confined space is long enough. Current research on the behaviour and mutation mechanism of flame development in the early stage is inadequate. However, in terms of formulating effective measures to suppress flame explosion, studying flame propagation in the early stages has an important and practical reference value.

The research undertaken in this thesis intends to understand the essence and mechanism of flame and the development and acceleration of a flame in a confined space, to analyse the physical and chemical process of the flame's internal structure and to establish a potential flame prediction method. To achieve this, it is necessary to explore the pressure wave of premixed flame and its chemical reaction mechanism in a confined space, utilising a comprehensive experiment with theoretical methods. This research will serve as a scientific reference to contribute to the prevention of combustible gas

explosion accidents and help control the spread of such accidents through early control and chemical inhibition. The hydrogen effects of hydrocarbon fuels will also be explored.

Although many institutions have carried out combustion research, many fails to find flame images that are restricted by the experiment conditions. It is therefore difficult to distinguish the characteristics and time points of different stages of flame development. It is also difficult to determine whether or not the violent deformation and cell lattice structures of flame are affected by instabilities (Fleifil et al. 1996). Hence, utilise the high-speed imaging system can help to connected the relationship between the morphologic change of flame, flame propagation speed and pressure change (or pulse).

3 CHAPTER THREE: Methodology

3.1 Introduction of Flame Diagnostic Measurement

Combustion diagnostics is actually combustion measurement. Different methods are used to obtain information—such as species concentration, temperature and flow field—in the combustion process, which provides an experimental basis for understanding the complex chemical reactions and flow processes in combustion. The parameters measured include temperature, velocity, pressure during combustion and the concentrations of hundreds of species (Einecke, S., et al, 2000). Over the past several decades, researchers have advanced the field of combustion diagnostics and invented new methods for combustion diagnosis. The development of these methods has been utilised to solve a number of different combustion problems, promoting a better understanding of the combustion process.

Current diagnostic methods are divided into two categories: contact measurement and non-contact measurement. Contact measurement utilises tools such as thermocouples (Marr, M.A., et al, 2010) and flue gas analysers (Lasek, J.A., et al, 2017) to take samples during combustion. This method normally involves probes or thermocouples during the measurement process and it cannot avoid interfering with the combustion field. Non-contact measurements include optical techniques to measure components in the field, such as the schlieren method and the colour-based flame chemiluminescence method.

Other types of non-contact measurements use tracer particles, such as particle image velocimetry (PIV), laser doppler velocimetry (LDV) and laser-induced fluorescence (LIF), etc. This thesis focuses on non-contact combustion diagnostics: schlieren method and the colour-based flame chemiluminescence method, since contact has disadvantages that can disturb the flame.

3.2 Schlieren Image System

There are three key optical methods to observe the flow field: shadowgraph, schlieren photography and interferometry. From these, the schlieren method can most intimately observe fluid behaviour, and this technique is a classic method for flow field measurement and display. The schlieren method was first proposed by Robert Hooke in the seventeenth century (Rienitz 1975). August Toepler then improved it in 1884. It is widely used in research fields where the flow field density changes, such as in heat transfer, combustion, turbulence, and shock waves. Schlieren measurement is based on the deflection of light as it passes through a stable, non-uniform refractive index field. The degree of deflection of the refractive index is proportional to the density change, so the shading boundary of the spherical flame experiment is located at the maximum value of the gas density gradient, i.e., the flame front. In other words, the principle of schlieren imaging is the light and dark pattern caused by the refraction of the propagation of light in different refractive index media, which results in the light no

longer being of uniform intensity on the image plane. For a completely homogeneous environment, when the knife edge blocks half of the reflected light, the spot captured in the camera should be an inverted image of a half-point light source. When the whole schlieren system is placed indoors, slight changes in brightness and darkness can be observed since the air is not completely stationary. If an object that can disturb the airflow—such as a burning candle—is placed in front of a mirror, its effect can be observed on the surrounding flow field.

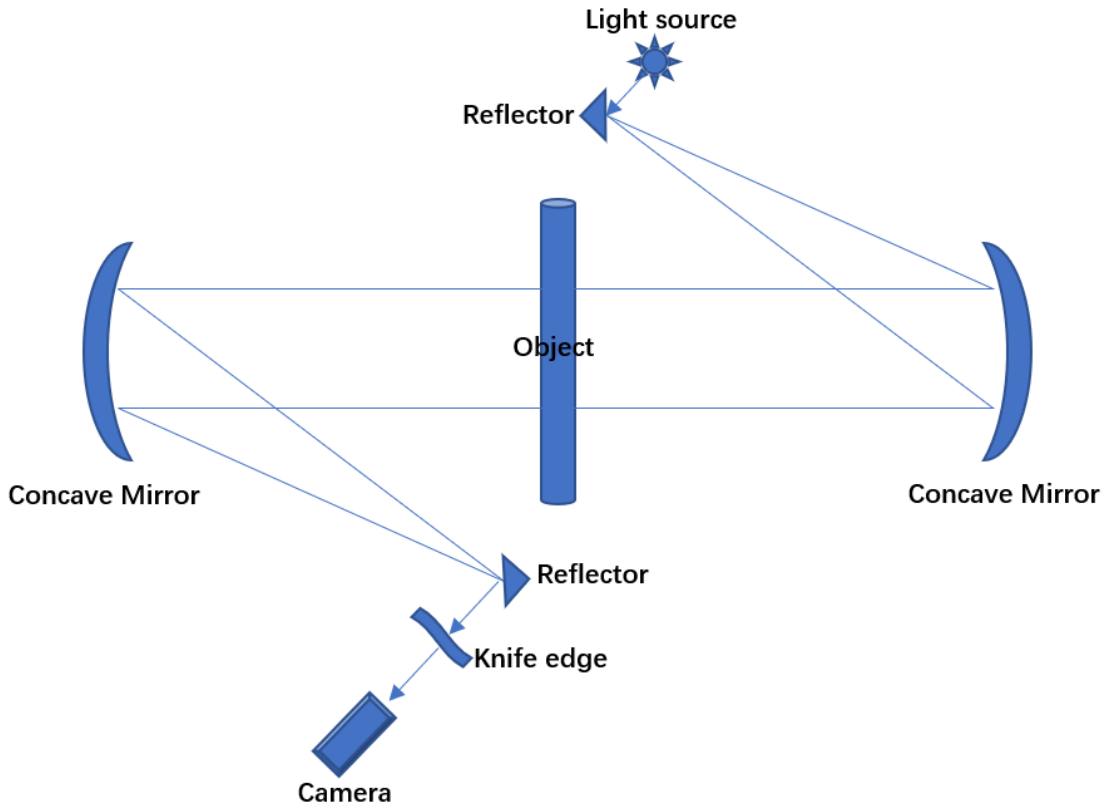

Figure 3-1 Z-type schlieren system.

Figure 3-1 illustrates a typical Z-type schlieren system consisting of two concave mirrors, two reflectors, one light source, one knife edge and one camera system connected to the computer. The light from the light source passes through a small hole

to form a point light source. The reflector then reflects the light to the concave mirror on the right, to create a parallel light between the two concave mirrors. The observed object should be placed in the middle of these mirrors and the light should cover it up. The light passes through the left concave mirror and is refracted into the camera through a refractor. The knife edge should be placed between camera and reflector. The sensitivity of the schlieren system is directly related to the focal length of the schlieren concave mirror and the size of the knife edge cutting the light source. The greater the focal length of the schlieren concave mirror and the more the light source is blocked by the knife edge, the higher the sensitivity of the schlieren system. At the same time, the light intensity is reduced as the sensitivity increases, which means the intensity of the view into the camera will be darker.

3.3 Calibration of Image colour-based flame chemiluminescence measurement system

3.3.1 Introduction

In 1666, British scientist Isaac Newton revealed the colorimetric properties of light and the secrets of colour (Mollon, J.D., 2003). His experiment demonstrated that sunlight is a mixture of various colours, and colour depends on the wavelength of light. The main source of natural light is the sun, and the primary sources of artificial light are

incandescent lamps, developed by Thomas Edison in 1879. An incandescent lamp is an electric light source that heats the filament to an incandescent state and uses thermal radiation to emit visible light. The visible spectrum is the part of the electromagnetic spectrum that can be seen by the naked eye. It falls in the range of 390 to 780 nm, as humans have different degrees of sensitivity to the colours.

3.3.2 The Relationship between Single High-Speed Colour Camera and Flame Chemiluminescence.

The camera records the moment the shutter is pressed, in a way that is similar to the functioning of the human eye. The light reflected from the surface of an object passes through the eye, and the light is then received and converted by the brain into neural signals. An image is then formed in the brain. The digital vision system is analogous to the human vision system, but it replaces human eyes and brains with cameras and computers (Yang, 2015). Compared to human vision, the advantages of the digital vision system include that it records light information using absolute measurement, that the recorded images can be processed and analysed by computers, and, most importantly, that the data can be stored for future retrieval and examination.

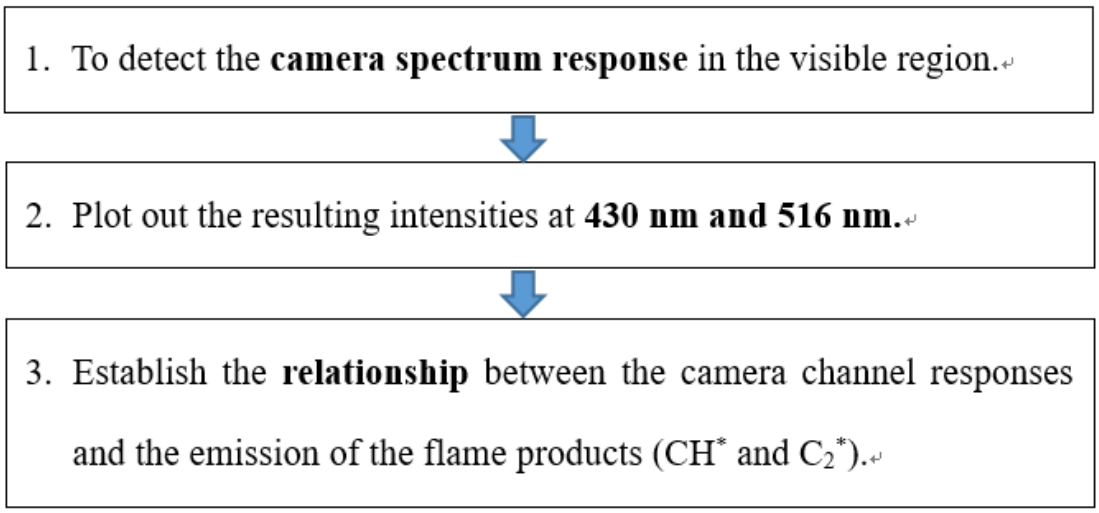

Figure 3-2 Flow chart of Image colour-based flame chemiluminescence measurement methodology

Image colour-based flame chemiluminescence measurement is based on relationships among the flame chemiluminescence, the camera sensor spectral sensitivity and the image colour model. This method was originally developed by Huang (2011), who found that two flame emissions (CH^* and C_2^*) have a strong correlation with the RGB model; this can be detected by a single-colour camera. Yang (2016) improved the calibration method which makes the system's accuracy improved. As noted in Chapter Two, there are colour filters on the camera sensor so the original information can be picked up during post-processing. Figure 3-2 shows that this information is obtained from the original image in three steps. First, the camera spectrum response is detected in the visible region, to plot out the resulting intensities at 430nm and 516nm. The relationship between the camera channel responses and the emission of the flame products (CH^* and C_2^*) is then established. RGB images are formed via the integration of the spectral illumination, the spectral reflectivity of the scene and the spectral

response of the camera. Unfortunately, the camera spectrum response is kept confidential by manufacturers. Without this information, the calculation of chemiluminescence and the chemiluminescence measurement proposed here cannot be implemented for combustion research. Therefore, an investigation of the spectral sensitivity in single high-speed colour cameras must be carried out.

3.3.3 Colour Camera Sensor Spectrum Sensitivity Setup

The first step of image colour-based flame chemiluminescence measurement is to calibrate the camera spectrum response, because each camera sensor has a similar function but a slightly different quality.

Figure 3-3. MI-150 (left); monochromator (middle); high-speed colour camera (right).

Figure 3-3 shows the three main devices used to calibrate the camera spectrum response: a light source, a monochromator, and the camera to be calibrated. The light source used for the current research is an MI-150 illuminator produced by Dolan Jenner Industries, which utilizes a 150W quartz halogen lamp. A halogen lamp is an incandescent lamp

that can provide a continuous spectrum. A monochromator is used to adjust the incoming light to the required wavelength. It is an optical component that allows the multicolour light emitted by the light source to output monochromatic light through the monochromator. The typical monochromator has an entrance slot with a fixed geometric position and a dispersion element—i.e., a diffraction grating—that can be rotated manually. The rotation angle of the grating is adjustable, and the wavelength of the output light is determined accordingly. The minimum adjustable scale of the monochromator used in this research is 1 nm.

The Photron FASTCAM SA-4 is a high-speed colour camera that uses a CMOS sensor with a constant 10,000 ISO for monochrome and 4,000 ISO for colour. The SA-4 camera can provide a square image of 1024 * 1024 pixels (which resolution is horizontal 1024 pixels times vertical 1024 pixels equals to 1048576 pixels) for a maximum of 3,600 fps. Or reduce the image resolution to 128 * 16 pixels (which resolution is horizontal 128 pixels times vertical 16 pixels equals to 2048 pixels) to allows fps reach up to 500,000.

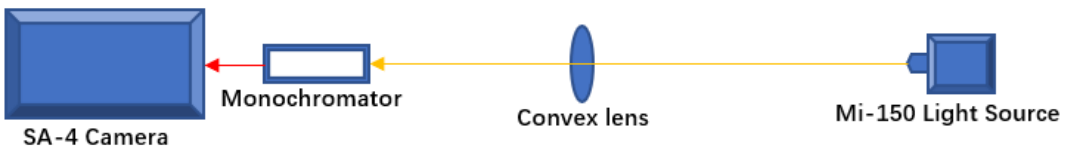

Figure 3-4. Schematic diagram of calibration of camera spectrum response.

Figure 3-4 shows a schematic diagram of the calibration work. All the devices are

placed on a table and the experimental devices are covered from the camera to the light source by heatproof and lightproof material to avoid unexpected light disturbance; the room lights are also switched off. A convex lens is placed between the light source and the monochromator, to ensure that light is forced into the monochromator. The wavelength range of the monochromator is adjusted from 350 nm to 750 nm with 5 nm intervals. All devices are fixed on the table, after adjusting the settings to ensure each picture is taken under the same conditions. Through this study of how the camera responds at the two selected wavelengths, the camera spectrum response can be determined. The emission of the light source covers the region of the complete visible spectrum and the use of the monochromator aims to separate the light to a required wavelength. This single wavelength is then detected by the high-speed camera. The captured signal will then be processed by a specially written code in MATLAB to provide the camera spectrum sensitivity across the range of visible spectrum wavelengths.

3.3.4 Spectrum Sensitivity of the Camera sensor

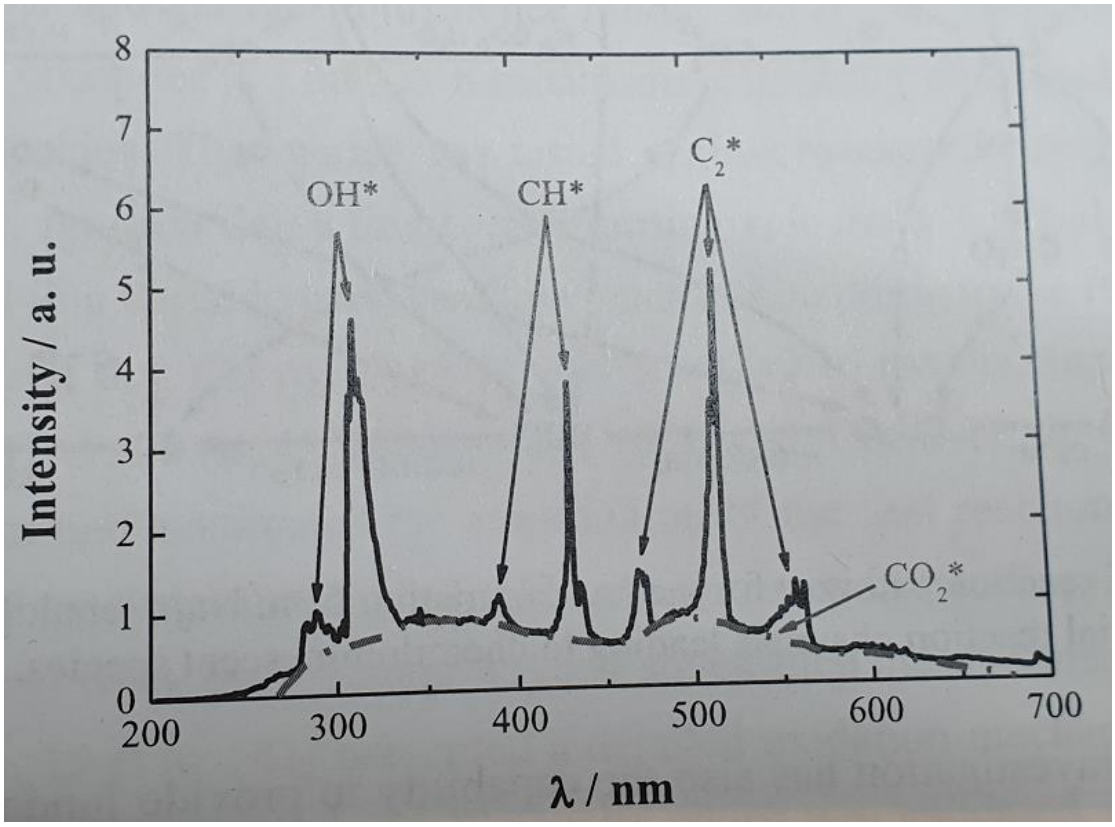

Figure 3-5 Typical flame emission spectrum of a premixed hydrocarbon flame (Bozkurt 2013).

Figure 3-5 shows the typical flame emission spectrum of a premixed hydrocarbon flame, under fuel rich conditions. It shows that four different chemiluminescence species (OH^*, CH^*, C_2^*, CO_2^*) have different excited ranges. The emissions of OH^*, CH^* and C_2^* have more than one peak value. The CH^* and C_2^* chemiluminescence measurement method proposed here is based on the assumption that all hydrocarbon premixed flame chemiluminescence only emits CH^* at 430 nm and C_2^* at 516 nm.

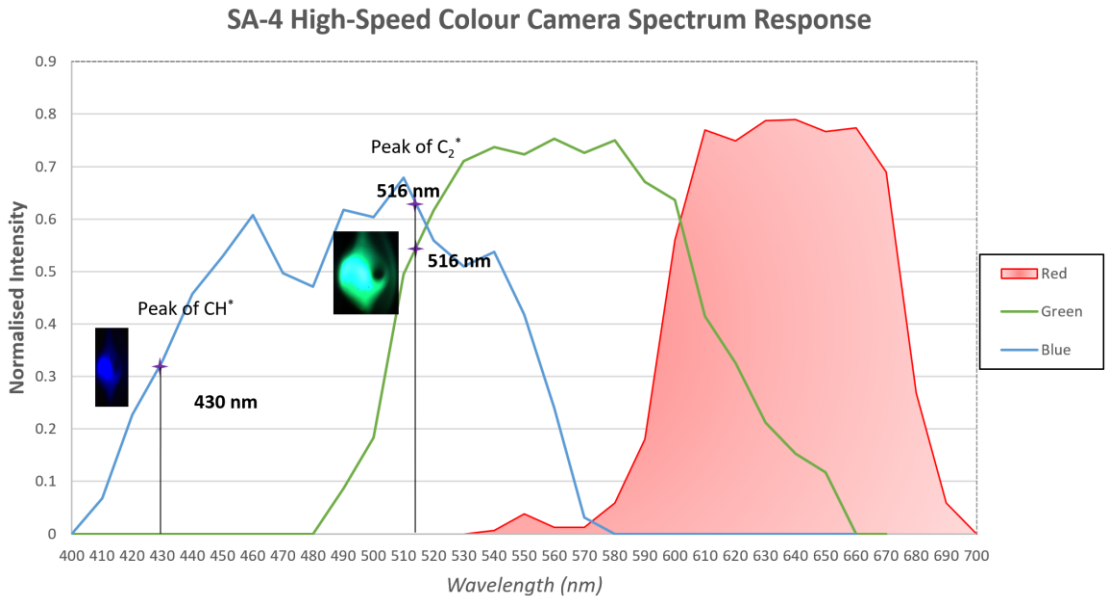

Figure 3-6. SA-4 High-speed colour camera spectrum response.

The spectrum response of different cameras is not identical in the R, G and B channels. The ratio of camera-specific parameter sensitivity is highly correlated to spectrum response. Therefore, this ratio must be known prior to the calculation of the CH^* and C_2^* chemiluminescence concentrations. Figure 3-6 shows the normalised spectral sensitivity ratios of R, G and B channels based on the calibration experiment. The x-axis is the wavelength within the visible spectrum and the y-axis is normalised intensity. Although the visible spectrum range is 350 nm to 750 nm, the core sensor of the SA-4 camera is only sensitive from 410 nm to 710 nm for any of the R, G or B channels. At 430 nm, there is only blue channel sensitivity, so the image colour is completely blue. At 516 nm, both B and G channels are sensitive; hence, the colour of the image is bluish green. The red channel is not sensitive at either 430 nm or 516 nm, so the R channel will not affect any results later during post-processing.

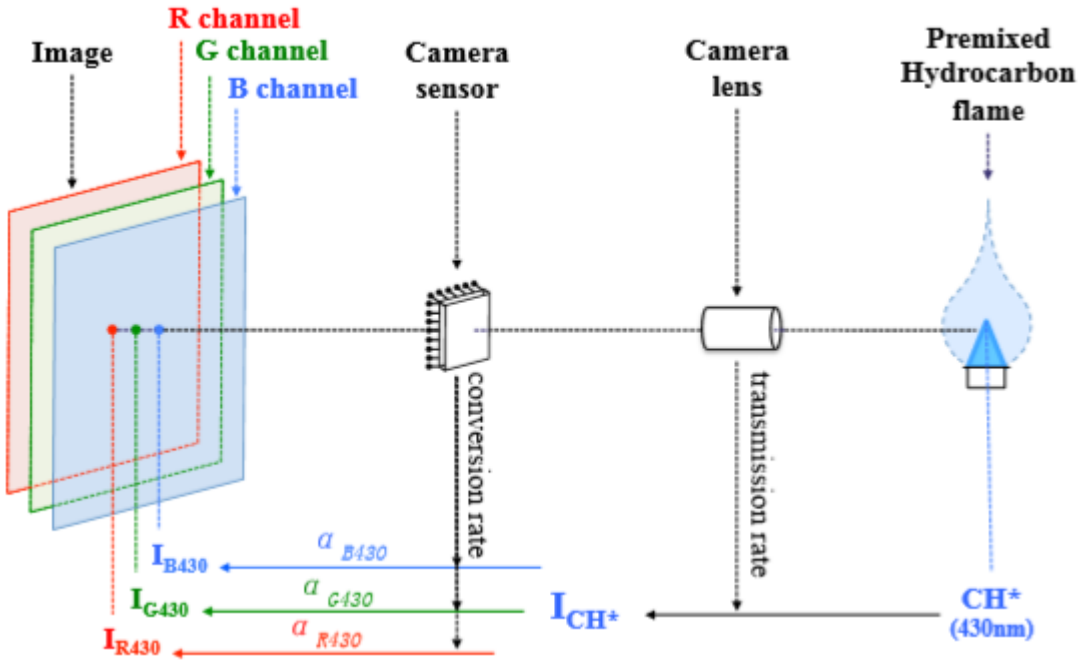

Figure 3-7. The relationship between image colour and radiation (Yang, 2016).

Once the calibration work is complete, a camera lens is installed. Figure 3-7 shows the relationship between image colour and radiation. Lens manufacturers try to minimise the light loss caused by refraction and dispersion, but it is impossible to completely eliminate light loss. Similarly, the camera sensor cannot fully receive the converted signal by passing through the lens. The free radical CH^* emissions are generated by the flame passing through the camera lens and enter into the camera sensor with a certain transmission rate and conversion rate. Hence, the relationship between each filter layer intensity and free radical emission can be represented as:

$$Intensity_{CH^*} = \frac{Intensity_{R_{430}}}{\alpha_{R_{430}}} = \frac{Intensity_{G_{430}}}{\alpha_{G_{430}}} = \frac{Intensity_{B_{430}}}{\alpha_{B_{430}}} \quad (3.1)$$

$$Intensity_{C_2^*} = \frac{Intensity_{R_{516}}}{\alpha_{R_{516}}} = \frac{Intensity_{G_{516}}}{\alpha_{G_{516}}} = \frac{Intensity_{B_{516}}}{\alpha_{B_{516}}} \quad (3.2)$$

where α conversion rate which have no unit is shown in Figure 3-7.

Based on the assumption that all hydrocarbon premixed flame chemiluminescence only emits CH^* at 430 nm and C_2^* at 516 nm, so image colour-based flame chemiluminescence measurement only 430 nm and 516 nm will be considered; hence, the intensity of the three channels can be defined as:

$$Intensity_R = Intensity_{R_{430}} + Intensity_{R_{516}} \tag{3.3}$$

$$Intensity_G = Intensity_{G_{430}} + Intensity_{G_{516}} \tag{3.4}$$

$$Intensity_B = Intensity_{B_{430}} + Intensity_{B_{516}} \tag{3.5}$$

Combining the emission intensities equations and channel intensities equations, the intensity of the channel equations can be calculated and simplified as follows:

$$Intensity_G = \alpha_{G_{516}} Intensity_{C_2{}^*} \tag{3.6}$$

$$Intensity_B = \alpha_{B_{430}} Intensity_{CH^*} + \alpha_{B_{516}} Intensity_{C_2{}^*} \tag{3.7}$$

Table 3-1 shows that the normalised spectral sensitivity ratio α is at 430 nm and 516 nm respectively. Which calculated by the result of SA-4 high-speed colour camera spectrum response and it shown in figure 3-6. The selected points of 430 nm and 516 nm were marked as star in the figure.

Table 3-1. Normalised spectral sensitivity ratio α.

Normalised spectral sensitivity ratio α		
$\alpha_{B_{430}}$	$\alpha_{B_{516}}$	$\alpha_{G_{516}}$
0.33	0.62	0.56

The CH^* and C_2^* chemiluminescence expression of the SA-4 camera sensor can be calculated as follows:

$$Intensity_G = 0.56 Intensity_{C_2^*} \quad (3.8)$$

$$Intensity_B = 0.33 Intensity_{CH^*} + 0.62 Intensity_{C_2^*} \quad (3.9)$$

Rearranging the above equations is given as:

$$Intensity_{C_2^*} = 1.79 Intensity_G \quad (3.10)$$

$$Intensity_{CH^*} = 3.03 Intensity_B - 3.3 Intensity_G \quad (3.11)$$

3.4 Image Post-Processing

3.4.1 Image Noise Reduction

Digital images are often affected by the interference of imaging equipment and external environmental noise during digitisation and transmission, as discussed in the previous chapter. The process of reducing noise in digital images is called image denoising. Although the Tag Image File Format (TIFF) used to store images does not actively generate noise, electronic noise is generated when the object captured by camera sensor which is the light signal transit to the electric signal, electronic noise enhanced as the ISO setting increase. SA-4 camera setting constant 10,000 ISO for monochrome and 4,000 ISO for colour will leads to generated electronic noise. The quality of the subsequent image processing is directly related to the quality of the image noise reduction. In order to obtain high-quality digital images, it is possible to remove the useless information in the signal while maintaining the integrity of the original

information as much as possible. Therefore, it is necessary to perform noise reduction processing on the picture before directly extracting the required information from the picture.

3.4.2 Image Enhancement

Image enhancement is a method to enhance useful information in an image. The purpose is to improve the visual effect of the image, purposefully emphasise the overall or local characteristics of the image and clarify an unclear image. While all images were denoised, the image enhancement used in this thesis is only to visualise the flame and its structure. The flame speed is fast in most flame-propagation-in-a-tube case studies and the highest possible frame per second rate is applied, to ensure that it can capture the details of the flame movement. However, in order to capture the clear movement of the flame, the required shutter speed is no longer than 1/fps. This leads to a very short exposure time and means the image is not visible without enhancement.

3.4.3 Fast Fourier Transform (FFT)

Any periodic function $f(t)$ can be represented by an infinite series consisting of a sine function and a cosine function. The essence of the Fourier series is to decompose a periodic signal into an infinite number of discrete sine (cosine) waves and transform it

into a discrete signal in the frequency domain. For example, a series of flames that are continuous in the time domain can then be converted into a frequency domain signal, using a fast Fourier transform (FFT). In this thesis, a fast Fourier transform will be used to analyse the frequency of the flame using a function code built inside the MATLAB database.

3.5 Conclusion

To summarise the methodology, two different non-contact optical technique measurements used in this thesis: schlieren method and the colour-based flame chemiluminescence method. Image colour-based flame chemiluminescence measurement is based on the assumption that all hydrocarbon premixed flame chemiluminescence only emits CH^* at 430 nm and C_2^* at 516 nm. The camera sensor's spectral sensitivity was calibrated. Image post-processing were applied to all the task images. MATLAB software will mainly be used for data analysis in this thesis. Table 3-2 shows the list and comparison of the test cases for Chapter four to seven. The tube size was used same 20 mm diameter with 1200 mm long for both round and square tube.

Table 3-2 Comparisons of test cases.

	Chapter FOUR	**Chapter FIVE**	**Chapter SIX**	**Chapter SEVEN**
Subject	Bunsen Burner	Quartz Round Tube	Quartz Round Tube	Acrylic Square Tube
Placement	Place on table	Horizontal	Vertical	Horizontal
Method	Flame Chemiluminces	Flame Chemiluminces	Flame Chemiluminces	Flame Chemiluminces & Schlieren Imaging
Device	High-speed Colour Camera	High-speed Colour Camera & Pressure Sensor	High-speed Colour Camera & Pressure Sensor	High-speed Colour Camera, High-speed Black and White Camera & Pressure Sensor
Key Purpose	To verify the flame chemiluminescence method need	To establish the impact of C_2^* chemiluminescence and pressure	To establish hydrogen concentration influences flame speed and pressure of the propagated flame	To investigate the impact of flame shape on flame oscillation, via the observed schlieren imaging.

4 CHAPTER FOUR: Comparison of Two Hydrocarbon (C_3H_8 & CH_4) Premixed Flames Using a Bunsen Burner

4.1 Introduction

To improve combustion technology, it is necessary to study and discuss the mechanism and status of the combustion process. In order to organise efficient and stable combustion, it is necessary to have a clear understanding of the physical and chemical reaction processes that occur in a burner. The Bunsen burner, named after German chemist Robert Bunsen, was originally an improved coal-gas lamp that allowed coal-gas and air to be mixed in a tube before burning. Modern Bunsen burners are generally gas burners that can pre-mix fuel and oxidants. The maximum flame temperature can reach up to 1500 °C if the mixture is completely burned. The Bunsen burner used in this research can control the flow of methane, propane and air separately, producing flames under different operating conditions to obtain a stable and controllable flame.

The essence of combustion diagnostics is to collect various types of information that can reflect the working conditions of the combustion system. In this case, comparing two typical hydrocarbon (C_3H_8 and CH_4) fuels can help us understand the hydrocarbon flame behaviour. There has been insufficient research around some of the chemical

reaction mechanisms in the combustion process, especially the role of intermediate products. These products are of great interest to researchers, because considering them can help us to more completely describe the process of reaction. The method used here—of utilising the intermediate products produced during the combustion process—is based on the assumption that all hydrocarbon premixed flame chemiluminescence only emits CH^* at 430 nm and C_2^* at 516 nm. CH^* and C_2^* emission concentrations can be referred to as B and G channels. These correspond to 430 nm and 516 nm respectively, as explained in the previous chapter.

4.2 Experiment Setup

The experiment setup consists of two parts—the fuel supply system and the imaging configuration—as shown in Figure 4-1. The fuel supply system comprises two rotameters, controlling the flow rate of fuel and air, and one mixing chamber. One side of the fuel transmission pipeline is connected to the fuel cylinder, which is placed outside of the building. The other side is connected to the fuel rotameter. The air rotameter connects to an air compressor with a pipeline that allows the correct amount of air into the system. Each rotameter has a valve that can be switched open or closed to allow gases to pass through it. Only one fuel rotameter and one air rotameter are connected to the fuel supply system at one time. The two outputs of the rotameters go to the mixing chamber through the same tube. The mixing chamber is installed between

the burner and the rotameters, providing the necessary space to mix fuel and air. For safety reasons, a flashback arrestor was installed between the burner and mixing chamber. This prevents the flame from moving back into the fuel cylinder, avoiding an unexpected explosion.

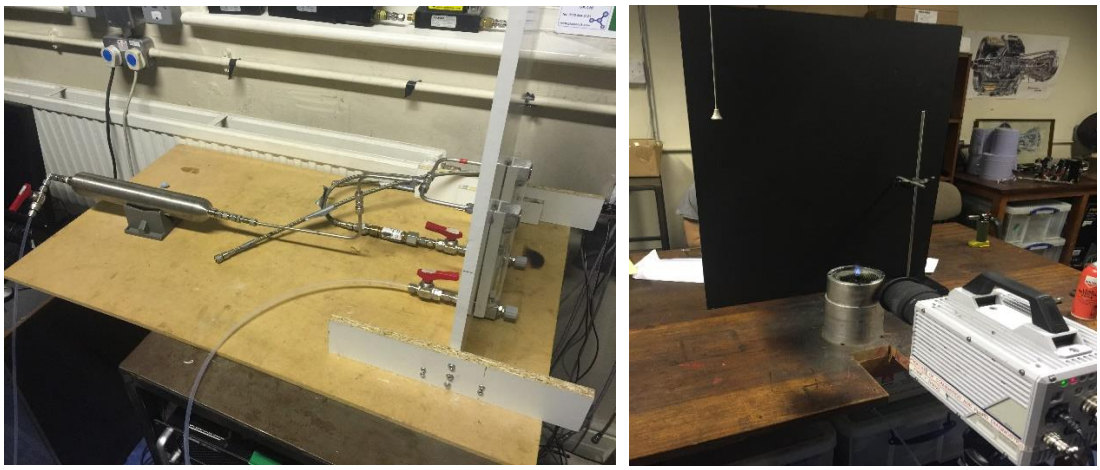

Figure 4-1. Experiment setup: Fuel supply system (left); imaging configuration (right).

Regarding the imaging configuration, a black board is used to reduce background noise during the operation of the imaging system. This also reduces the difficulty of separating the flame and the background during the post-processing stage, which in turn increases the accuracy of the results.

Following the methodology outlined here, the spectrum response of the high-speed imaging system used in this research already evaluated. This allows the proposed image processing measurement to be applied to the premixed flame investigation, irrespective of the uncertainties induced by the imaging hardware. A Bunsen burner placed between the camera and the board can create a stable conical flame.

The flame type of interest is premixed flame. In this case, methane and propane will be mixed with an oxidant (air) to form a stable cone-shaped flame with different flame colouration. The equivalence ratio of the fuel mixture is set from 0.9 to 1.55, with an interval 0.05. This is due to the limitation of the rotameters for both gas supplements, and the size of the burner nozzle. The flow rate of fuel is fixed at 0.09 L/min for C_3H_8 and 0.25 L/min for CH_4. The rate of air supply is then adjusted to achieve the required equivalence ratio settings. Table 4-1 shows the main details of the experimental parameters, which include the fuel system flow rate and the camera settings. The calculations of the full fuel system are shown in the appendix.

Table 4-1. Experiment properties of C_3H_8 and CH_4 premixed flames.

	C_3H_8	CH_4
Fuel flow rate (L/min)	0.09	0.25
Shutter speed (Sec)	1/125	1/50
Frame rate (fps)	125	50

4.3 Results and Analysis

The flame images illustrated here have applied only a denoise program. The function of this denoise program is to separate the flame itself and the background noise through a signal intensity threshold, and remove the signals which not the flame. Figure 4-2 shows the denoised image sequence of propane flame, from equivalence ratio 0.9 to

1.55. The rest of the black area which have no flame were cropped to save present space. The flame colour varies from pure blue to green-blue as the equivalence ratio increases. It is visible to the naked eye that the flame becomes lighter as the equivalence ratio increases. The flame colouration tends to be greenish in the fuel-rich condition, which indicates that C_2^* predominates in the flame emission. The flame shape remains conical at all times.

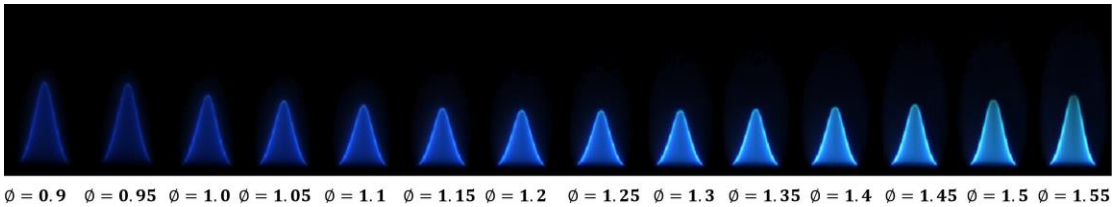

Figure 4-2. Processed C_3H_8 premixed flame images at an equivalence ratio ranging from 0.9 to 1.55.

The colour of the methane flame, however, changes from clearly pure blue to barely visible as the equivalence ratio increases. This is demonstrated in Figure 4-3. Additionally, the flame colour remains nearly consistent, which means the C_2^* emittance changes nuance due to the changes of the equivalence ratio. The structure of the flame remains cone-shaped, but is taller than the propane flame.

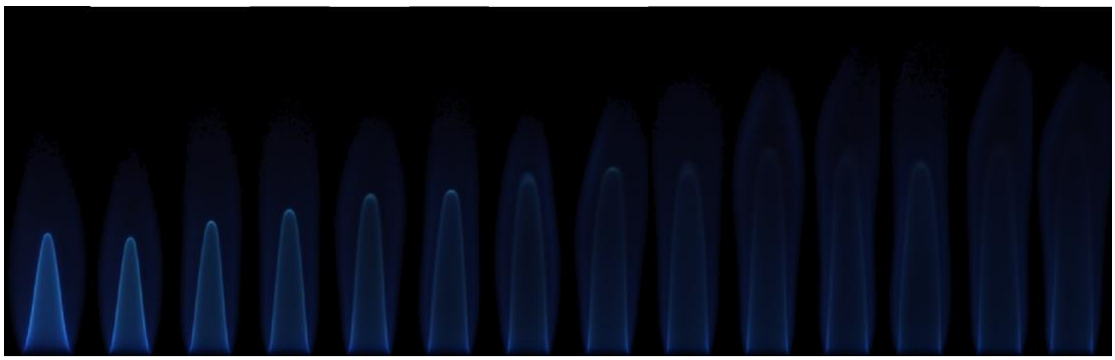

Figure 4-3. Processed CH_4 premixed flame images at equivalence ratios ranging from 0.9 to 1.55.

Applying the proposed image technique to the two previous image sequences, figure 4-4 shows the premixed propane CH^*/ C_2^* chemiluminescence emission ratio maps of the whole flame. The colour map transitions from blue to red, as the concentration of CH^*/C_2^* increases from 0 to 5. The colour of the inner flame which present as conical shape in the figure 4-4 is consistent at certain equivalence ratios, which means that the fuel and air have mixed well in the mixing chamber. For the post-reaction zone, there is not enough evidence to draw a conclusion—although between the inner conical flame shape and post-reaction zone shows consistently red colour which its present ratio of CH^*/ C_2^* around 4.5 as the equivalence ratio varies. The ratio of CH^*/ C_2^* in the C_3H_8 inner flame decreases as the equivalence ratio increases which shows good trend, but the local area, the layer between inner conical flame and post-reaction zone remained red colour which is un-usual although it's not affected the overall trend. The CH^*/C_2^* ratio always increases from the flame base to the top. There is a clear difference in the colour layer between the inner flame and the post-reaction area, which may be the flame front layer.

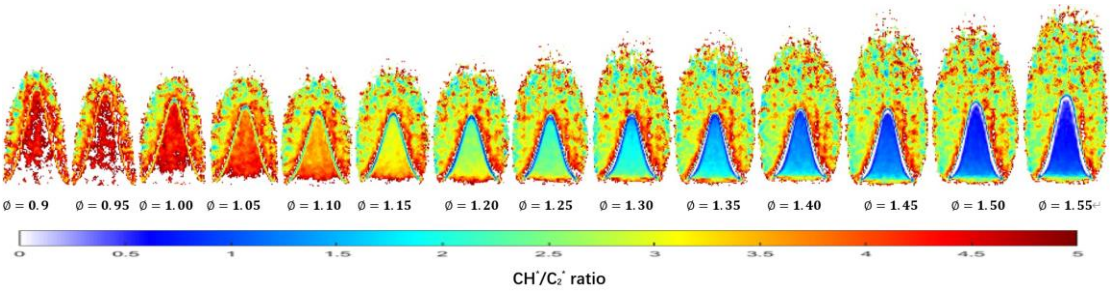

Figure 4-4. Propane CH^*/C_2^* ratio maps at an equivalence ratio from 0.9 to 1.55.

In the case of CH_4 as shown in figure 4-5, the CH^*/C_2^* ratio of the inner flame increases with the increase of the equivalence ratio, which shows an opposite trend to C_3H_8. The border of the inner flame and oxidation of CH_4 blurs as the equivalence ratio increases. A colour difference between the inner flame and the oxidation area can still be observed, however, even if the colour is similar. This means that the flame CH^*/C_2^* ratio may have the potential to identify the flame layer of premixed hydrocarbon flame.

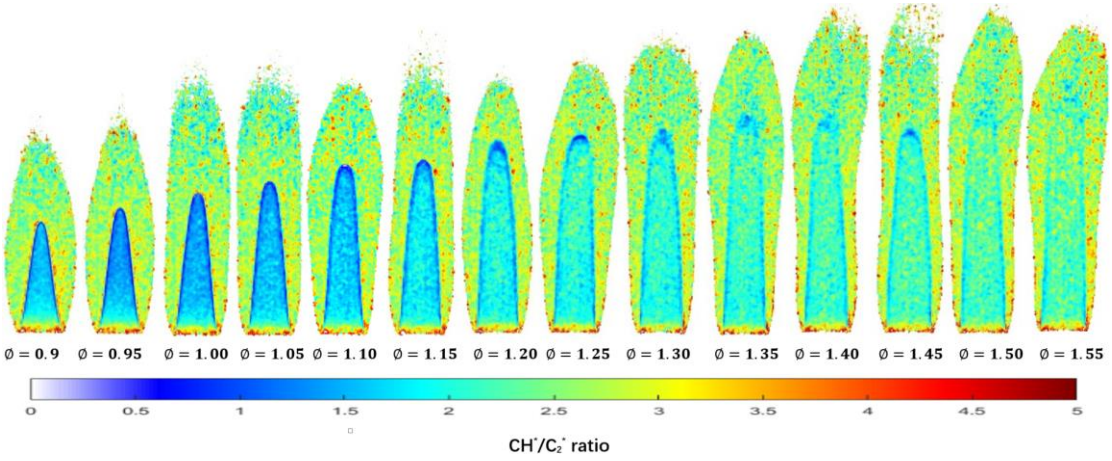

Figure 4-5. Methane CH^*/C_2^* ratio maps at an equivalence ratio from 0.9 to 1.55.

In the case of propane, the CH^*/C_2^* ratio decreases as the equivalence ratio increases, except at the point of equivalence ratio 0.9, as shown in Figure 4-6. The difference of CH^*/C_2^* ratio value between the highest point and the lowest point is approximately 3.4. For methane, the difference between the highest point and the lowest point is

approximately 0.45, and it shows the opposite trend of propane. In both cases, the CH^*/C_2^* ratio has a linear response to the equivalence ratio for fuel-rich conditions.

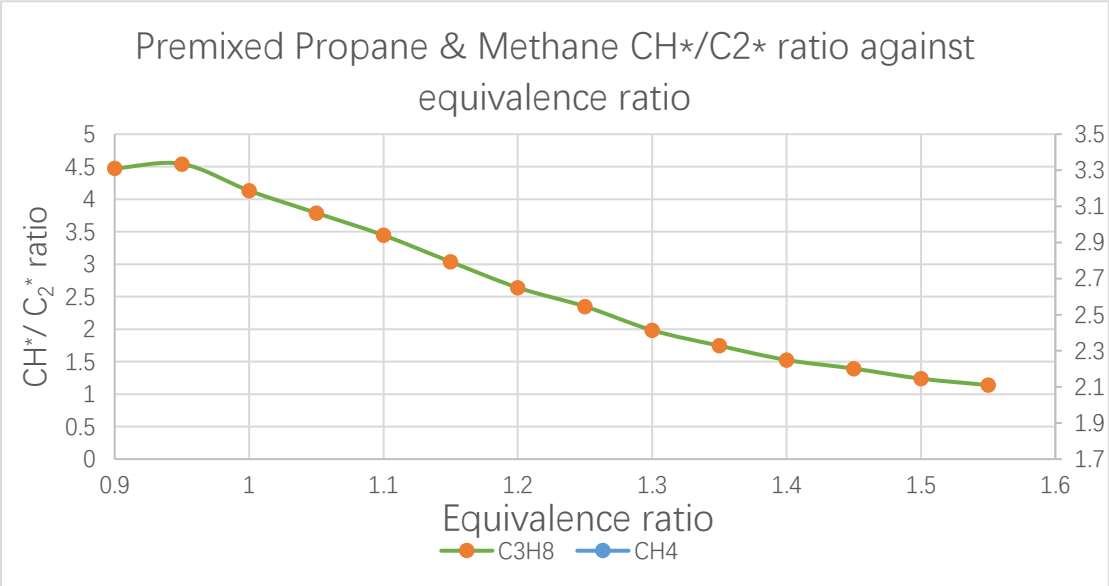

Figure 4-6. Premixed propane and the methane CH^*/C_2^* ratio plotted against the equivalence ratio.

Figure 4-7 shows the CH^* intensity for both fuels used on the primary axis, and the C_2^* intensity of the fuels used on the secondary axis. Comparing the total C_2^* intensity, propane has about four times more in fuel-rich conditions. There are, however, only slight changes for the methane. This is the main reason for the large variation in the CH^*/C_2^* ratio.

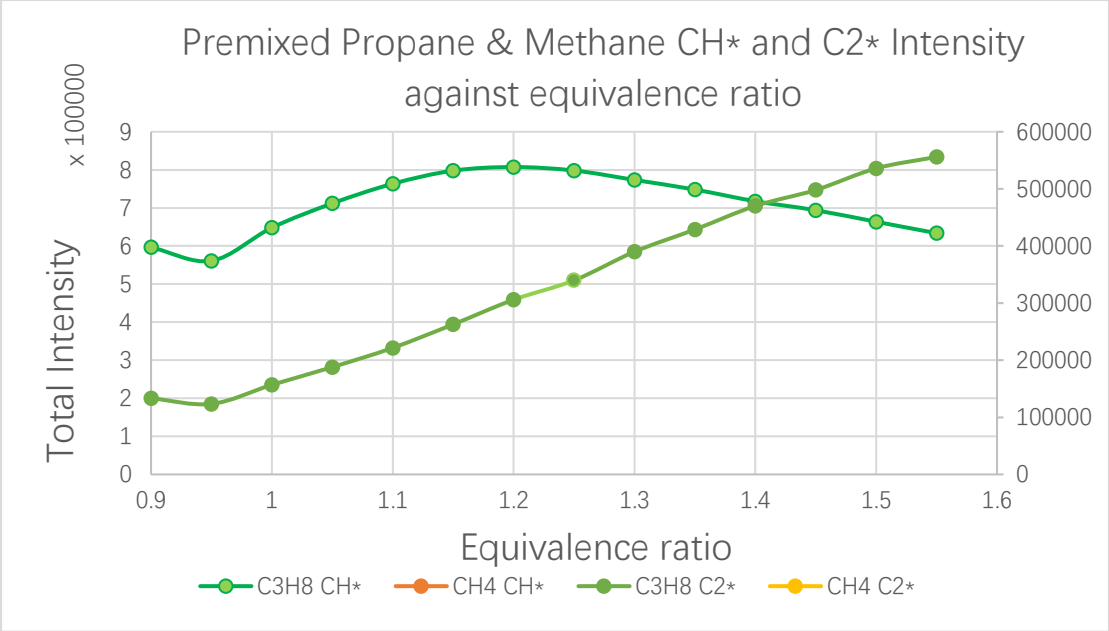

Figure 4-7. Premixed propane and methane CH^* and C_2^* intensity plotted against the equivalence ratio.

As shown in Figure 4-8, both the C_3H_8 and CH_4 flame areas are nearly linear as the equivalence ratio increases. Flame area were sum of flame pixels after the raw image de-noised. When the fuel flow rate is constant, the flame area becomes larger with a slower airflow rate as the equivalence ratio increases. The reason of kept fuel flow rate constant rather than airflow rate constant was because of the limit of rotameter.

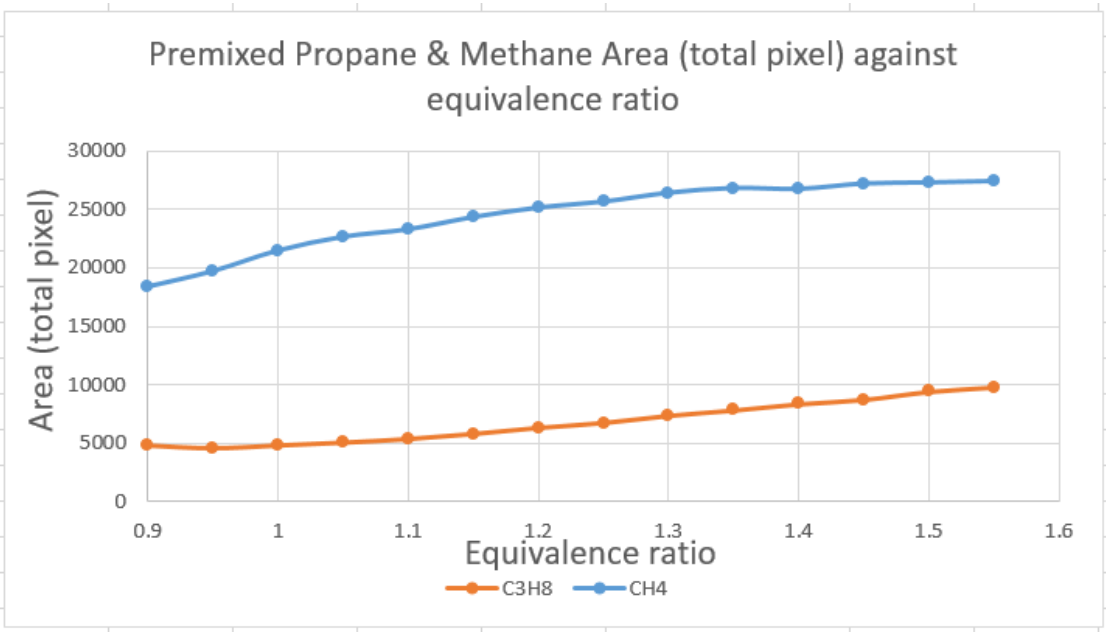

Figure 4-8. Premixed propane and methane area (total pixel) plotted against the equivalence ratio.

4.4 Conclusion

In this case, two typical hydrocarbon fuels, C_3H_8 and CH_4, are compared to investigate flame behaviour. The method used here utilises the intermediate products produced during the combustion process. This is based on the assumption that all hydrocarbon premixed flame chemiluminescence only emits CH^* at 430 nm and C_2^* at 516 nm. The results have been calculated and shown as figures. The main work can be summarised as follows:

In this experiment, the fuel supply system and the imaging configuration are applied, with a flow rate of fuel fixed at 0.09 L/min for C_3H_8 and 0.25L/min for CH_4. The

equivalence ratio is set from 0.9 to 1.55 with 0.05 intervals. Image colour-based flame chemiluminescence measurement was successfully applied in this case, to obtain information about the CH^*/C_2^* ratio. The result shows that, for both methane and propane, the CH^*/C_2^* ratio has a linear response to the equivalence ratio if it is higher than 0.95. The CH^*/C_2^* ratio of propane decreases as the equivalence ratio increases. Methane, however, shows the opposite trend. The findings show the CH^* intensity of propane to be about four times greater in fuel-rich conditions; however, there are only slight changes for methane. This is the main reason for the large variation in the CH^*/C_2^* ratio.

There is not enough evidence to explain why a linear response changes at the equivalence ratio of 0.95. The CH^*/ C_2^* ratio colour map for C_3H_8 case as shown in figure 4-4, the reason of why overall CH^*/ C_2^* ratio shows good trend with equivalence ratio since 0.95 to 1.55, but the layer between the inner conical flame and the post-reaction area consistently shows red colour, which also not affect the overall value were not cleared. To answer these questions, the test range needs to be extended to the flame-burning limit, however it is short of the current experimental rig due to the nozzle size and rotameters limitation issues.

5 CHAPTER FIVE: Premixed Methane / Air / Hydrogen Flame Oscillations in Horizontal Open-Ended Tubes

5.1 Introduction

Flammable hydrocarbon gases are widely utilised in industrial processes. However, during production, transportation, storage and use they have the potential to mix with air, to ignite and to detonate (Bjerketvedt 1997; Dorofeev 2011). Following the ignition of a premixture, the flame initially propagates as a deflagration. Yet, after interaction with the environment, it can accelerate and lead to a denotation (known as Deflagration to Detonation Transition [DDT]). One of the earliest studies of premixed flame propagation was that of Mallard and Le Chatelier, who ignited flames in tubes to examine the problem of coal mining explosion accidents. They demonstrated that significant alterations in the flame propagation rate occurred as the flame travelled down the tube (1883). Other studies went on to investigate flame propagation in tubes, to understand the mechanism of flame movements (Wheeler 1914; Corard 1932; Gerstein 1951; Markstein 1964). The flame vibration has been attributed to induced pressure oscillations that, if in-phase, can satisfy Rayleigh's Criterion (Rayleigh 1896) and result in enhanced burn rates.

In combustion, light emissions from the excited species formed during chemical reactions are known as flame chemiluminescence. Flame chemiluminescence measurements have received increasing attention from researchers, as they can provide useful information on the combustion process in conjunction with high-speed imaging. Huang and Zhang explored C_2^* chemiluminescence intensities utilising RGB colour channels (2008). Yang et al. subsequently applied this method to flame propagation in a tube, demonstrating the impact of pressure fluctuations (2015). Flame propagation down a tube was monitored using simultaneous C_2^* chemiluminescence and pressure measurements. In this study, ϕ =1.2 methane-hydrogen-air (R_H 0.2) flames have been filmed, R_H is a parameter defining the amount of hydrogen concentration in a fuel mixture, which was first implemented by Yu et al. (1986). The details of mixture volumes shown in Appendix 10.3. Flame propagating within a horizontal open-ended quartz tube measuring 1200 mm long with an internal diameter of 20 mm.

5.2 Experimental Setup

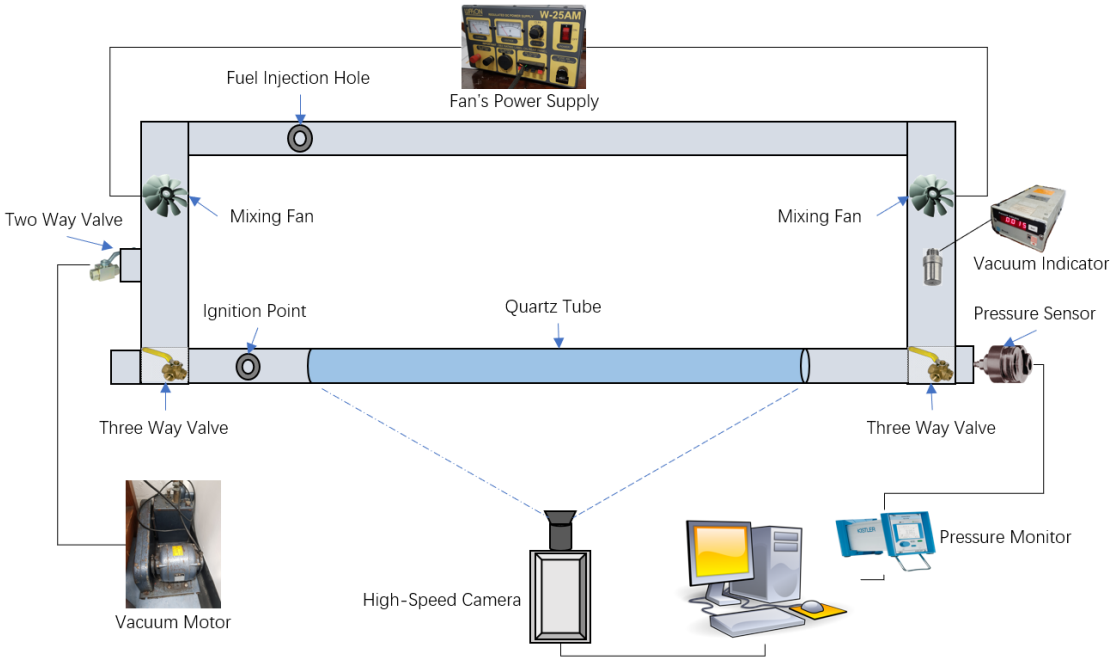

Figure 5-1. Experimental setup schematic drawing.

As shown in figure 5-1, the system is based around a 1200 mm long horizontal tube of 20 mm internal diameter; both ends are open to the atmosphere by changing two three-way valves. The ambient temperature of the lab was approximately 293 K. Following each experiment, the tube was evacuated using a vacuum pump. The required volume of fuel was injected into the apparatus using a syringe, and air was introduced into the rig to bring it to atmospheric pressure. The measurements reported here were performed with methane-hydrogen-air mixtures (R_H 0.2) at equivalence ratio 1.2. The volume of the rig were measured before the experiment, and it was used to calculated the required amount of the fuel to achieved the equivalence ratio requirement. The method of equivalence ratio calculation shown in appendix. This mixture was chosen following

the work of Ebieto et al. (2015), which found that the mixture produced highly oscillating flames. The experiment was repeated 20 times and the result is representative of those runs. The result present here only one of those runs. The mixture was ignited using a propane pilot flame placed at one end of the tube. The reason of not using spark ignition because it has been found to enhance the onset of lame oscillations. The quartz tube provided optical access to allow the flame propagation to be recorded. A Photron SA-4 high-speed colour camera—with a Nikon 35-200 mm, f-3.5 zoom lens; a consistent framing rate of 1000 fps; and a consistent 1000 μs shutter speed—was used to record the flame position. Pressure measurements were also collected using a Kistler Type 7261 piezo-electric pressure transducer, mounted at the end of the tube furthest from the ignition point. The camera and pressure transducer were synchronised.

Colour images were processed using MATLAB code to provide C_2^* emission levels, based on the characterisation of the colour signal emanating from the flame. The combustion C_2^* intensity was calculated from the blue and green channel values in the camera's RGB colour space. It showed good correlation by present the global C_2^* chemiluminescence intensities in a premixed hydrocarbon flame, it was used mean B and G image channel values, verified, and explained in detail by Huang and Zhang (2008).

5.3 Results and Analysis

Figure 5-2 shows the calculated sum of intensity of C_2^* and the pressure signal at the end of the tube. The propagation of the flame was categorised in four stages. Each stage of propagation is associated with different flame shapes, which are displayed in Figure 5-3.

Stage 1: During the first stage, the intensity of C_2^* increased slightly but there was no change in the pressure, which remained at its pre-ignition value. The flame propagated convex to the direction of travel. The convex or flame finger shape is due to the non-slip condition at the wall acting on the burnt gases, as well as to the heat transfer from the reaction zone to the wall (Yu 1986). Its shape was not symmetrical; it displayed a tail at the bottom of the tube, which has been attributed to the effect of buoyancy forces on the flame. This may be an artefact of the ignition method, as non-symmetrical flames have been observed in downwardly propagating flames (Ebieto 2017).

Stage 2: The intensity of C_2^* dropped, corresponding to the flattening of the flame, for example No.717 photograph as shown in figure 5-3. Oscillations can be observed in both the pressure and C_2^*. The maximum amplitude of the pressure oscillation increased with each cycle.

Stage 3: Here the C_2^* and pressure signals achieved their maximum amplitudes. A reduction in flame speed as shown in the third column on the top in the figure 5-3, the flame front positions were used to calculated the flame speed. The reduction in flame speed accompanied by a pressure build-up, initiates the third stage of the propagation: a parametric oscillating flame which first named by Clavin (2000) because the equation used to describe the flame motion is in the form of a parametrically driven damped harmonic oscillator. In the first two frames, No.760 & No.761 photographs as shown in figure 5-3, a long tail forms in the middle of the burned mixture. This may be due to a pressure gradient acting from the unburned to burned mixture, resulting in a Rayleigh-Taylor instability (Ebieto 2017) or tulip flame. Following the creation of the tail, the flame front collapses and becomes a near-spherical ball (see image at 765 ms, in Figure 29).

Stage 4: Here the C_2^* emission remained relatively constant, whilst the pressure levels it decayed down to nearly 0 Pa in Stage 4, similar to Stage 1.

The flame position and pressure histories are illustrated in Figure 5-3. The flame position can be referenced by finding the leading and trailing edges. The lead and trail points were defined here, according to located the first and the last flame signal along the flame propagation direction. During Stage 1 as shown in figure 5-4 (c), the flame propagated at ~2.5 m/s, approximately five times the laminar burning velocity (Gu, Xiao

Jun, et al, 2000). In Stage 2, both the flame and pressure start to pulsate, and the flame flattens as the speed deaccelerates to ~1.8 m/s. The peak pressure reached values of 130 Pa. Flame size reduction, in Stage 2, leads to a decrease in C_2^*. At its maximum point, the pressure achieves 895 Pa as shown in figure 5-4 (d) and the flame attains a maximum propagation speed of 4.5 m/s as shown in figure 5-4 (c). Performing a fast Fourier transform on both the distance amplitude and C_2^* signals revealed that the oscillatory components have frequencies of ~ 245 Hz. The pressure starts to decay beyond this point, and the shortening of the tulip flame length ultimately slows the front of the flame to -0.17 m/s, although the back of the flame continues to propagate forward. The intensity of C_2^* reduces at this point. The flame speed then increases back to the initial propagation speed of ~2.5 m/s shows in figure 5-4 (c), and as shown in figure 5.4 (d) the pressure within the tube stops oscillating.

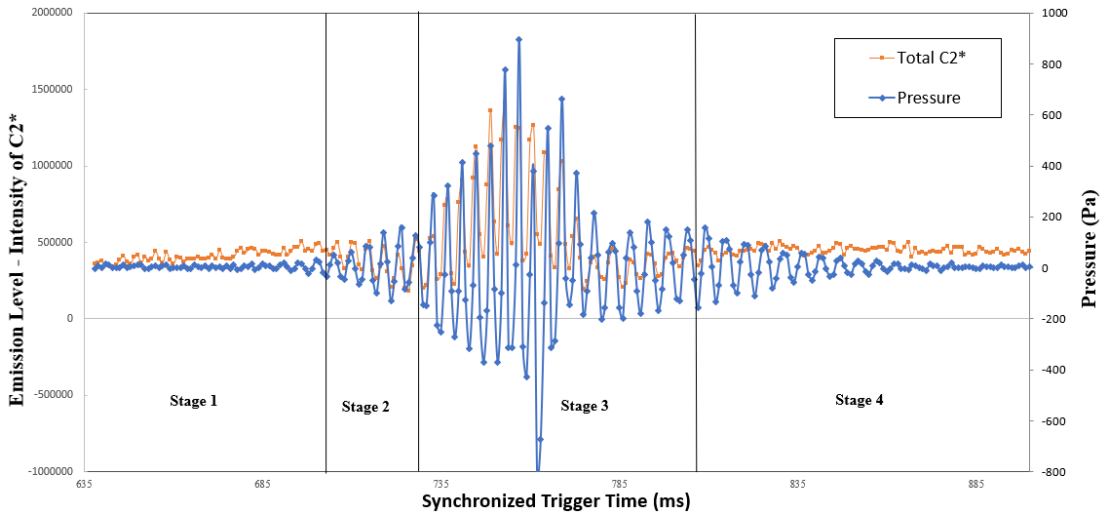

Figure 5-2. Calculated total intensity of C2* and pressure during the flame propagation.

Figure 5-3 shows the sample image sequence of each propagation stage and its respective time after the camera is triggered. The unburnt black area of all images was

cropped for clarity. The RGB channel values were selectively enhanced by multiplying the identified flame pixel 30 times, for presentation.

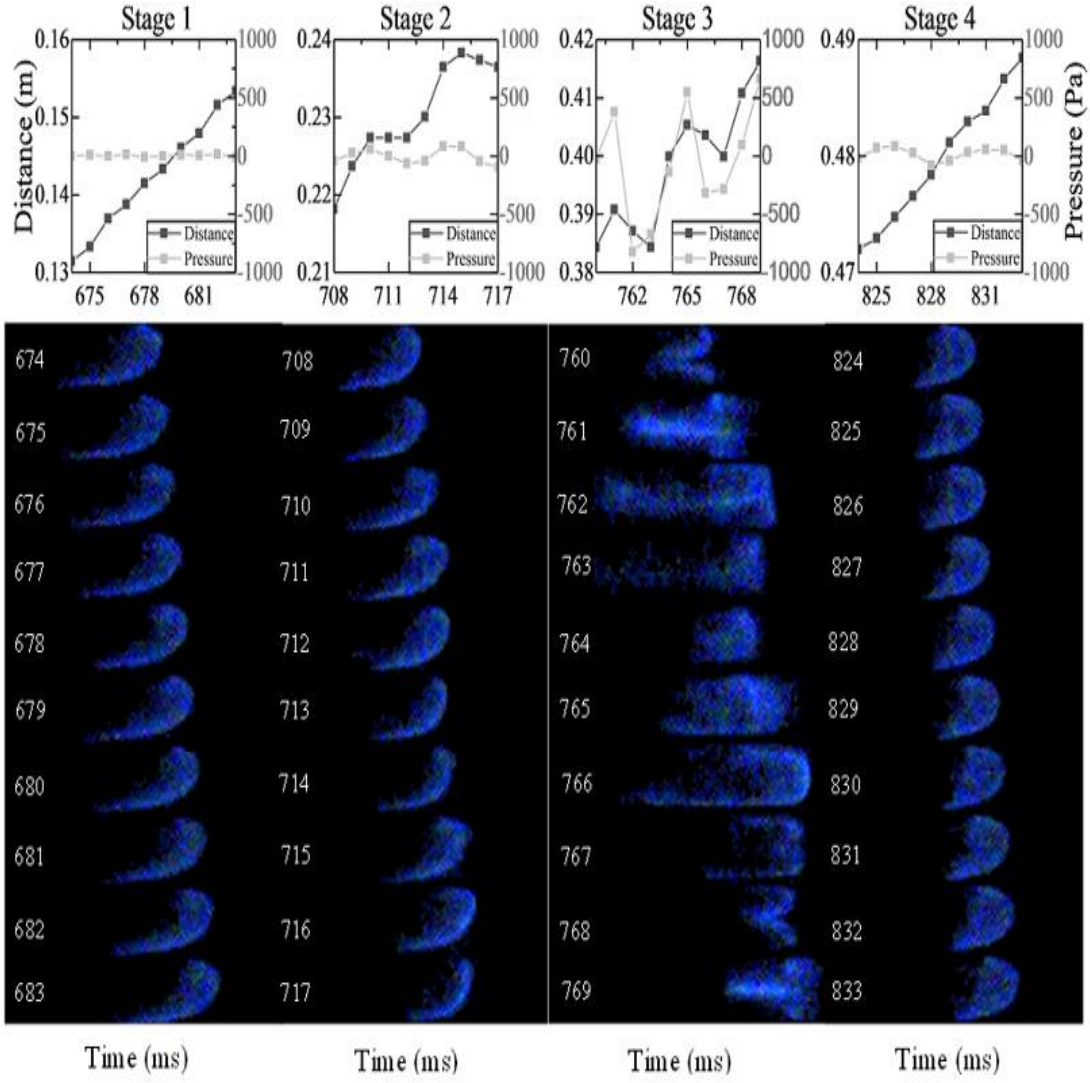

Figure 5-3. Sample image sequence of all stages with their respective time, pressure, and distance. The unburnt black area of all images was cropped for clarity. The RGB channel values were selectively enhanced by multiplying the identified flame pixel 30 times, for presentation.

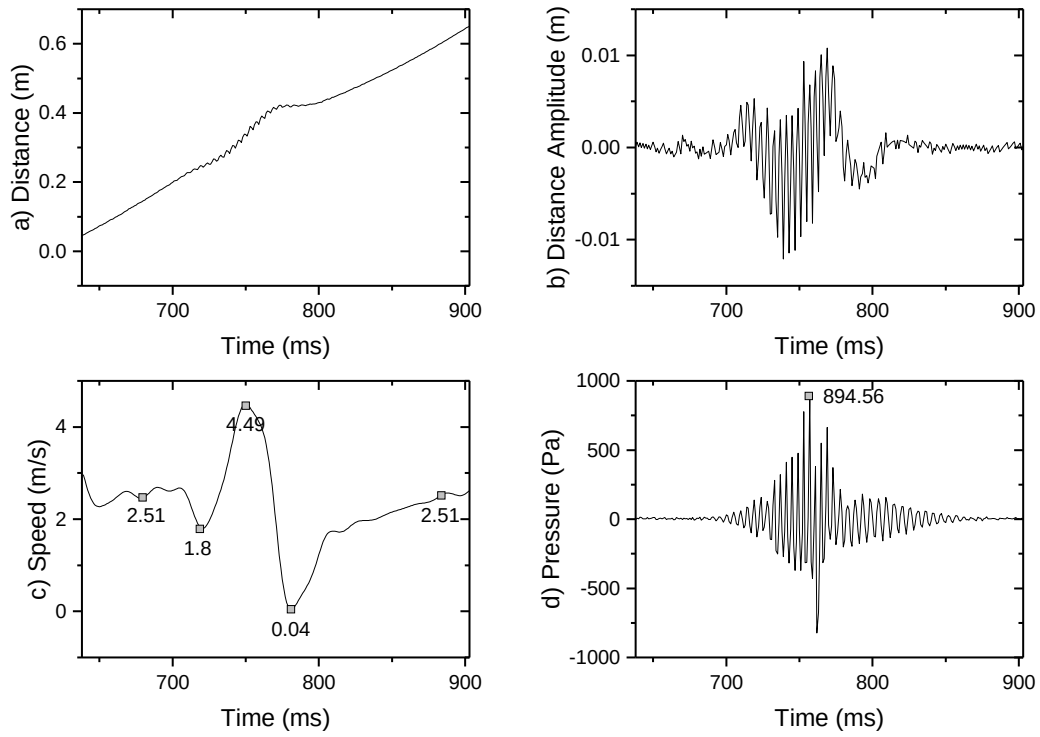

Figure 5-4 (a) Distance of flame front; (b) distance amplitude; (c) flame speed, calculated based on the flame front position; (d) pressure data.

A variety of behaviours are displayed by the flame as it passes through the self-generated pressure field. The position and frequency of the oscillation are artefacts of the tube. They would change if a different tube length was used (Clanet 1996). If a different mixture was ignited, however, the position and frequency would stay broadly the same (Clanet 1996). The magnitude of the pressure and the resulting movement of the gas column are consequences of the interaction between the pressure fluctuations and the flame. To further investigate the interaction, the phase difference between the pressure signals and the flame was determined. The existence of a similar oscillatory frequency in the flame front, tail, C_2^* and pressure show the existence of a coupling

interaction. A Hilbert transform was applied to the time signals to extract their phase information. Prior to performing the Hilbert transform, the oscillatory components need to be isolated from the wideband frequency that exists within the time signals, to remove the contribution from other frequency bands (Cohen 2014).

A 20th order finite impulse response band pass filter (cut-off frequency 100 Hz and 300 Hz) was used to isolate the ~245 Hz oscillation observed in the time signals. The reason of chosen 100 Hz and 300 Hz as cut-off frequency which not critical, but it was a required parameter. A Hilbert transform was then performed and the phase information for the flame front, tail, C_2^* intensity and pressure were obtained. The pressure phase was used as the reference, producing three plots of phase difference, as shown in Figure 5-5: pressure-front, pressure-tail and pressure- C_2^* intensity. The fluctuating phase in Figures 5-5(a) and 5-5(c) represent the different stages discussed previously. The coupling in Stages 2 and 3 was confirmed by the minimal phase fluctuation at ~ 0°, while Stages 1 and 4 were decoupled, as indicated by the high phase difference fluctuation. The coupling in Stages 2 and 3 cannot be observed in Figure 5-5(b), however, indicating that the flame tail does not couple with the pressure fluctuations.

The phase difference against pressure amplitude was plotted—as shown in figures 5-5(d), (e) and (f)—to observe the impact of the phase difference on the pressure amplitude, per Kim et al. (2011) and Coats et al. (2010). It can be seen, in Figures 5-

5(d) and 5-5(f), that—whenever the phase difference falls within 90° (in-phase)—the pressure amplitude starts to amplify. It dampens whenever it is beyond 90° (out of phase). Figure 5-5(e) shows that the flame tail does not couple with the acoustic field.

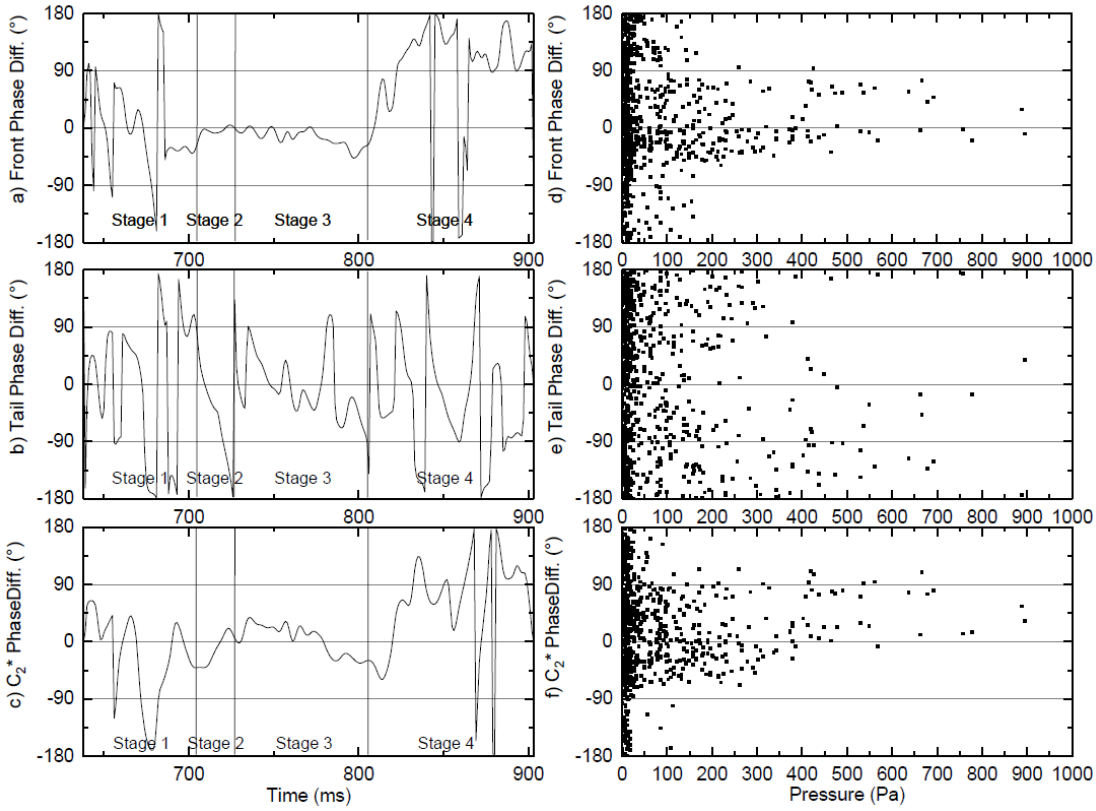

Figure 5-5. Flame-pressure phase difference: (a) flame front; (b) flame tail; and (c) flame C_2^* intensity. Compilation of flame pressure phase difference against pressure amplitude: (d) flame front; (e) flame tail; and (f) flame C_2^* intensity.

As the flame enters the acoustic field, it falls into phase with the pressure fluctuations. As the flame progresses and the pressure amplitude increases, there is a significant impact on the flame shape. Whilst the flame front position and C_2^* intensity (which depends on the flame area) fluctuate in-phase with the pressure oscillations, the rear of the flame does not. The action of the pressure waves pushes spikes of unburned mixture

into burned gas; this mixture can take time to burn and is not impacted by the pressure wave induced fluctuations. This is likely to be the cause of some of the spikes in peak pressure observed in Figure 5-4 (b), resulting in unexpected large pressures. The local pressure gradient is not discussed in this case.

5.4 Synchronization Devices Time Delay Study

Time delay is the time required for a signal to travel through the system. All devices relating to signal transition have a delay. It is difficult to measure the time delay of a single device because it requires knowing the exact time the signal enters the electronic element. The measurement system applied, in this case, includes two hard devices and three difference conditions during the experiment that may cause a signal delay: the transition of the pressure signals from the flame itself to the pressure sensor (pressure signal reception delay), the distance between the flame light and the high-speed colour camera (light signal reception delay), and the signal transmission between the devices (signal transition delay).

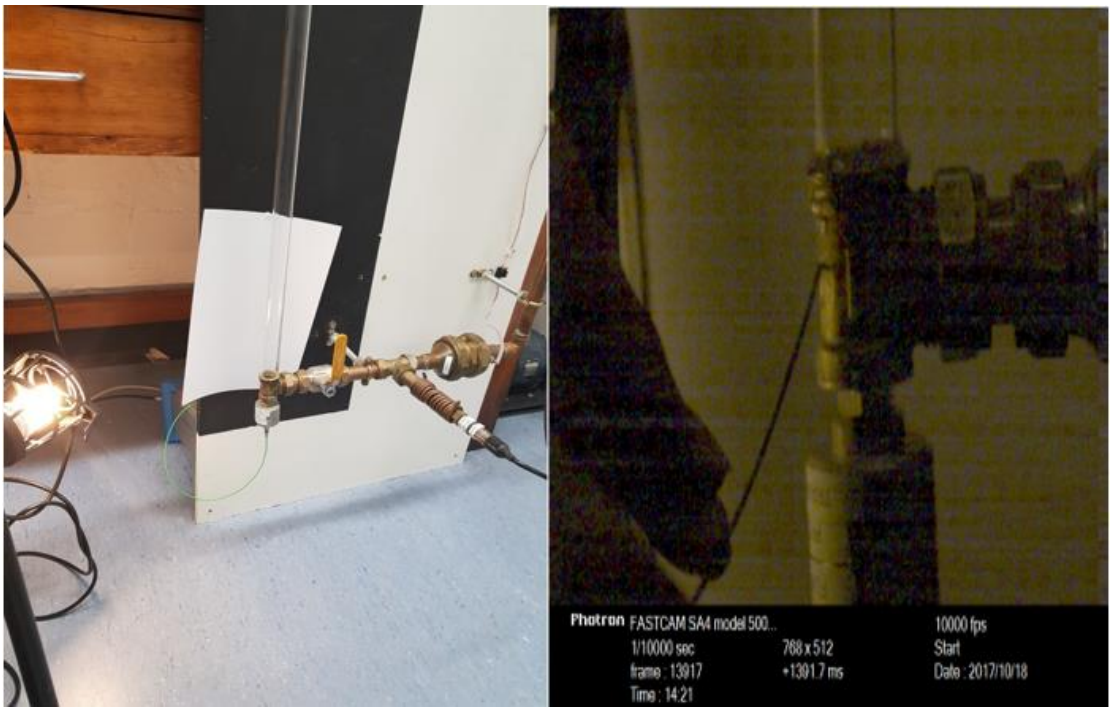

Figure 5-6. Time delay set-up (left); captured image (right).

For both pressure signal reception delay and light signal reception delay can be calculated. Hence signal transmission between the devices need to be measured. Figure 5-6 (left) shows the experiment setup, the experiment was designed to use a metal wire to hit the point covering the pressure sensor to create a signal, and a high-speed colour camera to capture the moment it was hit. Both the pressure sensor and the high-speed colour camera are synchronised by a synchronisation box that runs using LABVIEW and is activated by a trigger, a light source applied here to enable the high-speed colour camera to reach the highest possible frame rate with supplementary shutter speed. In this case, the camera was set to 10,000 fps and 1/10,000 sec of shutter speed. As shown in the figure 5-6 right side was the moment that pressure sensor was hit by the metal wire, which is the moment of pressure signal receipted by the pressure sensor. The

image quality is less important, once this moment can be identified. To check both the captured images and the pressure data, the signal transmission between the devices has an average 0.2 ms time delay. The speed of sound in this experimental condition was calculated at 362.6 m/s, the details of which are found in the appendix. When the flame starts oscillation, the pressure fluctuations then may cause tulip flame which the purposed of this case. Hence, choose flame starts oscillation location as measure end to calculated the pressure signal reception delay is appropriate. The distance between the measure end to pressure sensor about 67.5 cm. The time delay calculation is 1.86 ms for the flame sound wave to reach the pressure sensor. The delay of the high-speed camera capturing the images is assumed to be zero, because the speed of light is much faster than the current unit of magnitude.

However, the speed of sound travelled the mixture of gases related to temperature, pressure, and the mixture concentration. During the experiment, the mixture concentration is continually changing because of the flame oscillations. The temperature also changes, while the distance from the flame to the pressure sensor becomes shorter as the flame travels down to the tube. It is thus difficult to calculate an accurate time delay number for this. The sum of the time delay around 2 ms based on the calculation and experiment detection, however the minimum recording unit for colour camera was millisecond, and the minimum recording unit for pressure sensor was microsecond. If this un-accurate time delay 2 ms applied, the result may become

completely different which may cause one un-certain parameter in the result. Hence, the time delay was considered but not applied.

5.5 Conclusions

A study was conducted to determine the relationship between C_2^* chemiluminescence and pressure oscillations using an open-ended tube measuring 1200 mm long with a 20 mm internal diameter. A quartz tube was used to provide optical access for high-speed colour imaging, and a pressure transducer was utilised to collect the pressure signal at the end of the tube. The main conclusions of the study are:

1. Four stages were identified: curved flame, flattened flame, parametric flame (maximum oscillation) and normalising flame.

2. The measured C_2^* emissions have similar fluctuations with the measured pressure as the flame traverses down the tube. The results present the coupling interaction between flame chemiluminescence and pressure. The two signals are in-phase in Stage 2. The C_2^* and pressure reached maximum oscillation in Stage 3.

3. The fluctuations in the flame front position and C_2^* were found to vary in-phase with the pressure fluctuations. The observed flame position at the rear of the flame

was not in-phase with the pressure, although the complex flame shapes that were observed were caused by the pressure and flow oscillations. This is thought to result in some of the observed sudden jumps in the peak pressure.

6 CHAPTER SIX: Methane/Air Mixture in Fuel-Rich Conditions Mixing with Hydrogen Flame Propagation in a Vertical Tube

6.1 Introduction

Premixed flame propagation is a process that involves the interaction of fluid dynamics and complex chemical reactions. As discussed in previous chapters, the premixed flame propagation process is affected by many factors: fuel properties, pipe size, wall conditions, obstacles and whether the tube ends are opened or closed. Most studies focus on the propagation characteristics of single gas premixed flames in horizontal tubes; fewer people investigate vertical tubes and different fuel mixtures. In the past, flame propagation in a vertical tube has been shown to have a wider flammability limit (Ebieto 2017), which is affected by gravity. Coward H.F and G.W. Jones (1952) defined the flame flammability limit, as measured by a vertical tube. Nearly all laboratory flames are strongly affected by the gravitational field generated by earth. In this case, the effect of gravity will be changed from 90 degrees of the flame propagation direction, to reflect the flame propagation direction that would occur in a vertical tube.

6.2 Experiment Setup

Figure 6-1 illustrates the vertical placement of the rig. The system is based around a 1200 mm long quartz tube with a 20 mm internal diameter, placed vertically with its upper end open to the atmosphere during experiment, and bottom end remain closed. The same quartz tube described in Chapter Five was used, to provide optical access and allow the flame propagation to be recorded. Pressure measurements were also collected using a Kistler Type 7261 piezo-electric pressure transducer mounted at the bottom end of the tube, it was installed furthest from the ignition point. It was installed inside the closed end, as shown at the bottom of Figure 6-1. The ignition used as same as previous chapter was propane fuel spark lighter. The ambient temperature of the lab was approximately 293 K. Following each experiment, the tube was evacuated using a vacuum pump. The loop was closed, then required volume of fuel was injected into the apparatus using a syringe and air was introduced into the rig, to bring it to atmospheric pressure. A Photron SA-4 high-speed colour camera—with a Nikon 35-200 mm, f-3.5 zoom lens, a framing rate of consistent 1000 fps and a consistent 1000 μs shutter speed—was used to record the flame propagation progress. The camera was placed in front of the tube, and a black board used to reduce background noise. To avoid unexpected light entering the camera, all screens and the laboratory's lights were turned off during the experiment. The camera and pressure transducer were synchronised through a synchronisation box.

Figure 6-1. Experiment setup using a vertical tube.

In the previous chapter, the relationship between the C_2^* chemiluminescence and the pressure oscillations in a premixed methane/air/hydrogen flame in horizontal open-ended tubes was present under one condition. In this case, not only were highly oscillating flames captured, but also runs with equivalence ratios in fuel-rich conditions from 1.1 to 1.5 with 0.1 intervals, with hydrogen addition used in this case were from 0% to 40% at 10% intervals, and the details as shown in appendix. The purpose of this

case study was to demonstrate the hydrogen effect on flame propagation in vertical tubes.

6.3 Result and Analysis

Figures 6-2 to 6-6 demonstrate the flame front position (m), plotted against the flame propagation time (s) from equivalence ratio 1.1 to 1.5 with 0.1 intervals. Each graph shows the hydrogen addition at 10% intervals: 40% (dark blue circle), 30% (light blue plus), 20% (yellow cross), 10% (grey triangle) and pure methane/air mixture without hydrogen (orange square). Due to limitations caused by the tube length and the camera position, the maximum captured flame front position is 0.7 metres.

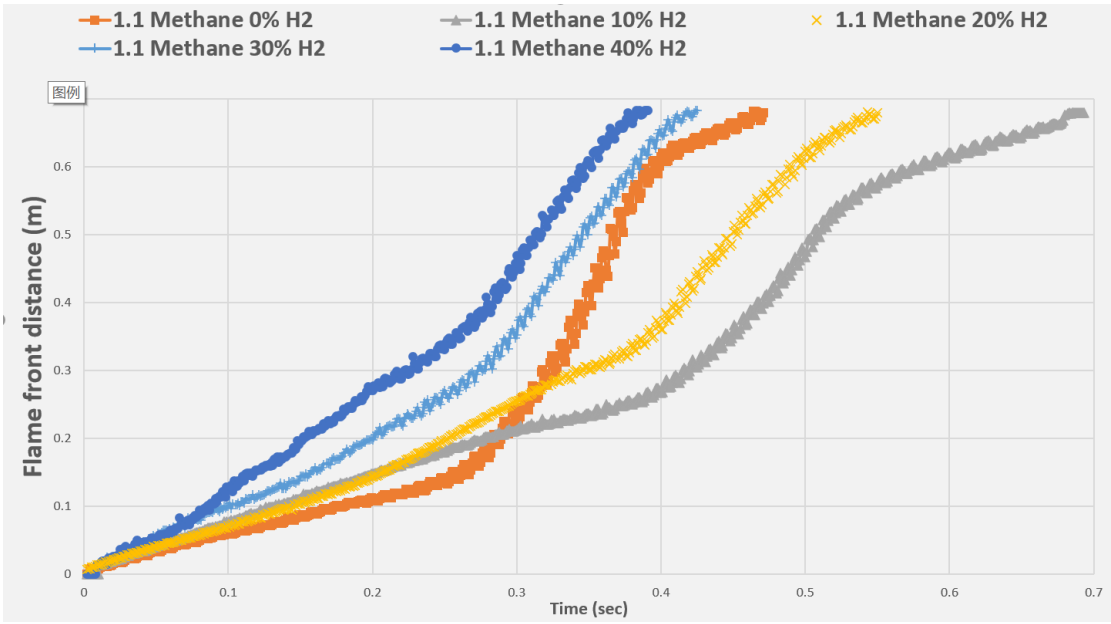

Figure 6-2. Flame front position plotted against time for a vertical tube at the equivalence ratio 1.1

methane/air with different hydrogen additions.

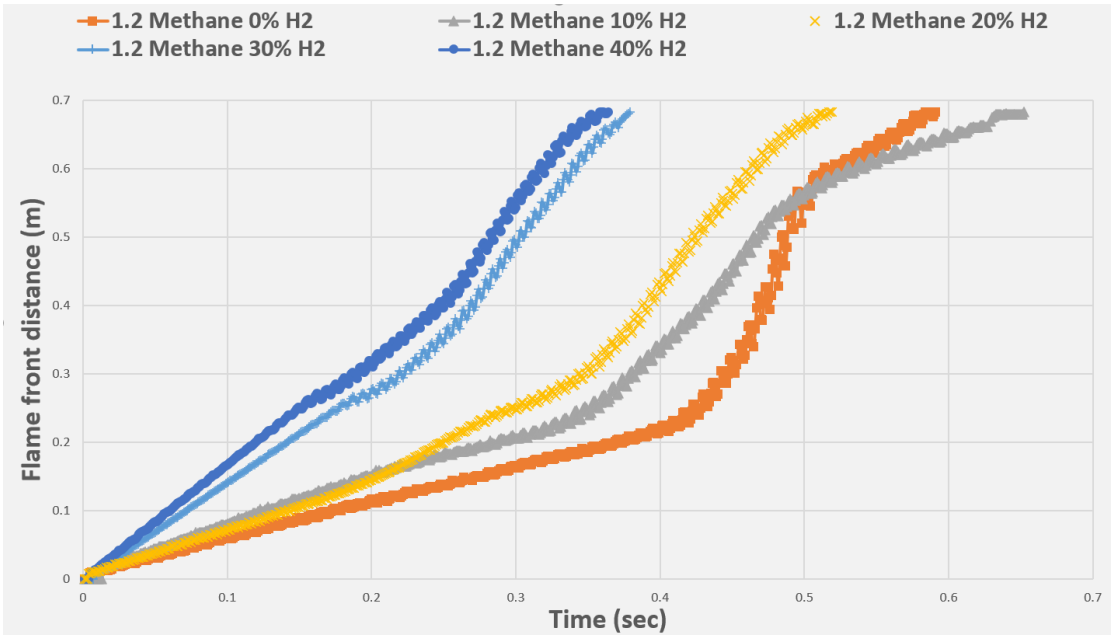

Figure 6-3. Flame front position plotted against time for a vertical tube at the equivalence ratio 1.2

methane/air with different hydrogen additions.

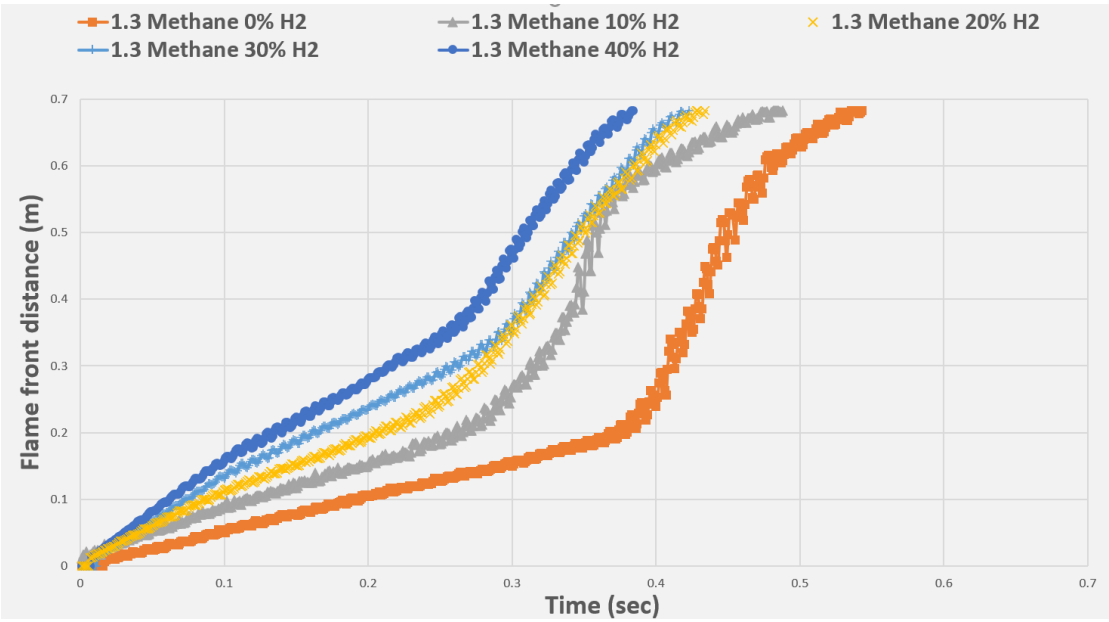

Figure 6-4. Flame front position plotted against time for a vertical tube at the equivalence ratio 1.3

methane/air with different hydrogen additions.

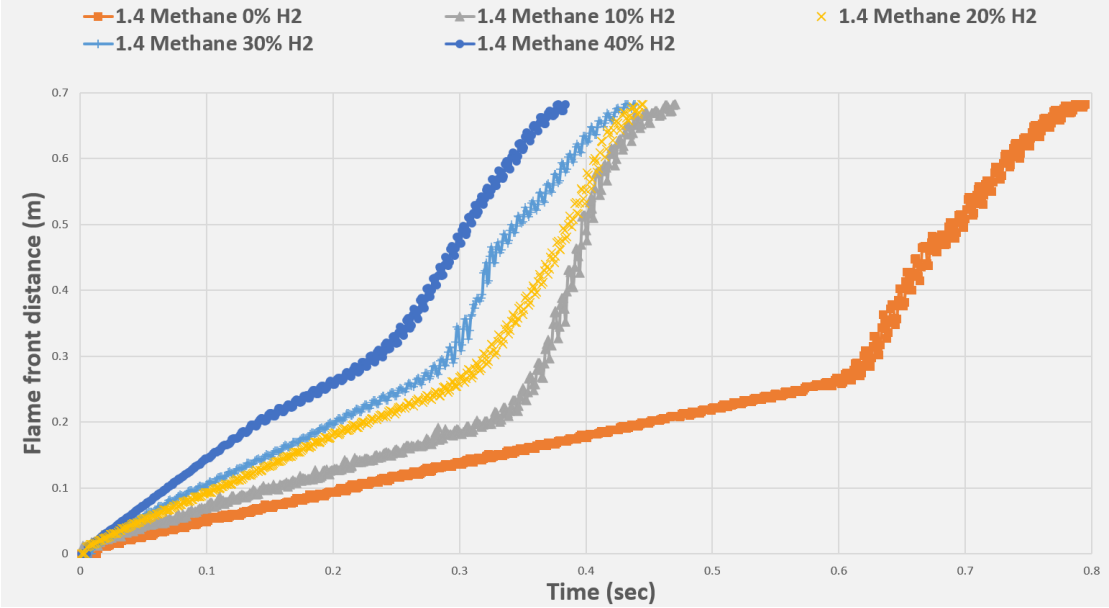

Figure 6-5. Flame front position plotted against time for a vertical tube at the equivalence ratio 1.4 methane/air with different hydrogen additions.

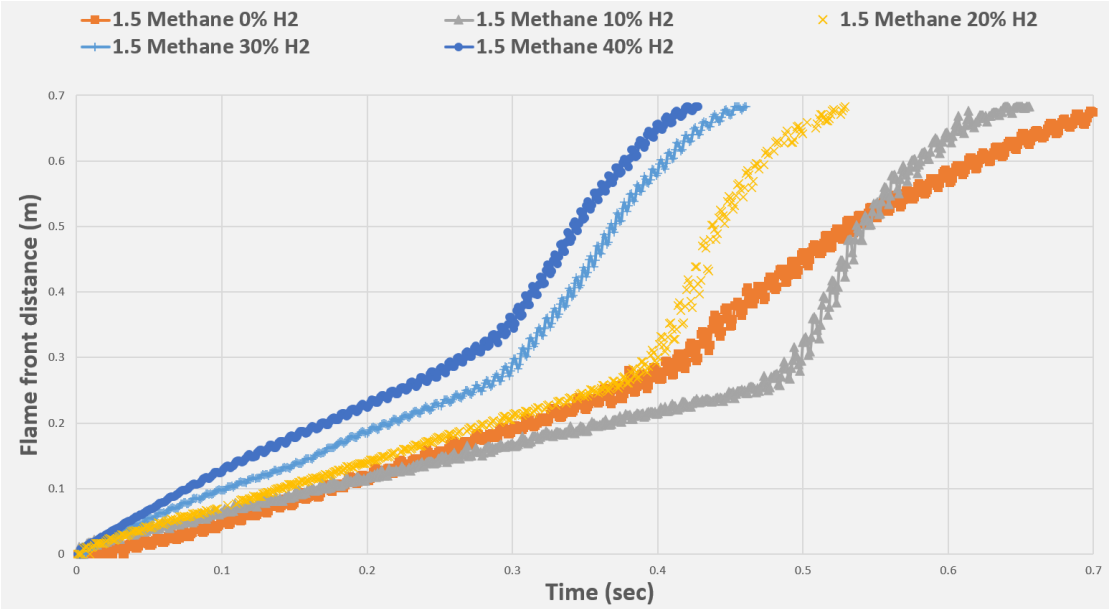

Figure 6-6. Flame front position plotted against time for a vertical tube at the equivalence ratio 1.5 methane/air with different hydrogen additions.

In fuel-rich conditions, self-induced flame turbulence was observed for all the runs, causing difficulty in measuring the position of the flame front. Therefore, once flame itself location has detected, no matter how was the flame shape, the pixel(s) that appeared the farthest in front of the propagation direction, and that were not noise, were used to indicate the flame front point. The flame front position was then calculated via comparison with the reference picture, which measured tube length.

	0%	10%	20%	30%	40%
1.1	0.472s	0.693s	0.55s	0.424s	0.389s
1.2	0.591s	0.652s	0.517s	0.379s	0.364s
1.3	0.536s	0.482s	0.428s	0.423s	0.383s
1.4	0.787s	0.47s	0.44s	0.431s	0.384s
1.5	0.708s	0.647s	0.529s	0.46s	0.426s

Table 6-1. Flame propagation time at varying equivalence ratios and H_2 additions.

The time used from the flame front position, propagated to the captured end (which limit of camera capture range) of the vertical tube, is shown in Table 6-1. This is also illustrated in Figure 6-7. As shown in table 4, the 40% hydrogen addition used the shortest time to travelled the tube which means it has fastest average speed of flame propagation in fuel-rich conditions. For all the runs except equivalence ratio 1.1 and 1.2 pure cases (without hydrogen addition), the time of flame propagated to the limit of camera capture end used shorter as the hydrogen addition increases, which mean the average flame speed increase as hydrogen addition increases. In these instances of

equivalence ratio 1.1 and 1.2 pure cases, the line of 20% of hydrogen addition is slightly lower than the 10% line at the first 0.2 s of flame propagation.

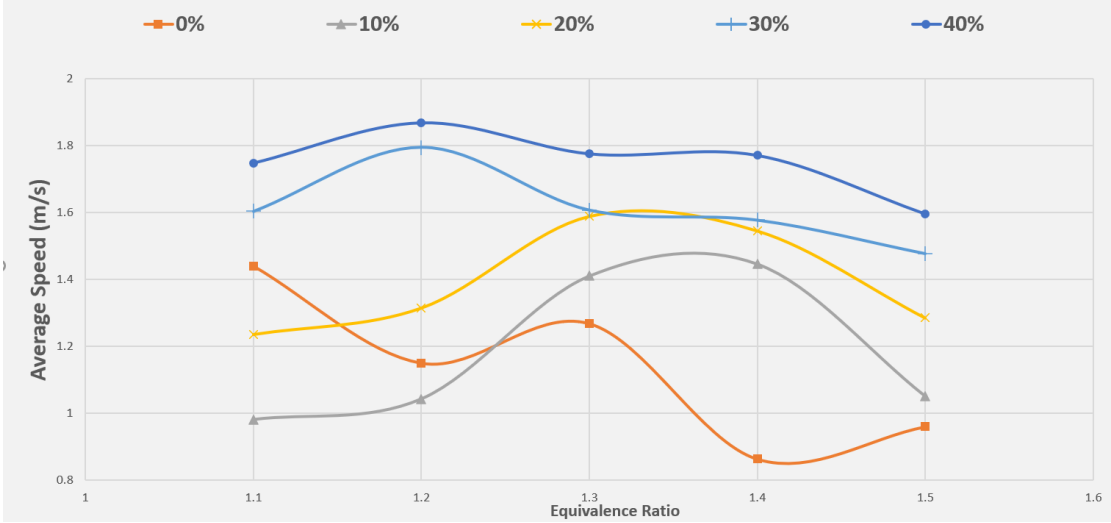

Figure 6-7. Average speed of flame propagation, calculated by propagation time at all conditions.

Figure 6-7 shows that the average speed, with 40% hydrogen additions, is always faster than under other conditions. It follows that, for higher concentrations of hydrogen addition, the average speed of flame propagation is faster. The pure methane/air case study reveals a different trend with hydrogen addition cases at equivalence ratio 1.1 and 1.2 conditions. The peak average speed of pure methane/air is at a 1.1 equivalence ratio. The trend of average speed in pure cases decrease, as the equivalence ratio increases in fuel-rich conditions.

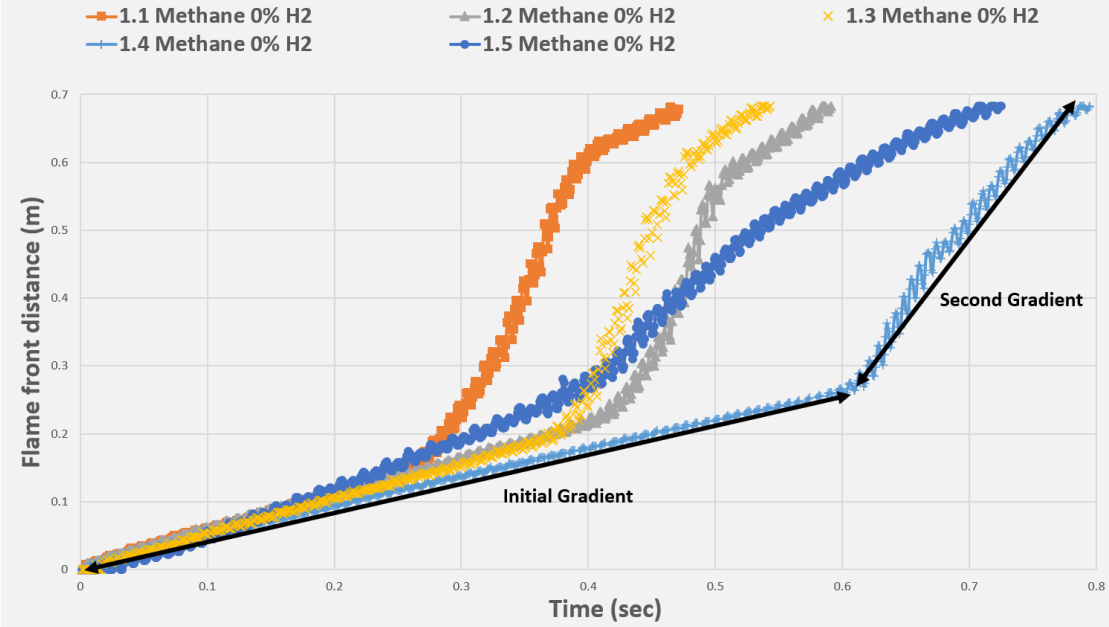

Figure 6-8. Flame front position plotted against time, using pure methane/air.

The average time shows only the approximate situation of the flame propagation; it cannot describe the details of the process. Hence, the speed was calculated by separating the flame propagation behaviours into two different conditions: pulsating flame propagation (initial gradient) and oscillation flame propagation (second gradient). Figure 6-8 shows an example of how to define these two behaviours. The figure shows the flame front position, plotted against time in a fuel-rich environment without the addition of hydrogen. From this, it is possible to see that the lighter blue line has two very different behaviours, which are marked by two-way arrows. Each trial has a similar initial speed, but they become different once oscillations start (i.e., the start of the second gradient stage). The flame propagation begins at a certain propagating speed as the initial gradient. The behaviours of the flame then change to a different oscillation from steady propagation to un-steady propagation as a second gradient. Utilising the

point between the two-way arrows to calculate the speed, before and after the behaviour changes, allows us to better understand the sudden changes in flame speed and it has protentional to help us find the method of suppression. For example, install a 'stop' device (something can stop the flame propagation) at the sudden change point to reduce the design of pipeline pressure limit to prevent further sudden changes of speed.

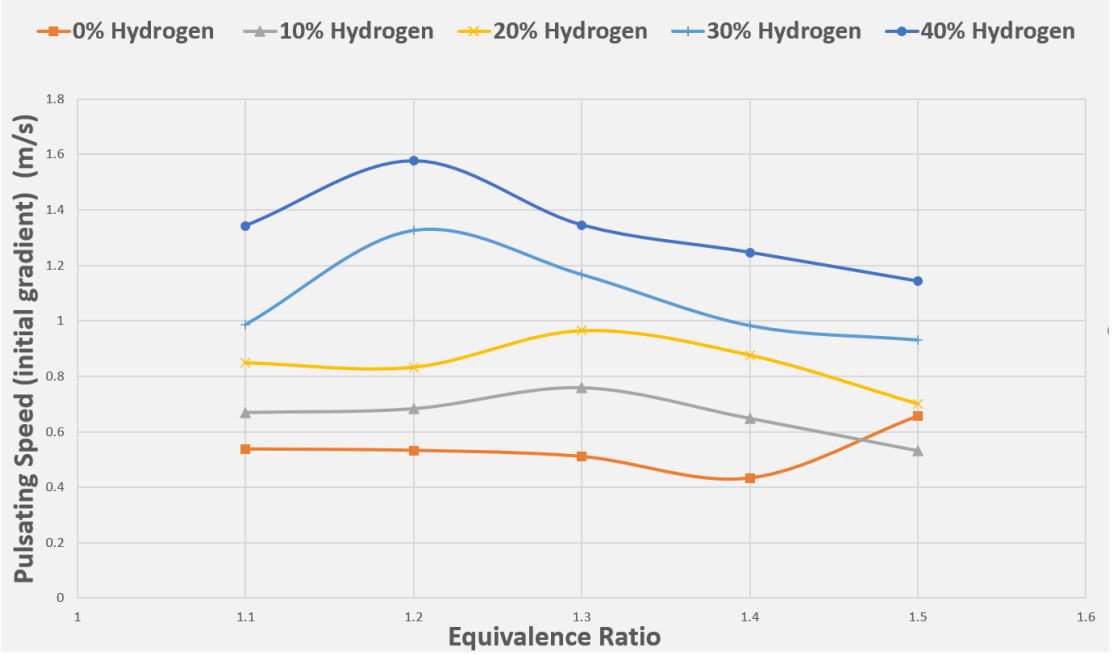

Figure 6-9. Flame speed during pulsating behaviour (initial gradient).

The flame speed of the initial gradient propagation, at each equivalence ratio for all hydrogen additions, is plotted in Figure 6-9. The lower hydrogen additions for vertical flame propagation lead to a reduced pulsating flame speed for all fuel-rich conditions. The minimum speed (0.43 m/s) occurred at equivalence ratio 1.4, without the addition of hydrogen. The maximum speed (1.58 m/s) occurred at equivalence ratio 1.2, with 40% hydrogen addition.

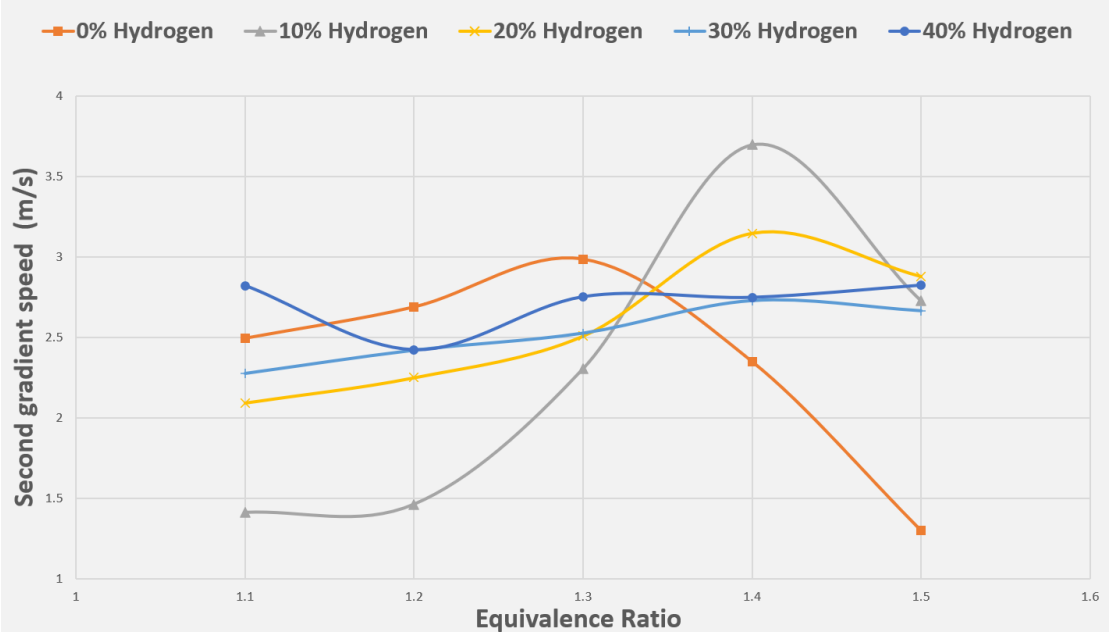

Figure 6-10. Flame speed at second gradient speed.

The flame speed of second gradient propagation at each equivalence ratio, for all hydrogen additions plotted, is in Figure 6-10. For pure methane/air runs, the speed increases up to equivalence ratio 1.3, then slows down until 1.5. For 10%, 20% and 30% hydrogen additions, the oscillation speed increases up to equivalence ratio 1.4, then is slower at 1.5.

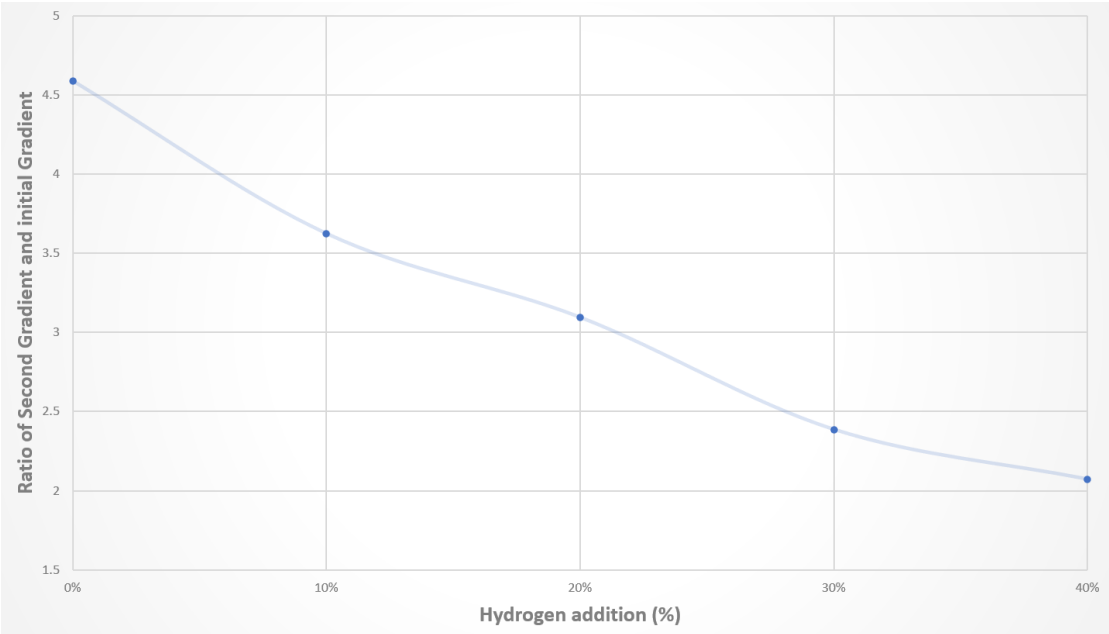

Figure 6-11. Ratio of oscillation gradient and initial gradients.

The ratio of the average oscillation gradient and average initial gradient has been calculated as shown in Figure 6-11. The maximum ratio of second gradient and initial gradient is at 0% hydrogen addition and the minimum ratio is at 40% hydrogen addition. The average value shows a linear decrease as the addition of hydrogen increases. This means the maximum speed difference happens in cases of pure methane/air. This may be a useful parameter, to determine how hydrogen affects the hydrocarbon fuels propagated in a pipeline.

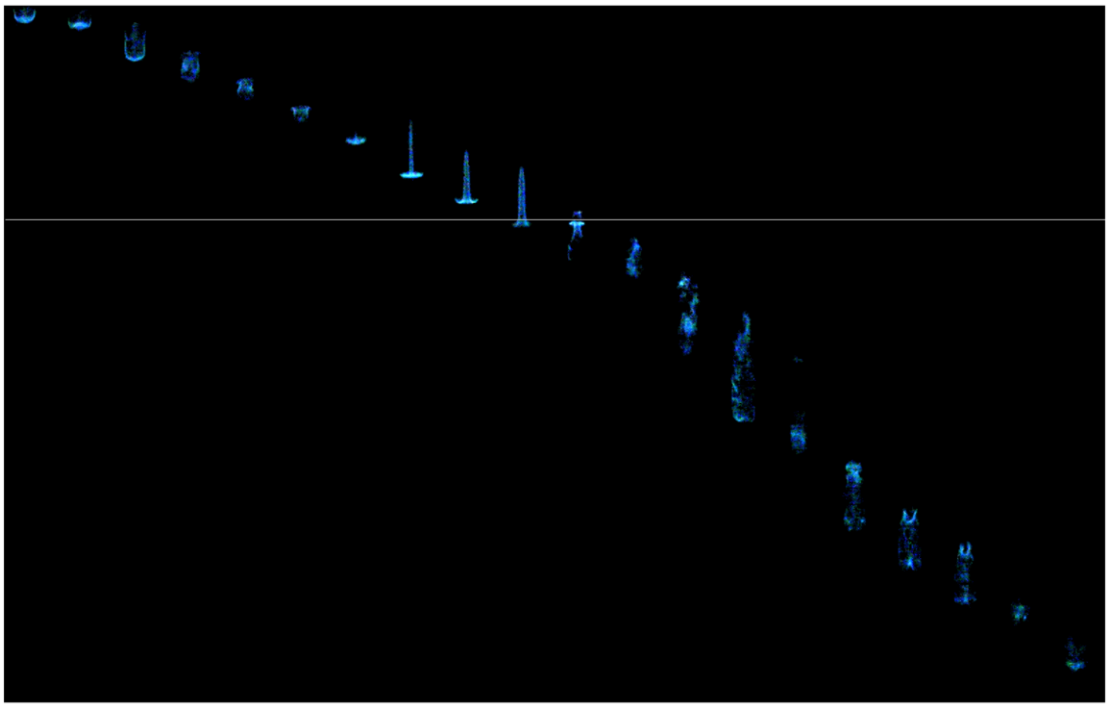

Figure 6-12 Image sequence of 1.5 methane/air without hydrogen.

Figure 6-12 shows the image sequence of methane/air at 1.5 equivalence ratio without hydrogen, as an example of the flame shape. The image is in accordance with flame propagation time, which means that the same intervals were used and the images were enhanced 100 times for presentation. The rest of the area was cropped to save space. The flame was in a tulip shape from the very beginning of the flame propagation, until the oscillation started at a third of the tube distance as marked white line on the figure. The tulip shape was not captured after the oscillation.

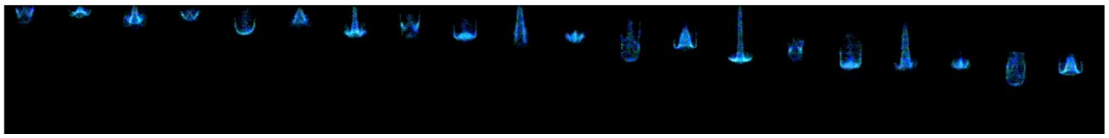

Figure 6-13 Image sequence of 1.5 methane/air without hydrogen (early stage).

Figure 6-13 shows the captured tulip-shaped flame at early stages propagation (around

first 1/5 of the tube length) at equivalence ratio 1.5, without the addition of hydrogen. This image sequence was taken 0.005 intervals after the first one, from the left to right. Multiple tulip flame were captured in this early flame propagation.

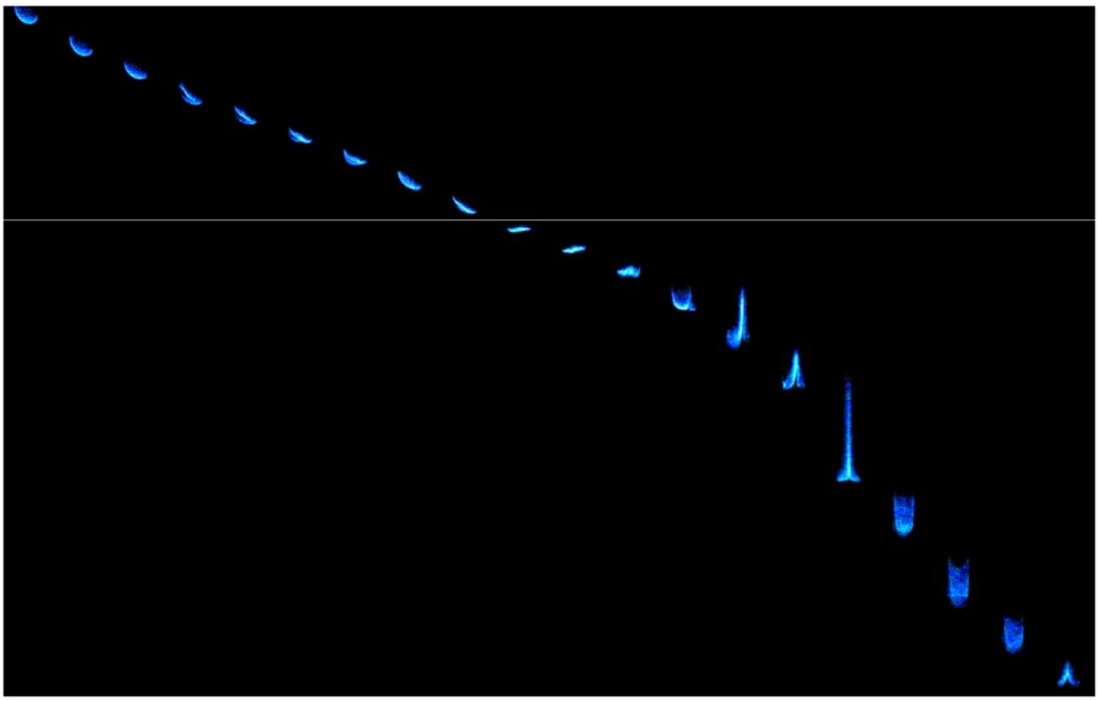

Figure 6-14 Image sequence of 1.5 methane/air, with 40% hydrogen additions.

In order to compare the hydrogen effect in these conditions, an image sequence of equivalence ratio 1.5 methane/air with 40% hydrogen additions was taken, as shown in Figure 6-14. The flame was captured as curved at the beginning for all repeated cases. The flame shape then changed to flat, at around a third of the tube's length as marked white line on the graph. Oscillation then starts, causing the flame to speed up; the tulip-flame shape is captured until the end. The tulip shape formed few times during the flame oscillation.

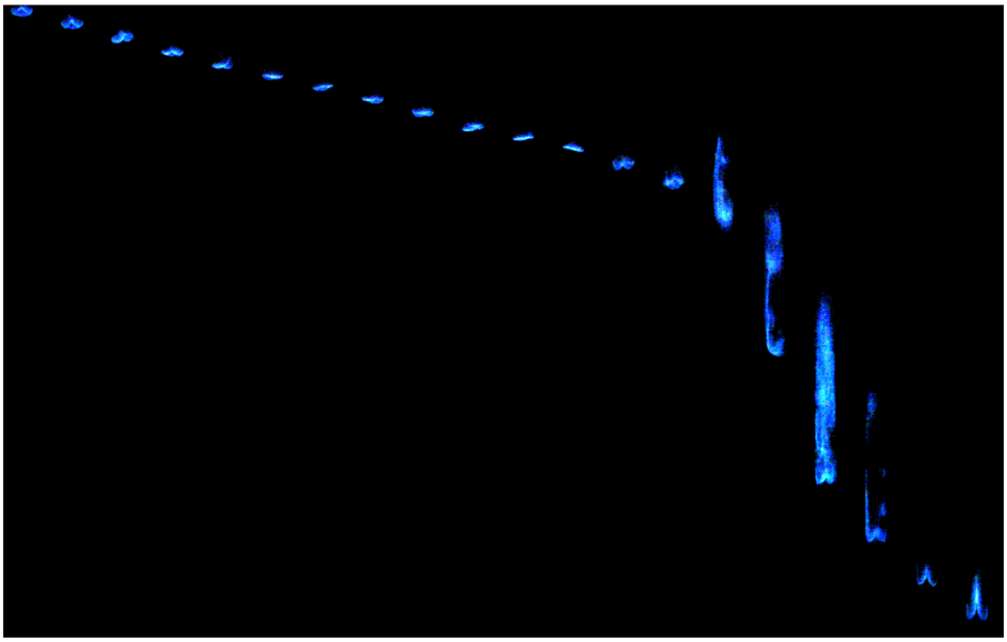

Figure 6-15 Image sequence of 1.3 methane/air without hydrogen.

Equivalence ratio 1.3 shows the peak value of the gradient stage; this run is used as an example. Figure 6-15 shows the twenty-image sequence of equivalence ratio 1.3 methane/air, without hydrogen addition. At the very beginning of flame propagation, the flame shape is curved but it quickly changes to flat. The oscillation happens at a third of the tube length; the flame speed immediately increases and the flame becomes unsteady. The tulip-flame shapes were captured a few times before and after the oscillation. All equivalence ratios 1.1 to 1.4, without hydrogen addition, demonstrate similar behaviours (steady to oscillation). A graph illustrating this can be found in the appendix.

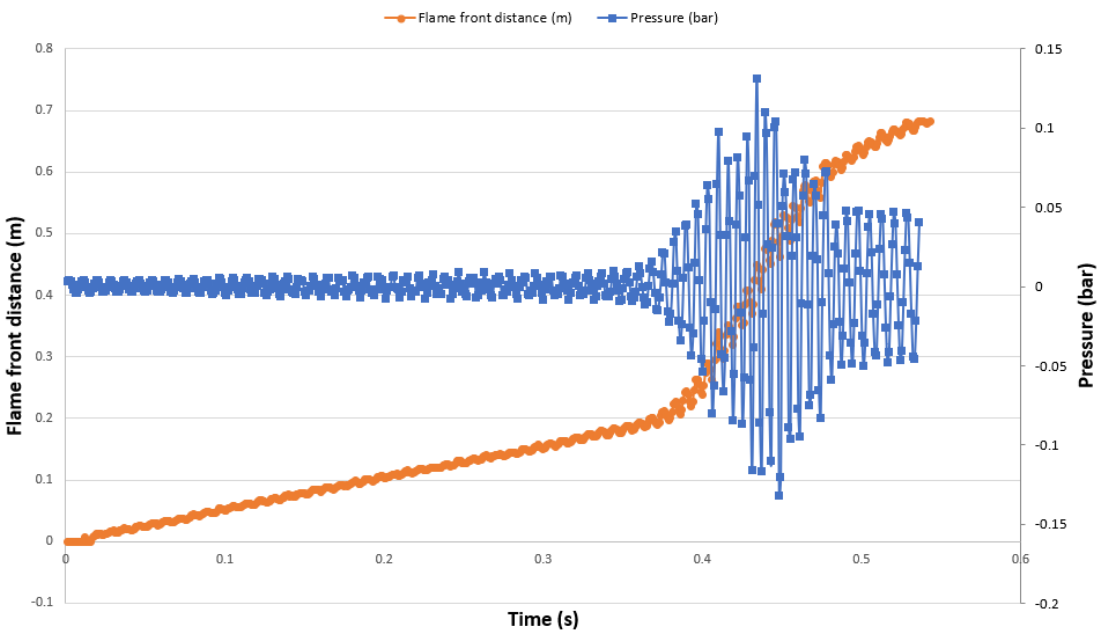

Figure 6-16. Flame front position and pressure at equivalence ratio 1.3, without hydrogen addition.

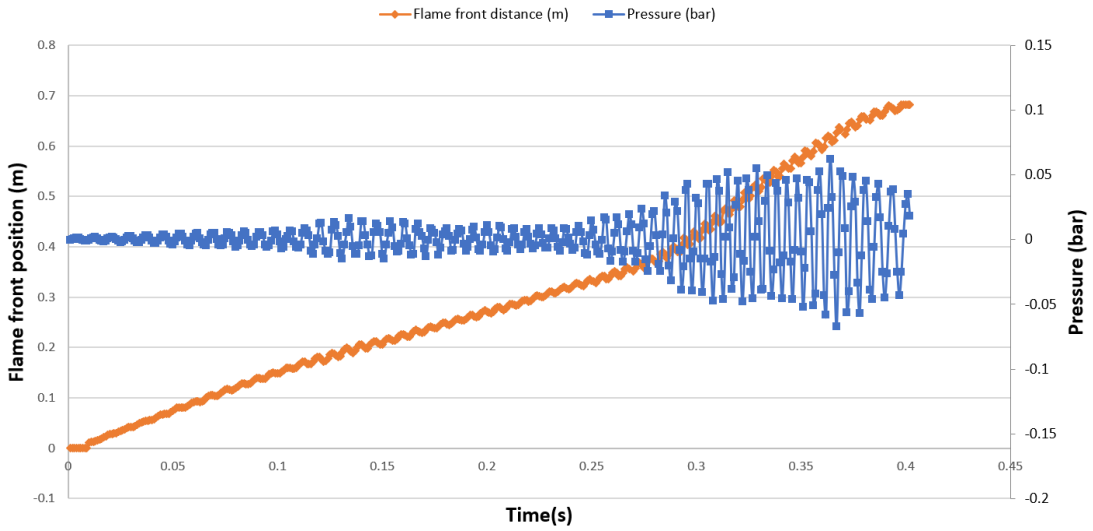

Figure 6-17. Flame front position and pressure at equivalence ratio 1.3, with 40% hydrogen addition.

To hypothesise why the flame propagation speed changes dramatically, Figures 6-16 and 6-17 are plotted to present two sample cases. These demonstrate how pressure affects the flame front distance between 0% hydrogen addition and 40% hydrogen addition, at equivalence ratio 1.3. As shown in Figure 6.15, the flame front position

moved slowly but there was no change in pressure; it remained near its pre-ignition value. A noticeable pressure fluctuation starts at around a third of the tube's length. The peak value of pressure is 0.13 bar. The flame front position travels almost linearly before the oscillation starts, and it becomes a high gradient during pressure fluctuations. After the peak oscillation, the pressure value decreases to around 0.05 bar and a tulip-shaped flame is captured at the end of the tube, as shown in Figure 6-16. Compared to the 40% hydrogen addition under the same conditions, as shown in Figure 6-17 the pressure data show that a small fluctuation happened in a similar position in the non-hydrogen run at a third of the tube length. It did not develop into a large oscillation. Rather, the pressure decreased and developed again after a time of steady propagation. The main difference between those two graphs: the pressure developed into a large oscillation while flame front distance grown to a bigger gradient for non-hydrogen addition case, however its relatively stable for 40% addition case. The pressure remains at around 0.05 bar, in the last third of the tube length. The peak pressure value is 0.06 bar, which is much smaller than the non-hydrogen examples. Figures 6-16 and 6-17 both show a correlation between the pressure and flame front position which is large pressure oscillation leads flame travelled faster, regardless of hydrogen addition.

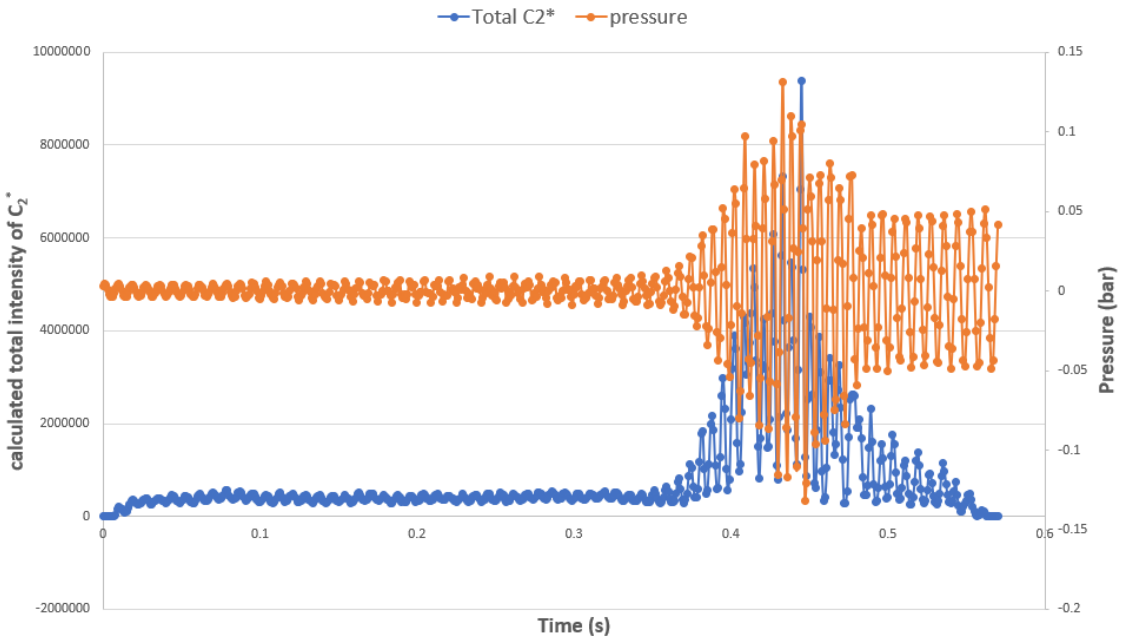

Figure 6-18. Calculated total intensity of C_2^* and the pressure signal at the end of the tube of equivalence ratio 1.3, without hydrogen addition.

Figure 6-18 shows equivalence ratio 1.3 without hydrogen addition case, the figure shows that the calculated total intensity of C_2^* and the pressure signal at the end of the tube. The propagation of the flame was categorised as two stages: the first stage is steady flame propagation without a large pressure fluctuation. The second stage is pressure fluctuation. During the first stage, the intensity of C_2^* remains steady and there are no changes in the pressure, which remains at its pre-ignition value. The flame propagates flat to the direction of travel. At the second stage which is pressure fluctuation stage, oscillations are observed in both the pressure and C_2^*, and the C_2^* and pressure signals achieve their maximum amplitudes. The average speed at this stage is much higher than in Stage one. The flame shape cannot maintain itself at the maximum

amplitudes. A tulip-shaped flame was captured at the end of flame propagation, and the pressure value remained steady at around 0.05 bar. The figure shows that the calculated total intensity of C_2^* and the pressure signal are in-phase at the maximum amplitude area.

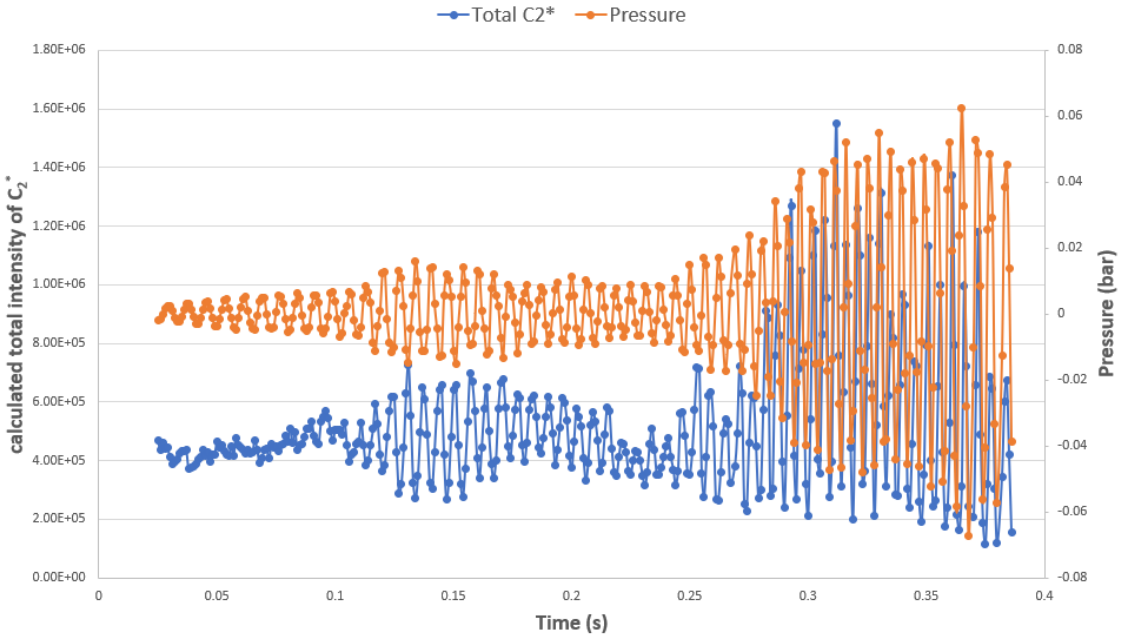

Figure 6-19. Calculated total intensity of C_2^* and the pressure signal at the end of the tube of equivalence ratio 1.3, with 40% hydrogen addition.

Figure 6-19 compares Figure 6-18 (equivalence ratio 1.3, no hydrogen) with the sample at 40% hydrogen addition. During the first stage, the intensity of C_2^* increased slightly and decreased again before the big oscillation; the pressure data shows a similar trend. However, at around the time of 0.15 s—which shows the maximum amplitude in the first stage—the calculated total intensity of C_2^* and the pressure signal are opposite; they are out of phase. The intensity of C_2^* decreases before its largest oscillation, but the pressure signal remains relatively steady in the same range. The pressure signal

becomes stronger at the end of propagation, with the peak value at about 0.06 bar without weakness. The intensity of C_2^* and pressure signal is out of phase, at the end of flame propagation.

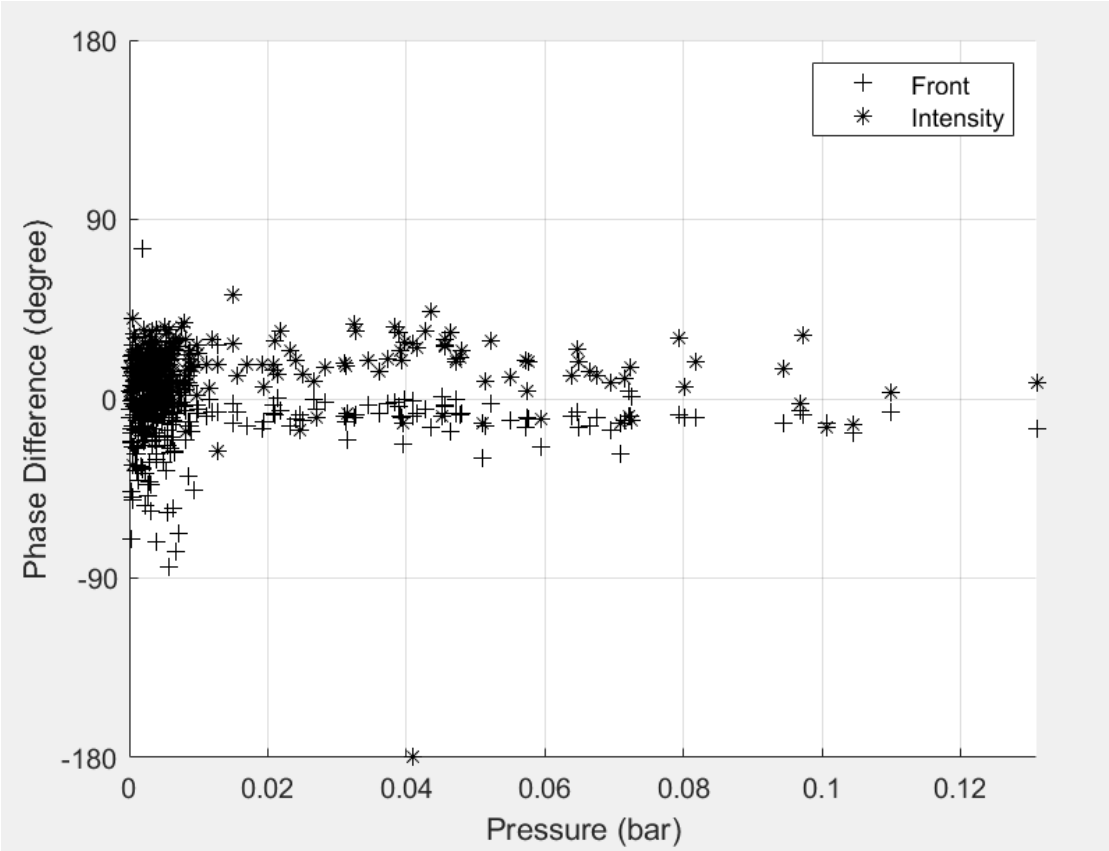

Figure 6-20 Flame-pressure phase difference: flame front distance (+) and flame C_2^* intensity at equivalence ratio 1.3, without hydrogen addition.

Figure 6-20 shows the phase difference against pressure amplitude. A Hilbert transform applied here as same as Chapter five. The pressure phase was used as the reference, producing pressure-front and pressure-C_2^* intensity. It can be seen, all flame front position data falls within 90 degree and most of C_2^* intensity data falls within 90 degree. Which means both flame front position and flame C_2^* intensity was coupling with the pressure.

6.4 Conclusions

Using an open-ended 1200 mm long vertical tube with a 20 mm internal diameter, a study was conducted to determine how different hydrogen concentrations affect flame propagation speed, C_2^* chemiluminescence and pressure oscillations. A quartz tube was used to provide optical access for high-speed colour imaging and a pressure transducer collected the pressure signal at the end of the tube. The main conclusions of the study are:

1. Flame propagation in a vertical tube can be divided into two stages, based on the average flame propagation speed: initial gradient stage and oscillation gradient stage. The average flame propagation speed is faster with higher hydrogen concentrations at the same equivalence ratios in fuel-rich conditions.

2. The ratio of oscillation gradient stage to initial gradient stage decreases linearly, as the hydrogen concentration increases. The highest ratio is during the pure methane/air trial, the pure methane flame propagation in a vertical tube can withstand sudden changes in speed which means the percentage change of average flame propagation speed between second oscillation gradient stage and initial gradient stage is the largest. This may be a useful parameter to determine how hydrogen affects the hydrocarbon fuels propagated in pipelines and a potential point to study in DDT.

3. The C_2^* emissions measured have similar pressure fluctuations as the flame traverses down the tube without hydrogen addition, in the equivalence ratio 1.3 trial. The results show the coupling interaction between flame chemiluminescence and pressure. A Hilbert transform was applied and the result as shown in figure 6-20 also approved the coupling between the flame C_2^* intensity and the pressure. The two signals are in-phase at the maximum oscillation. However, for the 40% hydrogen addition in the same conditions, the C_2^* emissions measured have opposite fluctuations which out of phase in the first stage and end of the tube, with the measured pressure signal at both oscillation ranges. It is difficult to conclude what effect the hydrogen had on C_2^* emissions, but the data shows that adding hydrogen at equivalence ratio 1.3 caused most of the C_2^* emissions and pressure fluctuation to be out of phase, leading to a decreased peak value of pressure.

4. Tulip-shape flames were captured multiple times, under different conditions and locations. It's worth to develop the relationship between tulip phenomenon, C_2^* emissions and pressure fluctuation in further experiment.

7 CHAPTER SEVEN: Premixed Methane / Air / Hydrogen Flame Propagation in a Square Tube Using Two Different Cameras

7.1 Introduction

Experimental research is vital for revealing basic phenomena, theories, and numerical models of the flame propagation process, and is key to the promotion and development of combustion and explosion science. Regarding the propagation of premixed flames in pipelines, previous experimental studies have mainly focused on the acceleration of explosive flames and deflagration-to-detonation processes, in either smooth or obstructed pipelines. The flammable gases that were used in those studies were also mainly single gases, including methane and propane or other hydrocarbon fuels. In recent years, experimental studies on the detonation of hydrogen-air mixtures in pipelines have been carried out successively, with the purpose of providing basic experiments for safety evaluation and the verification of numerical calculation models' data.

Although many experimental, theoretical, and numerical studies have been carried out on the propagation of premixed flames in pipes, certain flame characteristics—such as

flame instability and flame deformation—have not been fully studied. The literature is especially lacking regarding reliable flame research on explosion prediction models and experimental verification. It is difficult to ensure that each run of an experiment is exactly the same, because it is impossible to control all influence variables. Therefore, it is especially meaningful to obtain more information using different image-shooting methods simultaneously also not reduce the experiment repeatability. In this study, two camera capture systems were used: one high-speed colour camera and one high-speed black-and-white (B&W) camera were simonised to study the flame's shape, position changes and instability. Pressure sensor technology was used to study the characteristics of pressure increases and the relationship between the flame dynamics during flame propagation. Finally, flame chemiluminescence and the schlieren imaging technique were applied separately to the two cameras.

7.2 Experiment Setup

To use the schlieren method to capture flame movement, a 20-mm diameter square tube with 1200 mm long—made with a 2-mm thick acrylic sheet—was applied, as shown in Figure 7-1. The acrylic sheet used here allowed for over 95% light access. The metal cover maintained the tube's stability on the non-light access sides, while the gap between the tube's side was glued from outside to avoid affecting the centre flame.

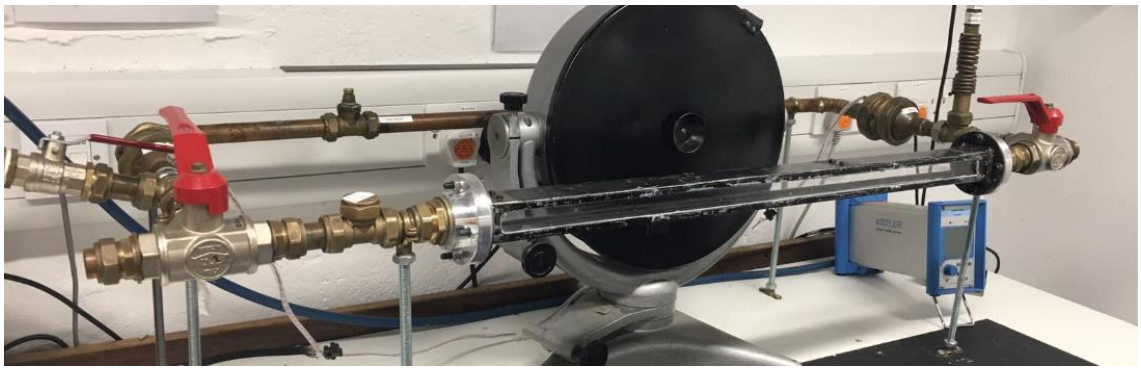

Figure 7-1 Square Tube

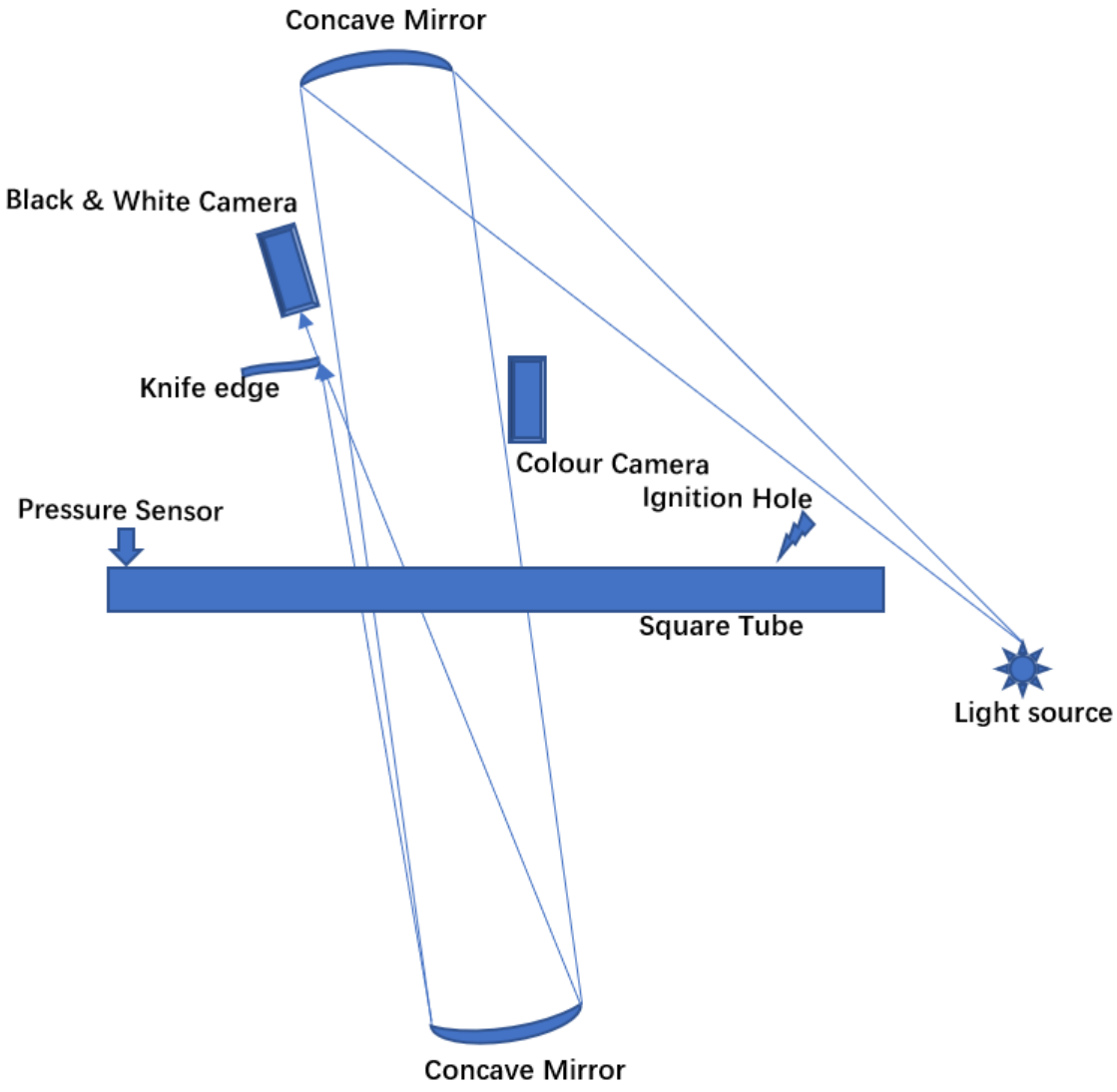

Figure 7-2. Schematic of the Experiment's Set-up

Figure 7-2 shows the schematic of the experiment's set-up, which mainly includes one

schlieren imaging system, one chemiluminescence imaging system, one pressure measurement system and one flame mixing system. The flame mixing system was similar to what is described in Chapters five and six, but it was configured to fit the z-type schlieren. The flame propagation tube was 1200 mm long and it was placed horizontally, as shown in Figure 7-1. The tube was both ends opened during the experiment. The mixing system is not included in Figure 7-2, but the real set-up images are shown in the appendix. The pressure measurements were collected using a Kistler Type 7261 piezo-electric pressure transducer, which was mounted at the end of the tube (Figure 7-2, left side) that was furthest from the ignition point (Figure 7-2, right side). The ambient temperature of the lab was approximately 293 K. Following each experiment, the tube was evacuated using a vacuum pump. The required volume of fuel was injected into the apparatus using a syringe, and air was introduced into the rig to bring it to atmospheric pressure. The high-speed camera that was used for the chemiluminescence imaging system was a Photron SA-4 high-speed colour camera with a Nikon fix 35 mm; an f-1.2 zoom lens; and a framing rate of 1,000 fps. Additionally, a 1,000-μs shutter speed was used to record the flame propagation progress. The high-speed camera that was used for the schlieren system was a Phantom V210 mono high-speed camera, with a Nikon AF NIKKOR 24–85 mm; an f-2.8-4D IF lens; a framing rate of 10,000 fps; and a 2-μs shutter speed. A typical z-type schlieren system was used. The light from the light source was passed through a small hole to form a point. The reflector then reflected the light onto the concave mirror on the right,

to create a parallel light between the two concave mirrors. The view that was reflected by the second concave mirror was cut by a knife edge and then passed into the camera. The chosen equivalence ratio was from 0.9 to 1.1, with 0.1 intervals of methane mixing with air; in addition, 0%–100% hydrogen was added in this case. The two cameras and the pressure sensor were synchronised.

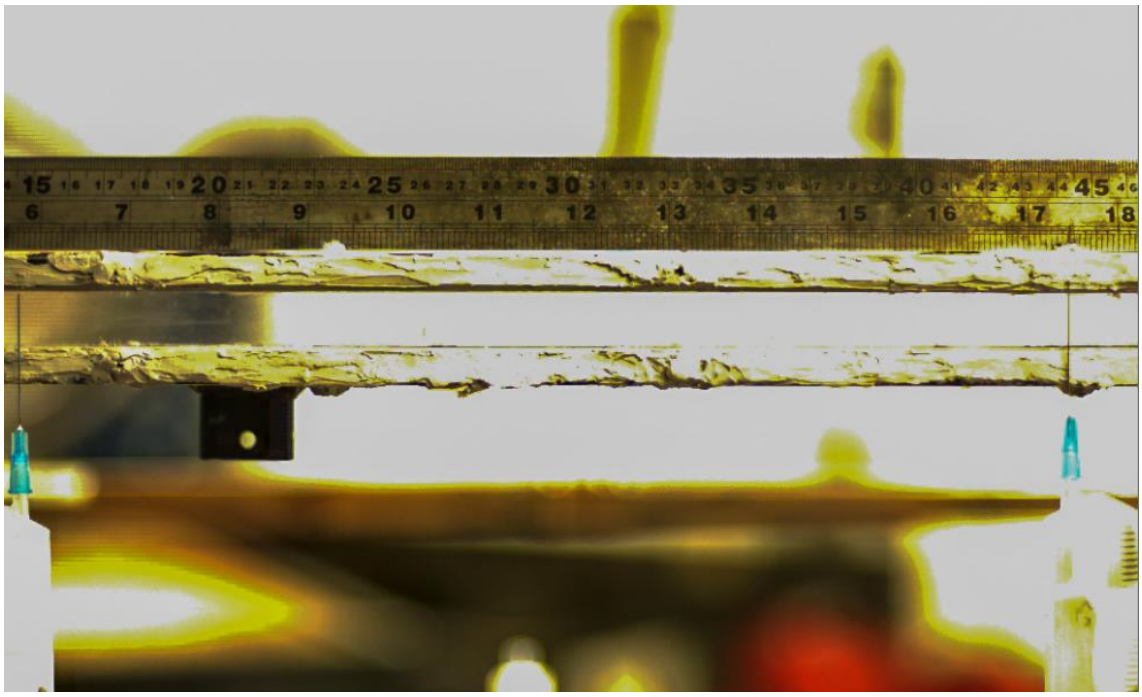

Figure 7-3. Reference image captured by colour camera

Figure 7-3 shows the reference image that was taken by colour camera after the set-up was completed. With two different optical measurement methods applied in one case, it was difficult to ensure that the cameras captured the same range. Hence, a reference image that was taken by the colour camera shows the range of colour that was captured, while two vertical syringe needles capture the range of the B&W camera. The small angle (less than 10 degrees) may have affected the results between the first concave mirror and the colour camera to the captured tube; therefore, it was ignored for technical

reasons.

7.3 Result and Analysis

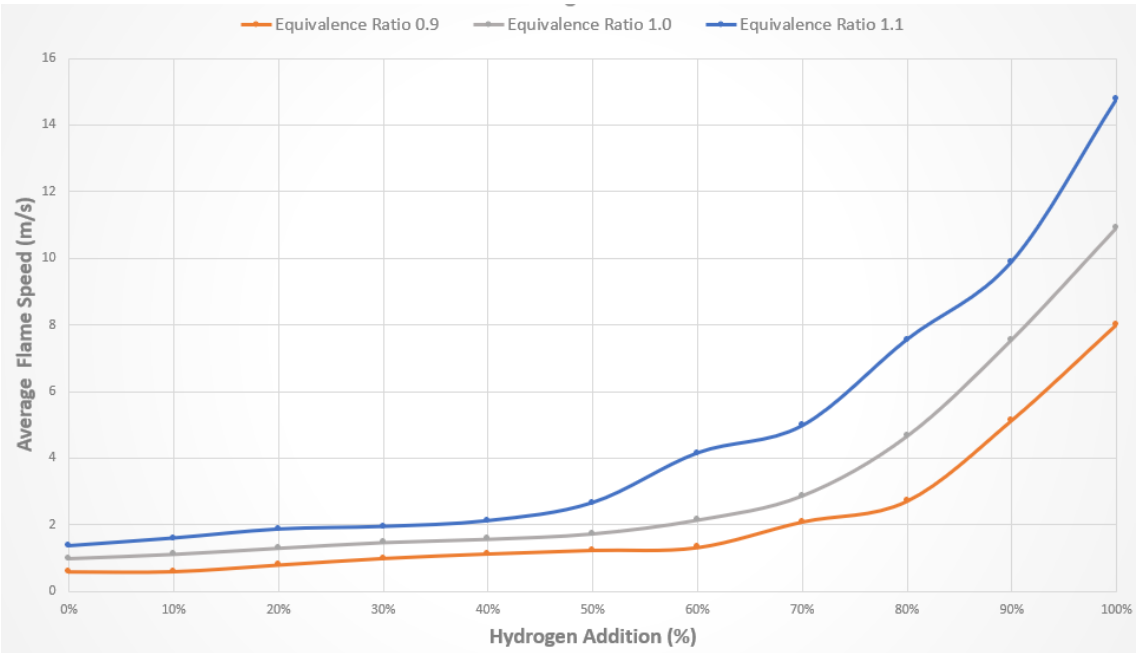

Figure 7-4. The average flame propagation speed of the methane/air/hydrogen mixture against the equivalence ratio at all conditions; each point is averaged by three runs.

Figure 7-4 shows a graph of the flame propagation speed against the equivalence ratio at varying hydrogen additions. The details of equivalence ratio calculation are shown in appendix figure 10-1 and 10-2. The average flame speed increased as the equivalence ratio increased with the same hydrogen addition. In a certain equivalence ratio, the average flame speed increased as the hydrogen addition increased, which means hydrogen concentration affects the flame propagation speed.

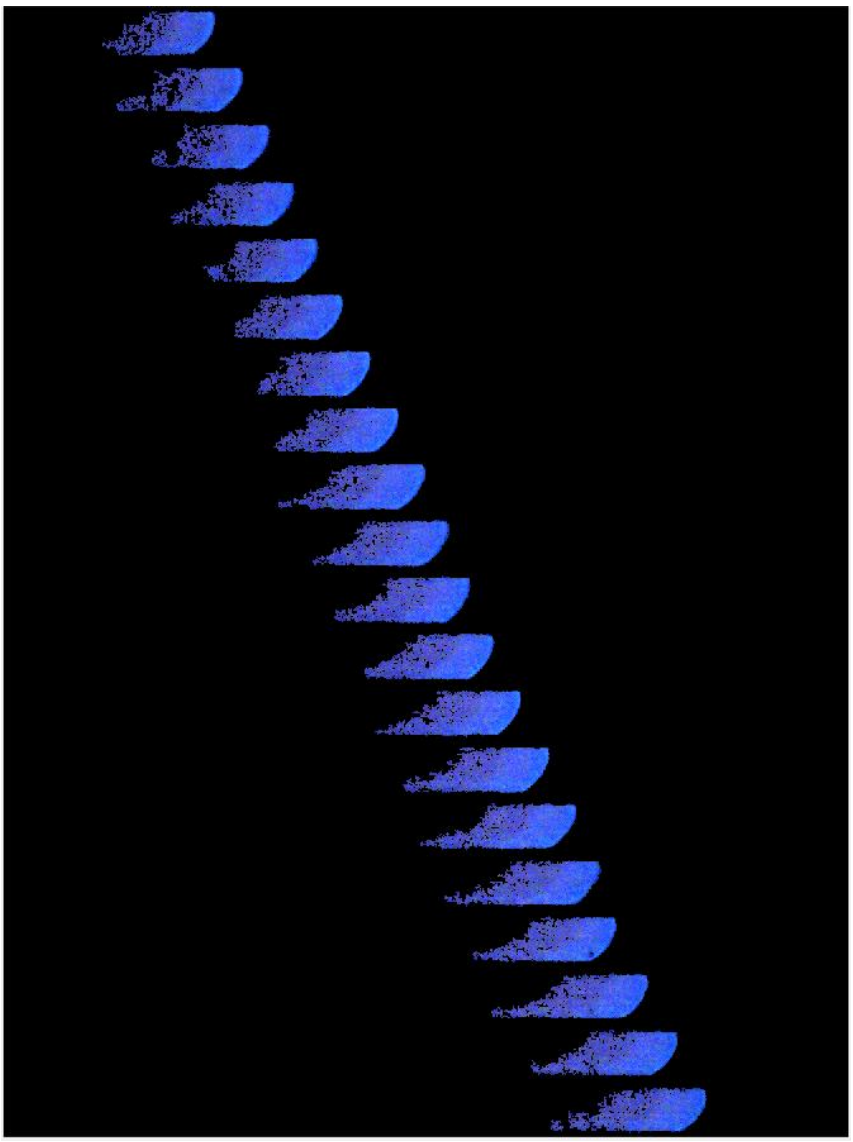

Figure 7-5. An equivalence ratio of 1.1 for the methane/air mixture and a 30% hydrogen addition.

Figure 7-5 shows an equivalence ratio of 1.1 for the methane/air mixture and a 30% hydrogen addition with a 0.005-second interval. The images were placed vertically and enhanced 20 times for better visualisation. In the image displayed above, the convex or flame finger shape was due to the non-slip condition of the wall acting on the burnt gases, as well as to heat transfer from the reaction zone to the wall (Yu 1986).

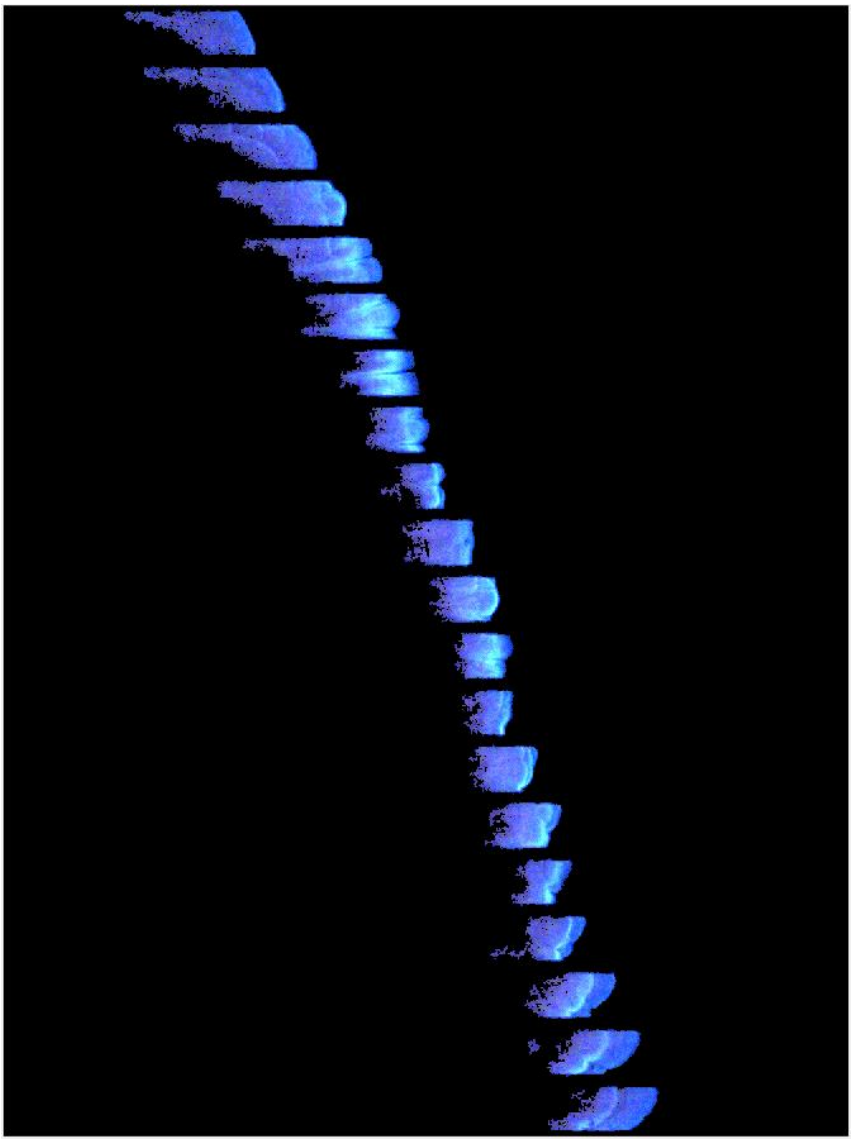

Figure 7-6. An equivalence ratio of 1.1 for the methane/air mixture and a 40% hydrogen addition.

The flame began oscillating during its propagation in the tube with a higher hydrogen concentration, as shown in Figure 7-6. The flame looks unstable, compared to Figure 7-5, and multiple flame shapes can be seen. At the early stage of the flame's propagation, the flame's front looks similar to that of Figure 7-5—convex to the unburnt gases' direction. However, the bottom layer of the flame is facing forward. The cellular flame shape that was formed inside the flame, followed by a tulip flame, can be observed

multiple times at the central length of the tube. The flame constantly changed shape and finally returned to a stable propagation, which was similar to what occurred at the early stage.

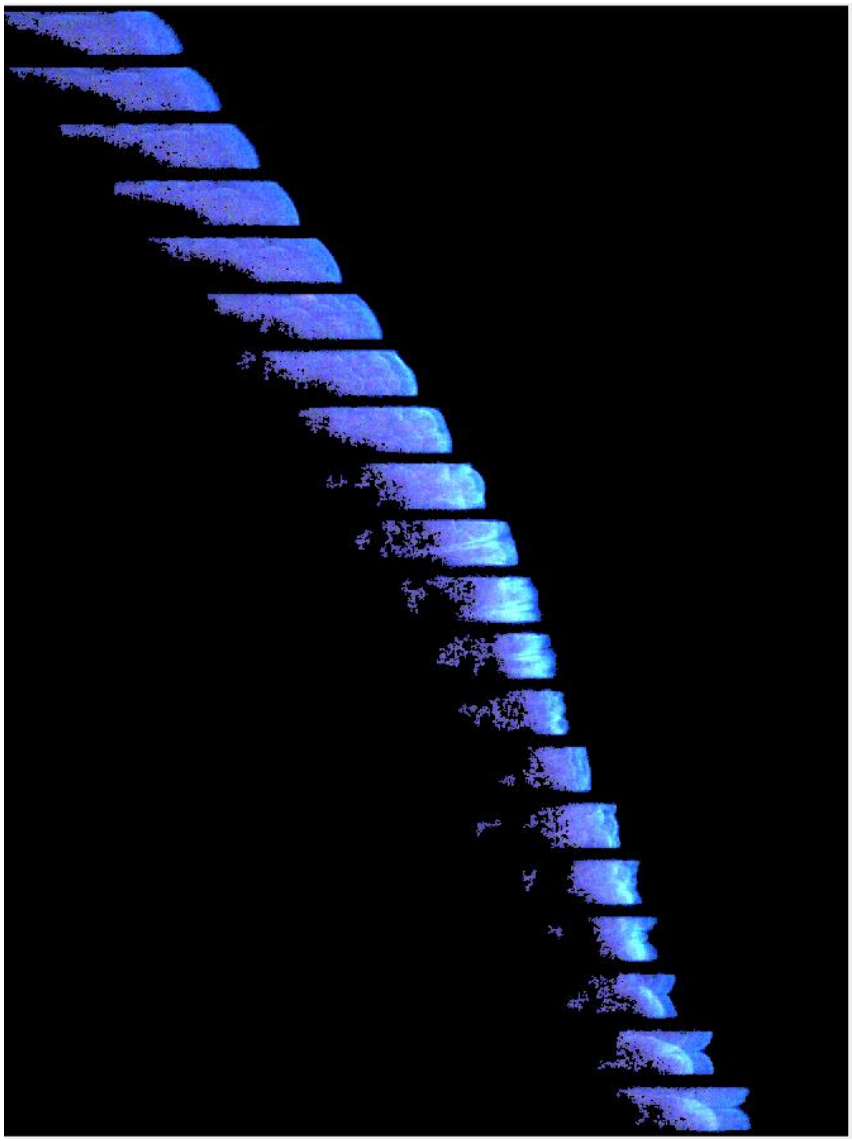

Figure 7-7. An equivalence ratio of 1.1 for the methane/air mixture and a 50% hydrogen addition.

Figure 7-7 shows a higher hydrogen concentration than that of Figure 7-6. The behaviours look similar, but the early stage of the stable flame propagation seems to extend around the central length of the tube, compared to 40% hydrogen addition as

shown in figure 7-6, the curved flame propagated longer before oscillation happened. Again, the tulip flame shape can be observed, but it occurs a little after the central length of the tube. Following the oscillation period, the cellular flame formed in the flame's front and brought a few flame shape propagations together towards the unburnt gases in the tube. For example, two layers of flame front as shown in bottom three in figure 7-6.

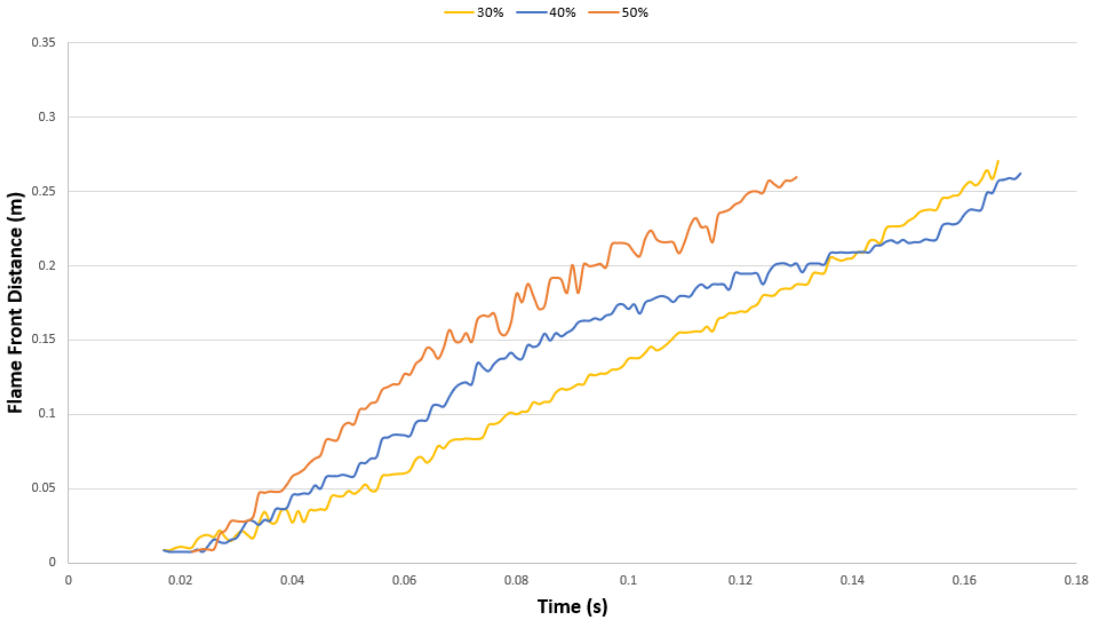

Figure 7-8. The flame's front position (m) from the captured beginning to captured end at an equivalence ratio of 1.1 for the methane/air/hydrogen mixture.

Figure 7-8 plots the flame's front position (m) from the captured beginning to the end of the camera against time with increasing hydrogen concentrations, from 30%–50%, at an equivalence ratio of 1.1 for the methane/air/hydrogen mixture. The details of mixture are shown in appendix. The methane and hydrogen concentration mixture of lower than 30%, at an equivalence ratio of 1.1; the hydrogen concentration mixture of

lower than 40%, at an equivalence ratio of 1.0; and the hydrogen concentration mixture of lower than 50%, at an equivalence ratio of 0.9, were observed with flame propagation. This was relatively steady in the entire tube, with a slight increase in velocity as the flames propagated. Some of the flames were captured by the small oscillation inside the flame, such as the first few images in Figure 7-6, it can observe some small layers inside of the flame, but there were no changes in the flame's shape. For the 30% hydrogen concentration, the flame's front position was relatively linear to the end, compared with the other two. As the hydrogen concentration increased to 40% and 50%, there was a noticeable position difference around the central length of the tube. As shown in figure 7-8, using a 0.15-m line in y-axis as a half-length of the tube for reference, the full captured range of tube about 0.3 meter, the greatest oscillation of the 50% hydrogen concentration happened after a half-length of the tube, and the gradient of the 40% hydrogen concentration reduced after a half-length of the tube.

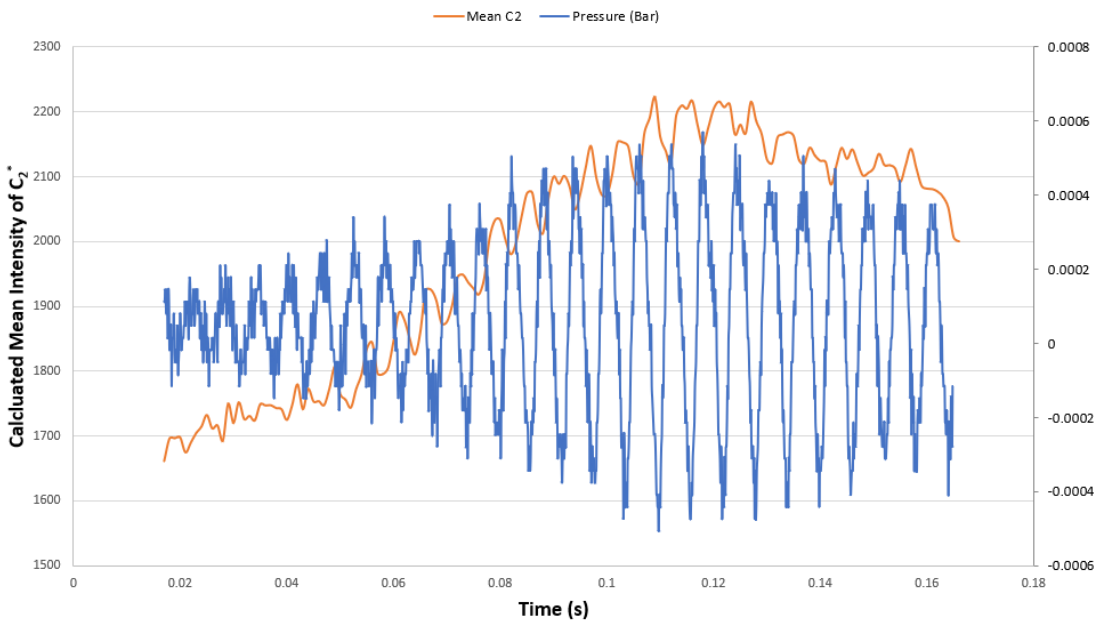

Figure 7-9. The calculated mean intensity of C_2^* and the pressure signal at the end of the tube at an equivalence ratio of 1.1, with a 30% hydrogen addition.

Figures 7-9, 7-10 and 7-11 show the calculated mean intensity of C_2^* and the pressure signal—which was placed at the end of the tube at an equivalence ratio of 1.1 with 30%, 40% and 50% hydrogen additions, respectively. Figure 7-9 shows the fluctuation of pressure constantly increased with each cycle, until the maximum amplitude of the pressure oscillation reached ~0.0005. The oscillation of the mean intensity of C_2^* can be observed, and the value increased—although there were no flame shape changes—in Figure 7-5. Both the mean intensity of C_2^* and the pressure data show it being out of phase for most of the oscillation cycles.

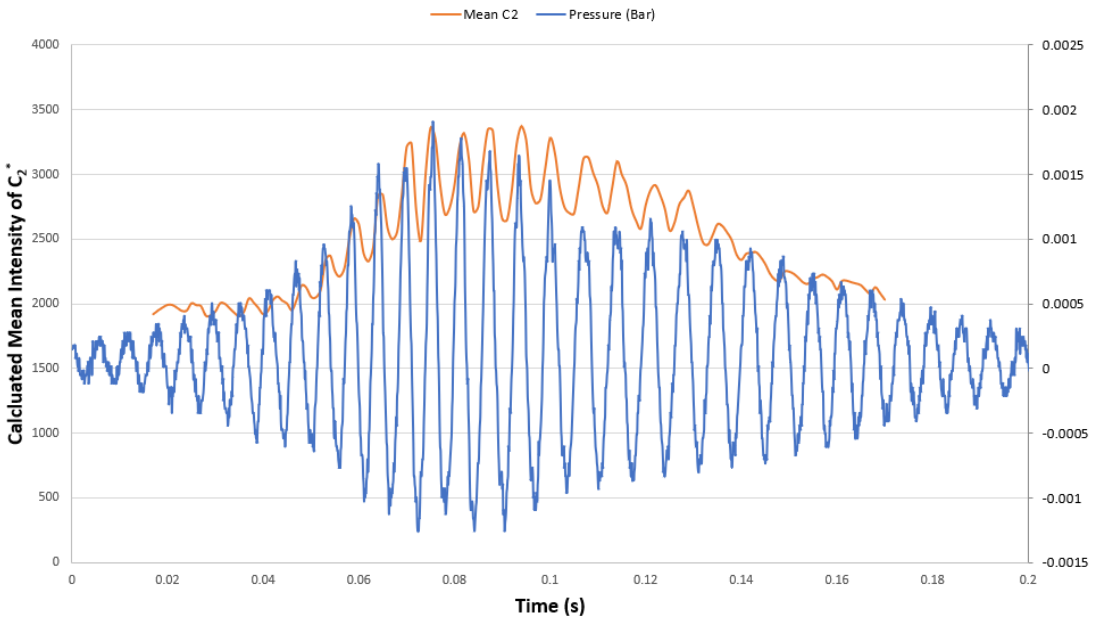

Figure 7-10. The calculated mean intensity of C_2^* and the pressure signal at the end of the tube with an equivalence ratio of 1.1, with a 40% hydrogen addition.

A 40% hydrogen concentration is shown in Figure 7-10. The pressure data were used from the ignition to the end. The maximum amplitude of pressure oscillation increased in nearly every cycle, until it reached a peak value of ~0.0019 and then decreased towards the end. The C_2^* and pressure signals increased to their maximum amplitudes during the same cycle of fluctuation. The value of C_2^* intensity then decreased to the same level as that of the early stage of propagation, towards the end. The pressure and C_2^* signals were in phase during their maximum oscillation and out of phase during the early stage of flame propagation.

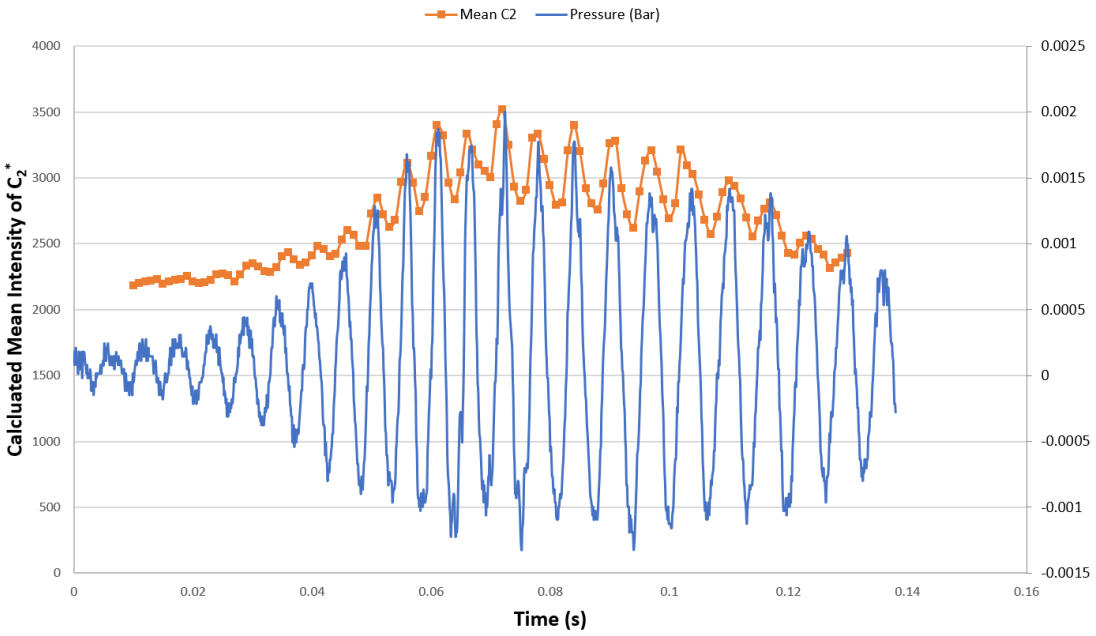

Figure 7-11. The calculated mean intensity of C_2^* and the pressure signal at the end of the tube with an equivalence ratio of 1.1, with a 50% hydrogen addition.

A 50% hydrogen concentration is shown in Figure 7-11. The C_2^* shows a similar trend to that of Figure 7-10. The maximum amplitude of pressure oscillation reached the 0.002 bar. The pressure and C_2^* signals were also in phase at their maximum oscillation range.

Figures 7-12 to 7-15 show that the schlieren images were captured at an equivalence ratio of 1.1, for the methane/air mixture with a 40% hydrogen addition. The images range from a normal flame to oscillation flame propagation. The number is shown at the left of each frame for easy identification. Each frame is timed with a 0.01-second interval.

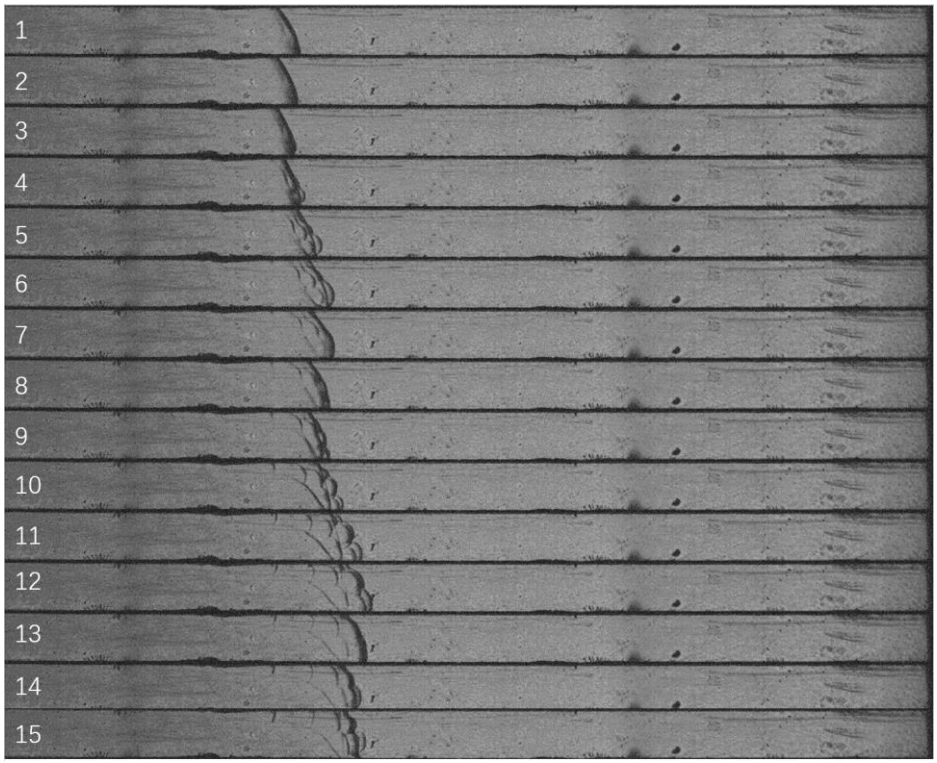

Figure 7-12. Schlieren images of an equivalence ratio of 1.1 for the methane/air mixture with a 40% hydrogen addition. (a)

Figure 7-12 shows the first column of images from image numbers 1 to 3 (only the number marked at the left of each image will be used in the following analysis). The flame's front shape like a finger, it was steady and pointed forward towards the unburnt gas. However, the flame's front layer not moved forward to the un-burned gas direction. Even moved forward to the burned gas direction. From 4 to 7, the cells appeared in the flame's front, which led to a cellularity increase as the flame speed increased. The flame's front position moved back to the burned gas direction again at 8 and 9 and then pushed to 12.

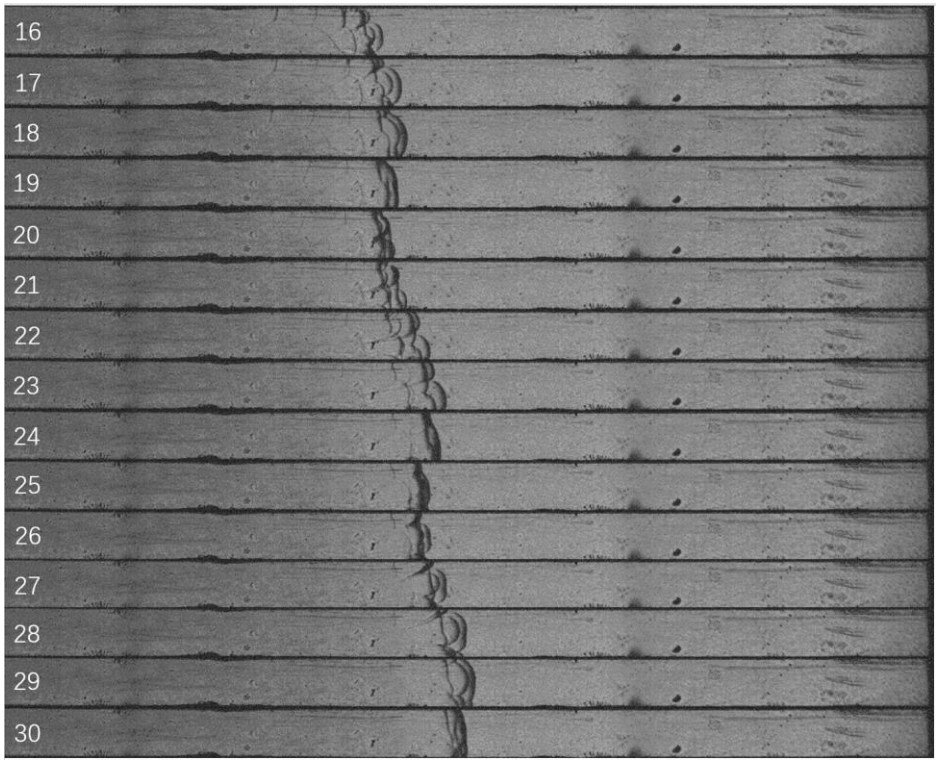

Figure 7-13. Schlieren images of an equivalence ratio of 1.1 for the methane/air mixture with a 40% hydrogen addition. (b)

Figure 7-13 shows the second column of images, which started from the cellular flame's front at 16. For both 16 and 17, the tulip shape was captured on two sides close to the wall of the tube, and it disappeared at 18. The flame pushed back towards the burnt gas's direction until 20, and the tulip shape was formed in the middle of the tube. The reversed tail in the middle of the flame developed, while the flame front position simultaneously propagated forward to the unburnt gas's direction to 23. The flame slowed again at 25, but the tulip shape formed again on two sides close to the wall, from 26 to 29.

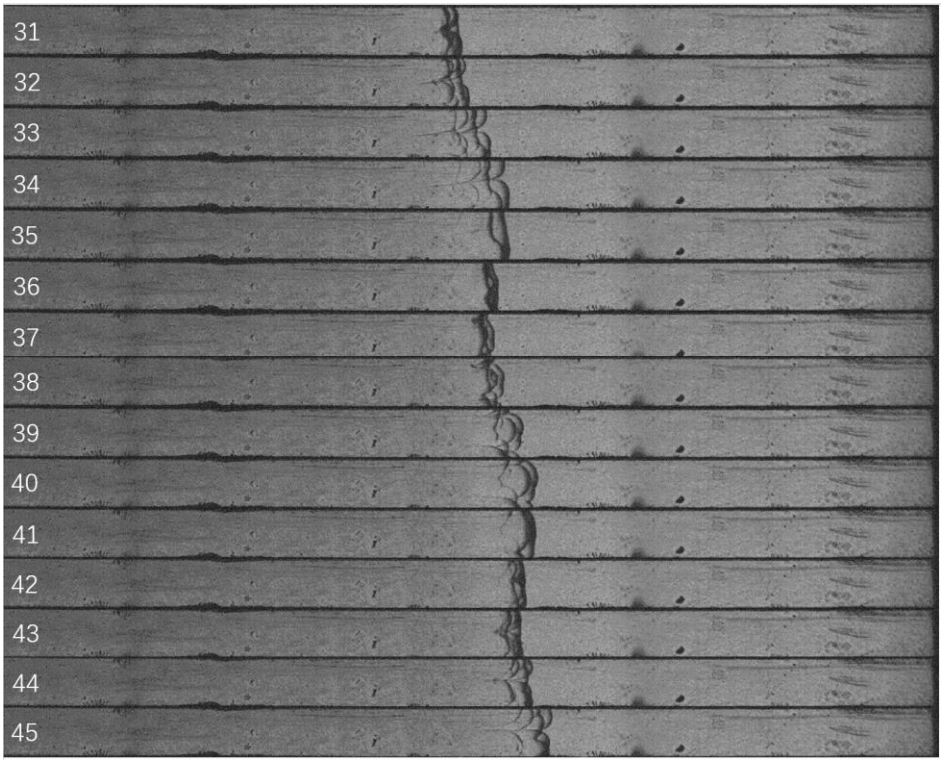

Figure 7-14. Schlieren images of an equivalence ratio of 1.1 for the methane/air mixture with a 40% hydrogen addition. (c)

The third column, as shown in Figure 7-14, reflects where a clear tulip-shaped flame formed in the middle of the tube, which was captured and developed from 31 to 34, with the flame's front position pushed forward towards the direction of the unburnt gas. A similar phenomenon repeated one more time, as seen in the remaining images of this column.

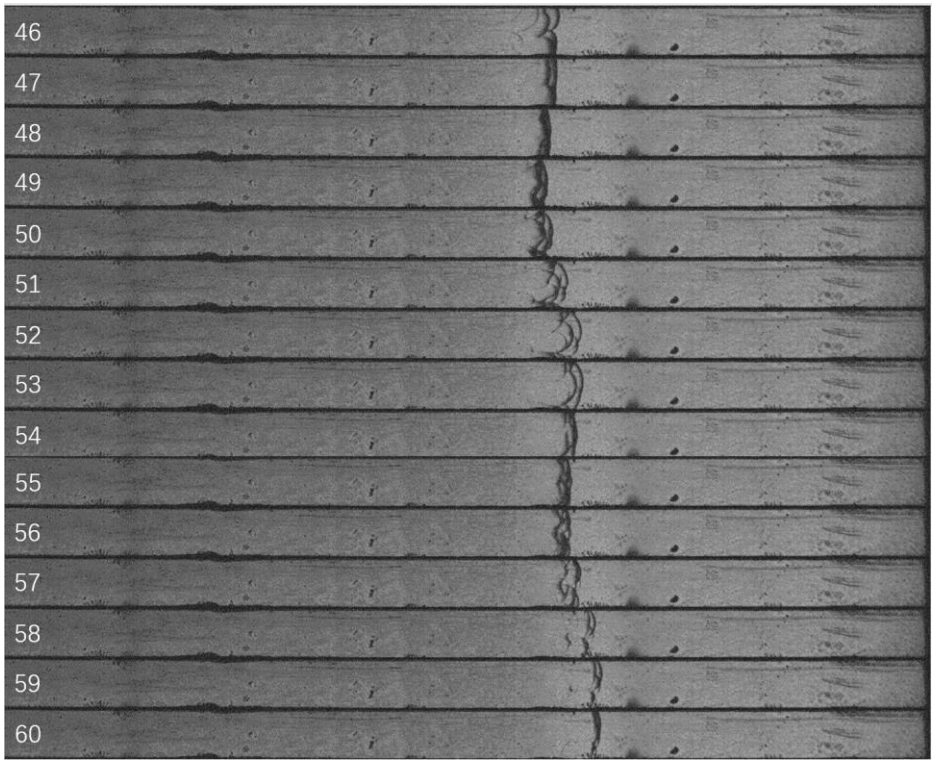

Figure 7-15. Schlieren images of an equivalence ratio of 1.1 for the methane/air mixture with a 40% hydrogen addition. (d)

The last column reflects similar behaviour to that of the previous three columns, but no tulip flame occurred; only cellular cell-shaped flames are shown.

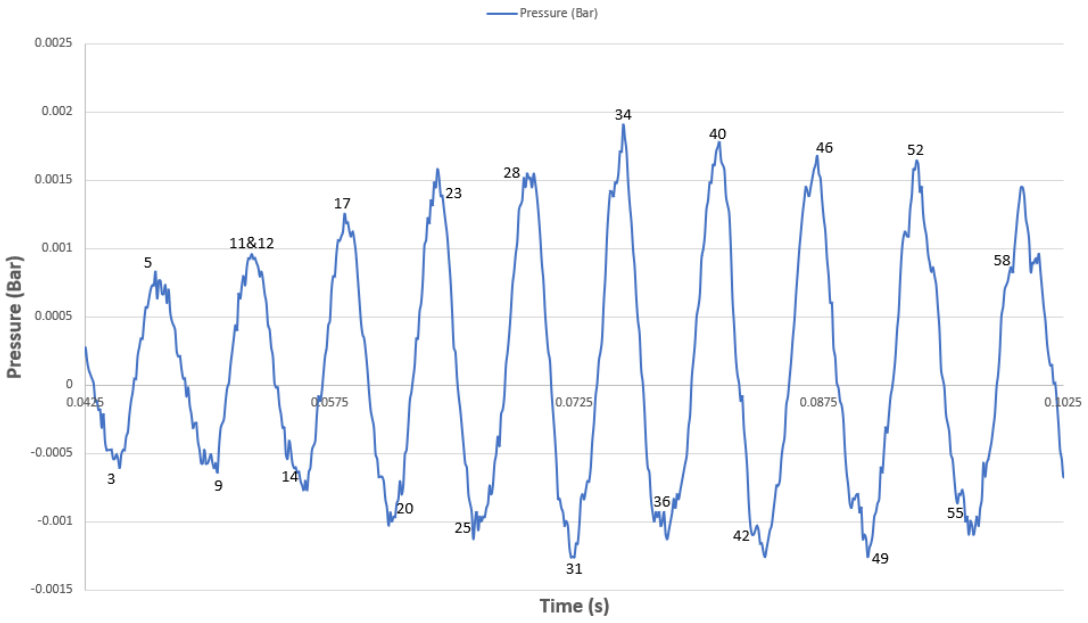

Figure 7-16. Pressure signal at the schlieren image range.

Figure 7-16 shows the pressure signals of the images in Figures 7-12 to 7-15. The number at the x-axis shows time(s) according to the recorded raw data. The number marked on the figure is used as the image's figure number (7-12 to 7-15). The location of the marks on the figure were approximate, because of the high rates of pressure data that were recorded. The figure shows that the pressure went down when the flame pushed back towards the burnt gas's direction, and the pressure went up when the flame pushed forward. As shown in figures 7-12 and 7-15, no tulip flame shapes could be observed while cells appeared.

7.4 Conclusions

This study used two different optical experiment methods at the same time, to obtain more information about methane/air/hydrogen mixture flame propagation in a square tube. In this case, two high-speed camera capture systems were successfully applied. A high-speed colour camera was used for flame-for-flame chemiluminescence analysis, and a high-speed black & white camera was used for a schlieren imaging study. Pressure sensor technology was used to study the characteristics of increasing pressure and the relationship between the flame's dynamics during propagation. The main conclusions of this study include the following:

1. The flame speed increased, as either the equivalence ratio or hydrogen concentration increased. No oscillation of the flame could be observed when the hydrogen concentration was below 50% at an equivalence ratio of 0.9, below 40% at an equivalence ratio of 1.0 and below 30% at an equivalence ratio of 1.1. This indicates that hydrogen has a stronger influence at higher concentrations of the methane–air mixture.
2. The correlation between fluctuations of measured C_2^* emissions and measured pressure was discussed. The results presented a coupling interaction between flame chemiluminescence and pressure, during flame oscillations.
3. The mixing of hydrogen increased the molecular diffusivity of the mixture. The images of schlieren did not show wrinkles, but did show more cellular cells at the

front of the flame (flame shows smooth front not rough), which proved that the flame was affected by thermal diffusion instability. The cellular flame's front led to an increased burning area at the flame's front, which caused an increase in flame speed. The conclusion similar to Bradley, D. et.al (2000) mentioned: wrinkling continually increases the flame speed.

4. The schlieren images and pressure signal results showed periodic propagation characteristics around the middle length of the tube. Each cycle included either a flat or a curved flame front, a cellular shape or cells at the flame's front, two near-boundary flames at the sides of the tulip flames, either a flat or a curved flame at the front again, either a cellular or cells' flame at the front again and, finally, a tulip flame in the middle of the tube. However, the formation of a tulip flame based on this case has six steps, it was different with Clanet and Searby's (1996) experiment and their four steps for forming a tulip flame. Gonzalez, M. (1996) proved that the periodic oscillation behaviour of the premixed flame in the tube is caused by the interaction between the flame and the pressure wave. The periodic acceleration and deceleration of the flame drove the flame shape to look like a cell structure. This flame structure is closely related to Rayleigh-Taylor instability. Clanet, C. & Searby, G. (1996) have also proven that the flame front speed decreased, related to the Rayleigh-Taylor instability.

8 CHAPTER EIGHT: Conclusions and Recommendations for the Future Work

8.1 Conclusions

The dynamics and behaviours of flame propagating, in a premixed methane/air mixture with hydrogen addition, were experimentally investigated in both horizontal and vertical tubes. The measurement method mainly applied a flame chemiluminescence technique, utilising a high-speed colour camera and a pressure sensor placed at the end of the tube. The interesting interaction between the C_2^* emissions and pressure, with hydrogen addition, was found in the horizontal tube. Hydrogen concentration, affecting flame speed at the second stage of flame propagation in a vertical tube, was also discussed. To develop the mechanisms of flame formation, schlieren imaging techniques were applied at flame propagation in a square tube. The contributions of this work are summarised in the following statements.

1. A flame chemiluminescence measurement technique was proposed. The image of the colour-based flame chemiluminescence measurement was based on relationships between the flame chemiluminescence, the camera's sensor spectral sensitivity and the image colour model. The high-speed colour camera tested was a Photron SA-4 model. The CH^* and C_2^* chemiluminescence measurement methods

were proposed, based on the assumption that all hydrocarbon premixed flame chemiluminescence only emits CH^* at 430 nm and C_2^* at 516 nm. Denoising the images, collecting data from the images and other post-processing tasks were accomplished mainly through the use of MATLAB software.

2. Two typical hydrocarbon fuels—C_3H_8 (propane) and CH_4 (methane)—burning on a Bunsen burner, were applied to establish the relationship between the C_2^* chemiluminescence and the premixed flame. The results found that—for both methane and propane—the CH^*/C_2^* ratio had a linear response to the equivalence ratio, when equivalence ratio was > 0.95. This provided the fundamental knowledge that the calculated CH^*/C_2^* chemiluminescence was related to the flame's chemistry.

3. Flame chemiluminescence measurement and pressure measurement methods were applied, in the case study of a premixed methane/air/hydrogen flame oscillation in horizontal open-ended tubes. The measured C_2^* emissions had similar fluctuations with the measured pressure, as the flame traversed down the tube. The results indicated a coupling interaction between the C_2^* flame chemiluminescence and the pressure.

4. The flame chemiluminescence measurement and pressure measurement methods were also applied to a vertical tube. Flame propagation in a vertical tube can be

divided into two stages, based on the average flame propagation speed: the initial gradient stage and the oscillation gradient stage. The flame propagation speed was faster, with higher hydrogen concentrations, at the same equivalence ratios in fuel-rich conditions. The ratio of two oscillation gradient stage (oscillation gradient stage to the initial gradient stage), decreased linearly as the hydrogen concentration increased. The results show a coupling interaction between the flame's chemiluminescence and the pressure. The two signals were in-phase at the maximum oscillation.

5. Two different optical imaging measurements—the flame chemiluminescence measurement and the schlieren imaging measurement—were successfully applied to obtain more information about flame propagation in a square tube. The flame speed increased as the equivalence ratio or hydrogen concentration increased. The oscillation range that was caused by the hydrogen concentration was discussed. The correlation between fluctuations of the measured C_2^* emissions and the measured pressure were also discussed.

6. Following the results of the schlieren images and pressure signals, periodic propagation characteristics were observed around the middle length of the tube. Each cycle included a flat or curved flame front, a cellular or cells flame front, two near-boundary sides of the tulip flame, a flat or curved flame at the front again, a

cellular or cells flame at the front again and a tulip flame in the middle of the tube. The tulip flame may not form or may not be included in the cycle, if the pressure decreases.

8.2 Recommendations for Future Work

Suggestions for future work are summarised in the following statements, as are some inconclusive elements of the work in this thesis.

1. The Bunsen burner case did not include hydrogen addition, for reasons of equipment safety. However, applying a wider test range, including a fuel burning limitation, can provide stronger evidence to establish the relationship between the C_2^* chemiluminescence and the premixed mixture condition.

2. Ma, Z (2016) successfully used the Silicon carbide fibre to detect the single point temperature of a flame propagating in a tube. This improvement to detect the whole temperature during flame propagation was considered in this research, but it failed at fibre preparation since long fibre is easy to break. Temperature is an important parameter, however, and is worth developing further.

3. One of the most important aspects of flame instability is the non-linear perturbation

of premixed flames. This non-linear perturbation effect has a crucial effect on changes in flame structure, shape and combustion speed. Even so, there is no mature theoretical model for flame propagation in a tube so far. This needs to be analysed and modelled from both experimental and theoretical aspects.

4. In theory, if the tube length is long enough, the flame speed will increase and then develop to DDT. In the industrial process, the obstacles have an important effect on the progress of DDT. However, the effects of obstacles on the early acceleration stage of flames are not well studied.

9 REFERENCES

[1] Airtest (2008). Gases Characteristics. [Accessed 1 July 2016]. Available from: http://www.airtesttechnologies.com/support/technical/gasescharacteristic.htm.

[2] Akkerman, V.Y., Bychkov, V., Petchenko, A. and Eriksson, L.E., 2006. Flame oscillations in tubes with nonslip at the walls. *Combustion and Flame*, *145*(4), pp.675-687.

[3] Annamalai, K. and Puri, I.K., 2006. *Combustion science and engineering*. CRC press.

[4] Ashurst, W.T., 1994, January. Modeling turbulent flame propagation. In *Symposium (International) on Combustion* (Vol. 25, No. 1, pp. 1075-1089). Elsevier.

[5] Bai, C., Gong, G., Liu, Q., Chen, Y. and Niu, G., 2011. The explosion overpressure field and flame propagation of methane/air and methane/coal dust/air mixtures. *Safety science*, *49*(10), pp.1349-1354.

[6] Barducci, A., Guzzi, D., Marcoionni, P., & Pippi, I. (2004). A New algorithm for temperature and spectral emissivity retrieval over active fires in the TIR spectral range. IEEE transactions on geoscience and remote sensing, 42(7), pp. 1521–1529.

[7] Benjamin Wehrmann (2019). UK and Germany mull boosting cooperation on hydrogen production with offshore wind. [Accessed 15th Jan 2020]. Available from: https://www.cleanenergywire.org/news/uk-and-germany-mull-boosting-cooperation-hydrogen-production-offshore-wind.

[8] Bjerketvedt, D., Bakke, J. R., & Van Wingerden, K. (1997). Gas Explosion Handbook, 52 (96), pp. 1–150.

[9] Bozkurt, M., 2013. *Shock-tube investigation of key reactions for chemiluminescence in various combustion systems* (Doctoral dissertation).

[10] Bychkov, V., Akkerman, V.Y., Fru, G., Petchenko, A., & Eriksson, L.E. (2007). Flame acceleration in the early stages of burning in tubes. Combustion and Flame, 150(4), pp. 263–276.

[11] Cheng, 2010. Memorial to Xuesen Qian. Acta Mechanica Sinica, 26(1), pp.1-2. [73]

[12] Louër, D. & Langford, J.I., 1988. Peak shape and resolution in conventional diffractometry with monochromatic X-rays. Journal of Applied Crystallography, 21(5), pp. 430–437.

[13] Ciccarelli, G. & Dorofeev, S. (2008). Flame acceleration and transition to detonation in ducts. Progress in Energy and Combustion Science, 34(4), pp. 499–550.

[14] Clanet, C. & Searby, G. (1996). On the "Tulip flame" phenomenon. Combustion and Flame, 105(1–2), pp. 225–238.

[15] Clavin, P. (1985). Dynamic behavior of premixed flame fronts in laminar and turbulent flows. Progress in energy and combustion science, 11(1), pp. 1–59.

[16] Coats, C.M., Chang, Z., & Williams, P.D. (2010). Excitation of thermoacoustic oscillations by small premixed flames. Combustion and Flame, 157, pp. 1037–1051.

[17] Cohen, M.X. (2014). Analyzing Neural Time Series Data. Massachusetts: MIT Press.

[18] Coward, H.F. & G.W. Jones. (1952). Limits of flammability of gases and vapors. U.S., Bur. Mines Bull. Technical Report No. BM-BUMLL-503.

[19] Coward, H.F., Hartwell, F.J. (1932). Studies in the mechanism of flame movement. Part I. The Uniform movement of flame in mixtures of methane and air, in relation to tube diameter. Journal of the Chemical Society (Resumed): pp. 1996-2004.

[20] Dorofeev, S.B., 2011. Flame acceleration and explosion safety applications. Proceedings of the Combustion Institute, 33(2), pp.2161-2175.

[21] Dunn-Rankin, D. & Sawyer, R.F. (1998). Tulip flames: Changes in shape of premixed flames propagating in closed tubes. Experiments in Fluids, 24(2), pp. 130–140.

[22] Dunn-Rankin, D., Ban, P.K., & Sawyer, R.F. (1988). Numerical and experimental study of "Tulip" flame formation in a closed vessel. Symposium (Intemational) on Combustion, 21(1), pp. 1291–1301.

[23] Ebieto, C.E., 2017. Dynamics of Premixed Flames in Tube (Doctoral dissertation, University of Sheffield).

[24] Ebieto, C.E., Amaludin, N.A., Woolley, R. (2015). Methane/Hydrogen/Air Flame Oscillations in Open Ended Tubes. 25th ICDERS.

[25] Ellis, O. Cd. C. (1928). Flame movement in gaseous explosive mixtures. Journal of Fuel Science, 7, pp. 502–508.

[26] Elperin, T., Kleeorin, N., & Rogachevskii, I., 1997. Turbulent barodiffusion, turbulent thermal diffusion, and large-scale instability in gases. Physical Review

E, 55(3), p. 2713.

[27] Fleifil, M., Annaswamy, A.M., Ghoneim, Z.A., & Ghoniem, A.F. (1996). Response of a laminar premixed flame to flow oscillations: A Kinematic model and thermoacoustic instability results. Combustion and flame, 106(4), 487–510.

[28] Fristrom, R.M. & Westenberg, A.A. (1965). Flame Structure. McGraw-Hill, New York, 424 pp. 424.

[29] Gerstein, M., Levine, O., Wong, E.L. (1951). Flame propagation. II. The determination of fundamental burning velocities of hydrocarbons by a revised tube method. Journal of the American Chemical Society, 73, pp. 418–422.

[30] Gonzalez, M. (1996). Acoustic instability of a premixed flame propagating in a tube. Combustion and Flame, 107(3), pp. 245–259.

[31] Gonzalez, M., Boighi, R., & Saouab, A. (1992). Interaction of a flame front with its self-generated flow in an enclosure: The "Tulip flame" phenomenon. Combustion and Flame, 88(2), pp. 201–220.

[32] Gonzalez, R.C., Woods, R.E. and Eddins, S.L., 2004. Digital image processing using MATLAB. Pearson Education India.

[33] Hardalupas, Y. & Orain, M. (2004). Local measurements of the time-dependent heat release rate and equivalence ratio using chemiluminescent emission from a flame. Combustion and Flame. 139, pp. 188–207.

[34] Hernandez, R. & Ballester, J. (2008). Flame imaging as a diagnostic tool for industrial combustion. Combustion and Flame, 155(3), pp. 509–528.

[35] Hirschfelder, J.O. and Curtis, C.F. (1949). Theory of propagation of flames. WILKINS W.A. Third Symposium on Combustion, Flame and Explosion Phenomena. Baltimore.

[36] Huang, H.W. and Zhang, Y. (2008). Flame colour characterization in the visible and infrared spectrum using a digital camera and image processing. Meas. Sci. Technol., 19(8).

[37] Huang, H.W. and Zhang, Y., 2011. Digital colour image processing based measurement of premixed CH4+ air and C2H4+ air flame chemiluminescence. *Fuel*, *90*(1), pp.48-53.

[38] Huang, Y. & Yan, Y. (2000). Transient two-dimensional temperature measurement of open flames by dual-spectral image analysis. Transactions of the Institute of Measurement and Control, 22(5), pp. 371–384.

[39] Huang, Y., Yan, Y., Lu, G., & Reed, A. (1999). On-line flicker measurement of gaseous flames by image processing and spectral analysis. Measurement Science and Technology, 10(8), pp. 726–733.

[40] Jarosinski, J. & Veyssiere, B. (2009). Introduction: Challenges in Combustion. In Combustion Phenomena (pp. 15–16). CRC Press.

[41] Jarosinski, J. and Veyssiere, B., 2009. Instability Phenomena during Flame Propagation. In Combustion Phenomena (pp. 81-114). CRC Press.

[42] Jianfeng, P., Qian, W., Zhenhua, P., & Xia, S. (2015). Combustion Science.

[43] Jiansheng Yang. (2015). Vision-based Measurement for Combustion and Vibration

Studies. (Doctoral dissertation, University of Sheffield).

[44] Kanury, A.M. (1975). Introduction to Combustion Phenomena. London-New York: Gordon and Beach.

[45] Ke Fa, (1987). Boiler combustion test research method and measurement technology.

[46] Keenan, J.J., Makarov, D.V., & Molkov, V.V. (2014). Rayleigh–Taylor instability: Modelling and effect on coherent deflagrations. International Journal of Hydrogen Energy, 39(35), pp. 20,467–20,473.

[47] Kim, K., Lee, J., Quay, B.D., & Santavicca, D.A. (2011). The Dynamic response of turbulent dihedral V flames: An Amplification mechanism of swirling flames. Combustion and Flame, 183, pp. 163–179.

[48] Law, C.K. (2007). Combustion at a crossroads: Status and prospects. Proceedings of the Combustion Institute, 31, pp. 1–29.

[49] Liberman, M.A., Ivanov, M.F., Kiverin, A.D. et al. (2012). Deflagration-to-detonation transition in highly reactive combustible mixtures. 28th International Symposium on Shock Waves. Kontis K. Springer Berlin Heidelberg, pp. 331–336

[50] Lieuwen, T. (2003). Modeling premixed combustion-acoustic wave interactions: A Review. Journal of Propulsion and Power, 19(5), pp. 765–781.

[51] Lipatnikov, A. (2012). Fundamentals of premixed turbulent combustion. CRC Press.

[52] Lukai Zheng 2018. Combustion Visualization monitoring using high speed

imaging (Doctoral dissertation, University of Sheffield).

[53] Ma, Z., 2016. Two-colour temperature measurement based on high speed imaging (Doctoral dissertation, University of Sheffield).

[54] Mallard E. F. & Le Chatelier, H. (1883). Combustion of explosive gas mixtures. Ann Mine.

[55] Mallard, E., 1883. Recherches experimentales et theoriques sur la combustion des melanges gaseux explosifs. Ann. mines, 8(4), pp.274-568.

[56] Marbach, G., Loepfe, M., & Brupbacher, T. (2006). An Image processing technique for fire detection in video images. Fire Safety Journal, 41(4), pp. 285–289.

[57] Markstein, G.H., Guenoche, H. and Putnum, A.A., Non-steady Flame Propagation,(1964), 183.

[58] Markstein, G.H. (1957). A Shock-tube study of flame front-pressure wave interaction. In Symposium (International) on Combustion. 6, (1; January). pp. 387–398. Elsevier.

[59] Guenoche, H., 1964. Nonsteady flame propagation. Pergamon Press, New York, p.107.

[60] Marques, J.S. & Jorge, P.M. (2000). Visual inspection of a combustion process in a thermoelectric plant. Signal Processing, 80(8), pp. 1577–1589.

[61] Matalon, M. (2009). Flame Dynamics. Proceedings of the Combustion Institute, 32(1), pp. 57–82.

[62] Nolan, D.P., 2014. Handbook of fire and explosion protection engineering

principles: for oil, gas, chemical and related facilities. William Andrew.

[63] Nori, V. and Seitzman, J., 2007, January. Chemiluminescence measurements and modeling in syngas, methane and jet-A fueled combustors. In *45th AIAA Aerospace Sciences Meeting and Exhibit* (p. 466).

[64] Pande, J.O., Stokke, R.G., & Tonheim, J. (2000). Explosion of hydrogen in a pipeline for CO~ 2. Loss Prevention Bulletin, 156.

[65] Ptáček, P., Opravil, T. and Šoukal, F., 2018. Introducing an Approach to Effective Mass of Activated Complex. Introducing the Effective Mass of Activated Complex and the Discussion on the Wave Function of this Instanton, p.47.

[66] Rayleigh, J.W.S., 1896. The Theory of Sound, volume 1, chapter V, 100.

[67] Rhodes, D.B. and Keck, J.C., 1985. Laminar burning speed measurements of indolene-air-diluent mixtures at high pressures and temperatures. *SAE Transactions*, pp.23-35.

[68] Rienitz, J., 1975. Schlieren experiment 300 years ago. Nature, 254(5498), pp.293-295.

[69] Salamandra, G.D., Bazhenova, T.V., & Naboko, I.M. (1958). Formation of detonation wave during combustion of gas in combustion tube. Symposium (International) on Combustion, 7(1), pp. 851–855.

[70] Sbarbaro, D., Farias, O., & Zawadsky, A. (2003). Real-time monitoring and characterization of flames by principal-component analysis. Combustion and flame, 132(3), pp. 591–595.

[71] Searby, G. & Rochwerger, D. (1991). A Parametric acoustic instability in premixed flames. Journal of Fluid Mechanics, 231, pp. 529–543.

[72] Siniša Kekez (2018). What is a digital camera CCD? Why is it important to have to gather a cinematic look to your video? [Accessed at 18th Dec 2018] Available from: https://www.quora.com/What-is-a-digital-camera-CCD-Why-is-it-important-to-have-to-gather-a-cinematic-look-to-your-video.

[73] Sivashinsky, G.I., 1979. On self-turbulization of a laminar flame. *Acta Astronautica*, *6*(5-6), pp.569-591..

[74] Tang Zhaoting, 2011. Design of thermocouple temperature measuring instrument for spacecraft.

[75] Thakur, M., Vyas, A.L. and Shakher, C., 2001. Measurement of temperature and temperature profile of an axisymmetric gaseous flames using Lau phase interferometer with linear gratings. Optics and lasers in engineering, 36(4), pp.373-380.

[76] Tipsuwanpom, V., Krongratana, V., Gulpanich, S., & Thongnopakun, K. (2006). Fire detection using neural network. 2006 SICE-ICASE International Joint Conference, pp. 5474–5477.

[77] Victor Nikolaevich Kondratiev, (2016). History of the study of combustion. [Accessed 20 June 2016]. Available from: https://www.britannica.com/science/combustion/History-of-the-study-of-combustion.

[78] Wei Chengye, Yan Jianhua, & Shang Miner, (2003). Combustion diagnosis based on furnace flame image.

[79] West, W.E. & Westwater, J.W. (1953). Radiation-conduction correction for temperature measurements in hot gases. Industrial and Engineering Chemistry, 45(10), pp. 2152–2156.

[80] Wheeler, R.V. (1914). CCXLIII. The Propagation of flame in mixtures of methane and air. The “uniform movement.” Journal of the Chemical Society, Transactions 105, pp. 2606–2613

[81] William, F.A. (1985). Combustion Theory: The Fundamental theory of chemically reacting flow system.

[82] Xiao, H., An, W., Duan, Q. et al. (2013). Dynamics of premixed hydrogen/air flame in a closed combustion vessel. International Journal of Hydrogen Energy, 38(29), pp.12,856–12,864.

[83] Xiao, H., Shen, X. & Sun, J. (2012). Experimental study and three-dimensional simulation of premixed hydrogen/air flame propagation in a closed duct. International Journal of Hydrogen Energy, 37(15), pp. 11,466–11,473.

[84] Xiao, H., Shen, X., Guo, S., & Sun, J. (2013). An Experimental study of distorted tulip flame formation in a closed duct. Combustion and Flame. 160(9), 1725–1728.

[85] Yang, J., Mossa, F.M.S., Huang, H.W., Wang, Q., Woolley, R., & Zhang, Y. (2015). Oscillating flames in open tubes. Proc. Combust. Inst., 35(2), pp. 2075–2082.

[86] YANG, X.L. and Yan, J., 2005. Principles for the Measurement and Image

Processing Using PIV [J]. *Sichuan University of Science and Technology*, *1*.

[87] Yu, G., Law, C.K. and Wu, C.K., 1986. Laminar flame speeds of hydrocarbon+ air mixtures with hydrogen addition. Combustion and flame, 63(3), pp.339-347.

[88] Zeldowitsch, J.B. and Frank-Kamenetzki, D.A., 1988. A theory of thermal propagation of flame. In Dynamics of Curved Fronts (pp. 131-140). Academic Press.

[89] Zhang Mingchun, Xiao Yanhong, (1987). Principle and application of thermocouple temperature measurement.

[90] Mollon, J.D., 2003. The origins of modern color science. The science of color, 2, pp.1-39.

[91] Clavin, P., 2000. Dynamics of combustion fronts in premixed gases: from flames to detonations. Proceedings of the Combustion Institute, 28(1), pp.569-585.

[92] Gu, X.J., Haq, M.Z., Lawes, M. and Woolley, R., 2000. Laminar burning velocity and Markstein lengths of methane–air mixtures. *Combustion and flame*, *121*(1-2), pp.41-58.

[93] Bradley, D., Sheppart, C.G.W., Woolley, R., Greenhalgh, D.A. and Lockett, R.D., 2000. The development and structure of flame instabilities and cellularity at low Markstein numbers in explosions. *Combustion and flame*, *122*(1-2), pp.195-209.

[94] Masters, B.R., 2012. Albert Einstein and the nature of light. *Optics and Photonics News*, *23*(7), pp.42-47.

[95] Planck, M. (1913), “Theory of Heat Radiation”, second edition, english translation

put out by Dover Publ., New York, (1959). Reprinted (1991).

[96] Adamovich, I.V., Li, T. and Lempert, W.R., 2015. Kinetic mechanism of molecular energy transfer and chemical reactions in low-temperature air-fuel plasmas. *Philosophical Transactions of the Royal Society A: Mathematical, Physical and Engineering Sciences*, *373*(2048), p.20140336.

[97] Yang, J., 2016. Vision-based Measurement for Combustion and Vibration Studies (Doctoral dissertation, University of Sheffield).

[98] Huang, H. W., Wang, Q., Tang, H. J., Zhu, M., & Zhang, Y. (2012). Characterisation of external acoustic excitation on diffusion flames using digital colour image processing. *Fuel , 94*, 102-109

[99] Huang, H. W., & Zhang, Y. (2011). Digital colour image processing based measurement of premixed CH4+air and C2H4+air flame chemiluminescence. *Fuel , 90*, 48-53

[100] Wang Quan, 2006. Methane-Air premixed flame propagation in pipeline.

[101] Mitchell, A.C. and Zemansky, M.W., 2009. Resonance radiation and excited atoms. *Resonance Radiation and Excited Atoms*.

[102] Phillips, H., 1965, January. Flame in a buoyant methane layer. In *Symposium (International) on Combustion* (Vol. 10, No. 1, pp. 1277-1283). Elsevier.

[103] De Goey, L.P.H., Van Oijen, J.A., Kornilov, V.N. and ten Thije Boonkkamp, J.H.M., 2011. Propagation, dynamics and control of laminar premixed flames. *Proceedings of the Combustion Institute*, *33*(1), pp.863-886.

[104] Baukal Jr, C.E., 2000. Heat transfer in industrial combustion. CRC press.

[105] Xiao, H., Duan, Q. and Sun, J., 2018. Premixed flame propagation in hydrogen explosions. *Renewable and Sustainable Energy Reviews*, *81*, pp.1988-2001.

[106] Noorollahi, Y., Kheirrouz, M., Asl, H.F., Yousefi, H. and Hajinezhad, A., 2015. Biogas production potential from livestock manure in Iran. *Renewable and Sustainable Energy Reviews*, *50*, pp.748-754.

[107] Olah, G.A., 2005. Beyond oil and gas: the methanol economy. *Angewandte Chemie International Edition*, *44*(18), pp.2636-2639.

[108] Matalon, M., 2007. Intrinsic flame instabilities in premixed and nonpremixed combustion. *Annu. Rev. Fluid Mech.*, *39*, pp.163-191.

[109] Morgan, M.D., Mehta, S.A., Al-Himyary, T.J. and Moore, R.G., 2004, January. Detection of Combustion in Pipelines Using Flame Noise. In *Canadian International Petroleum Conference*. Petroleum Society of Canada.

[110] Bradley, D., Lawes, M., Liu, K., Verhelst, S. and Woolley, R., 2007. Laminar burning velocities of lean hydrogen–air mixtures at pressures up to 1.0 MPa. *Combustion and Flame*, *149*(1-2), pp.162-172.

[111] Zhang, Q., Qian, X., Chen, Y. and Yuan, M., 2020. Deflagration shock wave dynamics of DME/LPG blended clean fuel under the coupling effect of initial pressure and equivalence ratio in elongated closed space. *Journal of Cleaner Production*, *250*, p.119572.

[112] Shepherd, J.E. and Lee, J.H., 1992. On the transition from deflagration to

detonation. In *Major research topics in combustion* (pp. 439-487). Springer, New York, NY.

[113] YAKHOT, V., 1988. Propagation velocity of premixed turbulent flames. *Combustion Science and Technology*, *60*(1-3), pp.191-214.

[114] Einecke, S., Schulz, C. and Sick, V., 2000. Measurement of temperature, fuel concentration and equivalence ratio fields using tracer LIF in IC engine combustion. *Applied Physics B*, *71*(5), pp.717-723.

[115] Lasek, J.A., Kopczyński, M., Janusz, M., Iluk, A. and Zuwała, J., 2017. Combustion properties of torrefied biomass obtained from flue gas-enhanced reactor. *Energy*, *119*, pp.362-368.

[116] Marr, M.A., Wallace, J.S., Chandra, S., Pershin, L. and Mostaghimi, J., 2010. A fast response thermocouple for internal combustion engine surface temperature measurements. *Experimental thermal and fluid science*, *34*(2), pp.183-189.

[117] Intajag, S., Tipsuwanporn, V. and Chatthai, R., 2009, March. Retinal image enhancement in multi-mode histogram. In 2009 WRI World Congress on Computer Science and Information Engineering (Vol. 4, pp. 745-749). IEEE.

10 APPENDIX

10.1 Flame Temperature Technique

10.1.1 Introduction

The burning of fossil fuels is the most common method for energy consumption around the world, a trend that will continue over the following decades. Emissions from burning fossil fuels include carbon oxides, nitrogen oxides, volatile organic compounds, polycyclic aromatic hydrocarbons, sulphur oxide, black smoke and dust. The production and emissions of these pollutants don't just reduce combustion efficiency—they also harm the environment and human health.

Combustion pollutants are associated with the combustion process. The radiation characteristics of flame temperature and radiation medium are two important parameters to reflect the combustion process. Measuring these two parameters accurately plays a guiding role in researching the combustion mechanism and is of great significance in understanding the production and release of heating (radiation, convection and thermal conductivity) in the combustion process.

10.1.2 Contact Thermometry

Conventional temperature measurement includes two major categories: contact and non-contact thermometry. Contact thermometry refers to the method that directly places the temperature-measuring element into the burning flame and brings the elements into contact with the flame. This method is direct and simple. The most common type of contact thermometry is thermocouple thermometry (Ke 1987). The thermocouple forms a loop using two different metals as a conductor. Its two ends meet and, at the same time, produce a thermoelectric force under different temperature conditions (Zhamg 1987).

A thermocouple needs to be placed into the chamber and in contact with the flame directly; errors will therefore occur, due to the interference of other mediums in the combustion field (West 1954). In general, however, thermocouple thermometry has the advantages of employing simple equipment and being accurate and easy to maintain. Thus, thermocouple thermometry has been widely used in the field of industrial and scientific research (Tang 2011). The main disadvantage of contact thermometry is the disturbance to the flame. A secondary limitation is that the temperature status of only a single point can be measured at any one time. A large number of points need to be measured, to determine the temperature distribution of the whole combustion pipe; the installation of this setup is difficult.

10.1.3 Non-contact Thermometry

Non-contact thermometry uses components that do not contact the combustion flame to measure flame temperature. Non-contact thermometry mainly includes optical thermometry and acoustic thermometry. Optical thermometry makes use of the radiation characteristics of the combustion flame and optical principles to measure the temperature of the flame. Optical thermometry specifically covers radiation thermometry, which uses the radiation intensity of the infrared or visible light to measure the temperature (Barducci et al. 2004), and laser thermometry (Thakur et al. 2001), which measures temperature by taking advantage of Rayleigh scattering. The use of optical thermometry requires the pipeline windows to be kept free of pollution, to allow for a clear view.

Compared to contact thermometry, the principle of non-contact thermometry is more complicated. However, non-contact thermometry has advantages: 1) it is not easily disturbed by the object being measured and 2) the temperature measurement range is not affected by materials; hence, it is more suitable under the circumstances of high temperatures. Meanwhile, non-contact thermometry can measure temperature distribution without the need to arrange a large number of measuring points, as required in contact thermometry.

10.1.4 Two-Colour Temperature Technique Using a Signal Camera

The use of a digital camera to quantify temperature is not new. However, it is difficult to apply the technique to high temperature measurements due to the image saturation problem (Ma 2016). To avoid this issue, digital high-speed cameras with high shutter speeds provide an excellent tool for high temperature measurements. The advantages of temperature measurement techniques based on digital images include their less intrusive nature, their fast-responding features and the fact that such devices are easy to set up.

Utilising a camera to measure the flame temperature relies on the two-colour principle, which in turn depends on recording the flame or light source radiation. The principle of the method of two-colour temperature measurement is derived using the blackbody assumption of flame radiation, combined with Planck's Law and Wien's Law.

Temperature and radiation generally conform to Planck's Law during the combustion process. For the combustion flame, Planck's Law can be replaced with Wien's Law, and monochromatic radiation can be shown as:

$$\mathrm{I}(\lambda, \mathrm{T}) = \varepsilon(\lambda, \mathrm{T}) \frac{C_1}{\lambda^5} \exp\left(-\frac{C_2}{\lambda T}\right) \tag{10.1}$$

where λ is wavelength and T is the absolute temperature. $\mathrm{I}(\lambda, \mathrm{T})$ is the flame

emissivity at T and λ conditions, and C1 and C2 are Planck's first and second constant, with values of 3.7419×10^{-16} W·m^2 and 1.4388×10^{-2} m·K respectively.

Combining the characteristics of colour imagery, it can be assumed that the values of the R, G and B channels should be proportional to the red, green and blue radiation wavelengths in the photosensitive element.

Therefore:

$$\mathrm{R(T)} = k_R \varepsilon(\lambda_R, T) \frac{C_1}{\lambda_R^5} \exp\left(-\frac{C_2}{\lambda_R T}\right) \tag{10.2}$$

$$\mathrm{G(T)} = k_G \varepsilon(\lambda_G, T) \frac{C_1}{\lambda_G^5} \exp\left(-\frac{C_2}{\lambda_G T}\right) \tag{10.3}$$

$$\mathrm{B(T)} = k_B \varepsilon(\lambda_B, T) \frac{C_1}{\lambda_B^5} \exp\left(-\frac{C_2}{\lambda_B T}\right) \tag{10.4}$$

λ_R, λ_G and λ_B are the wavelengths of the red, green and blue channels respectively; they are constants. R(T), G(T) and B(T) are the R, G and B values of image pixels at T temperature's radiation.

k_R, k_G and k_B are attenuation coefficients for the R, G and B channels, and they are constant, except for light pathway changes.

If the radiation source is blackbody, then:

$$\mathrm{R}_b\mathrm{(T)} = k_R \frac{C_1}{\lambda_R^5} \exp\left(-\frac{C_2}{\lambda_R T}\right) \tag{10.5}$$

$$\mathrm{G}_b\mathrm{(T)} = k_G \frac{C_1}{\lambda_G^5} \exp\left(-\frac{C_2}{\lambda_G T}\right) \tag{10.6}$$

$$\mathrm{B}_b\mathrm{(T)} = k_B \frac{C_1}{\lambda_B^5} \exp\left(-\frac{C_2}{\lambda_B T}\right) \tag{10.7}$$

$\mathrm{R}_b\mathrm{(T)}$, $\mathrm{G}_b\mathrm{(T)}$ and $\mathrm{B(T)}$ are the values for the R, G and B channels of image pixels under T temperature's blackbody radiation.

Combined equations:

$$\mathrm{R(T)} = \varepsilon(\lambda_R, T)\mathrm{R}_b(\mathrm{T}) \tag{10.8}$$

$$\mathrm{G(T)} = \varepsilon(\lambda_G, T)\mathrm{G}_b(\mathrm{T}) \tag{10.9}$$

$$\mathrm{B(T)} = \varepsilon(\lambda_B, T)\mathrm{B}_b(\mathrm{T}) \tag{10.10}$$

Utilise the grey body assumption:

$$\varepsilon(\lambda_R, T) = \varepsilon(\lambda_G, T) = \varepsilon(\lambda_B, T) = \varepsilon(T) \tag{10.11}$$

Substitute to equations:

$$\frac{\mathrm{R(T)}}{\mathrm{R}_b(\mathrm{T})} = \frac{\mathrm{G(T)}}{\mathrm{G}_b(\mathrm{T})} = \frac{\mathrm{B(T)}}{\mathrm{B}_b(\mathrm{T})} = \varepsilon(T) \tag{10.12}$$

Transfer equation:

$$\frac{\mathrm{R(T)}}{\mathrm{G(T)}} = \frac{\mathrm{R}_b(\mathrm{T})}{\mathrm{G}_b(\mathrm{T})} = S_{rg} \tag{10.13}$$

S_{rg} is the value of the R to G ratio under T temperature. According to the above equations, when there are no blackbody or grey body sources, the value of the R to G channel ratio is related only to T temperature. Therefore, it is useful to utilise the blackbody source to obtain the relationship between the temperature and the R to G ratio, to measure the temperature of the combustion flame.

10.2 Fuel-Air Ratio Calculator

CH4

Fuel/ AIR = 1

$$CH_4 + 2O_2 = CO_2 + H_2O$$

$V_{CH_4} : V_{O_2}$ =1: 2

$\frac{V_{O_2}}{V_{air}} = 20.942\%$

$V_{CH_4}: V_{air}$ =1: $\frac{2}{20.942\%}$ =9.55

- **For air:** Use the Rotameter of CO2 instead of air.

$$Q_{gas} = \sqrt{\frac{\rho_{gas}}{\rho_{rotameter}}}\, Q_{rotameter}$$

$$\rightarrow \quad Q_{air} = \sqrt{\frac{\rho_{air}}{\rho_{co_2}}}\, Q_{rotameter}$$

$$\rightarrow \quad 9.55 = \sqrt{\frac{1.204}{1.977}}\, Q_{rotameter}$$

$$\rightarrow Q_{rotameter} = 12.237$$

- **For air:** Use the Rotameter of CH4

$$Q_{rotameter} = 1$$

SO,

$$Rotameter_{CH_4}: Rotameter_{air} = 1: 12.237$$

C3H8 Fuel/ AIR = 1

$$C_3H_8 + 5O_2 = 3CO_2 + 4H_2O$$

$V_{C_3H_8} : V_{O_2}$ =1: 5

$\frac{V_{O_2}}{V_{air}} = 20.942\%$

$V_{CH_4}: V_{air}$ =1: $\frac{5}{20.942\%}$ =23.875

- **For air:** Use the Rotameter of CO2 instead of air.

$$Q_{gas} = \sqrt{\frac{\rho_{gas}}{\rho_{rotameter}}}\, Q_{rotameter}$$

$$\rightarrow \quad Q_{air} = \sqrt{\frac{\rho_{air}}{\rho_{co_2}}}\, Q_{rotameter}$$

$$\rightarrow \quad 23.875 = \sqrt{\frac{1.204}{1.977}}\, Q_{rotameter}$$

$$\rightarrow Q_{rotameter} = 30.609$$

- **For fuel:** Use the Rotameter of CH4 instead of C3H8

$$Q_{gas} = \sqrt{\frac{\rho_{gas}}{\rho_{rotameter}}}\, Q_{rotameter}$$

$$\rightarrow \quad Q_{C_3H_8} = \sqrt{\frac{\rho_{C_3H_8}}{\rho_{CH_4}}}\, Q_{rotameter}$$

$$\rightarrow \quad 1 = \sqrt{\frac{1.898}{0.6998}}\, Q_{rotameter}$$

$$\rightarrow Q_{rotameter} = 0.607$$

SO,

$$Rotameter_{C_3H_8}: Rotameter_{air} = 0.607: 30.609 = 1: 50.427$$

10.3 Fuel Calculator and Characteristics for Hydrogen Addition

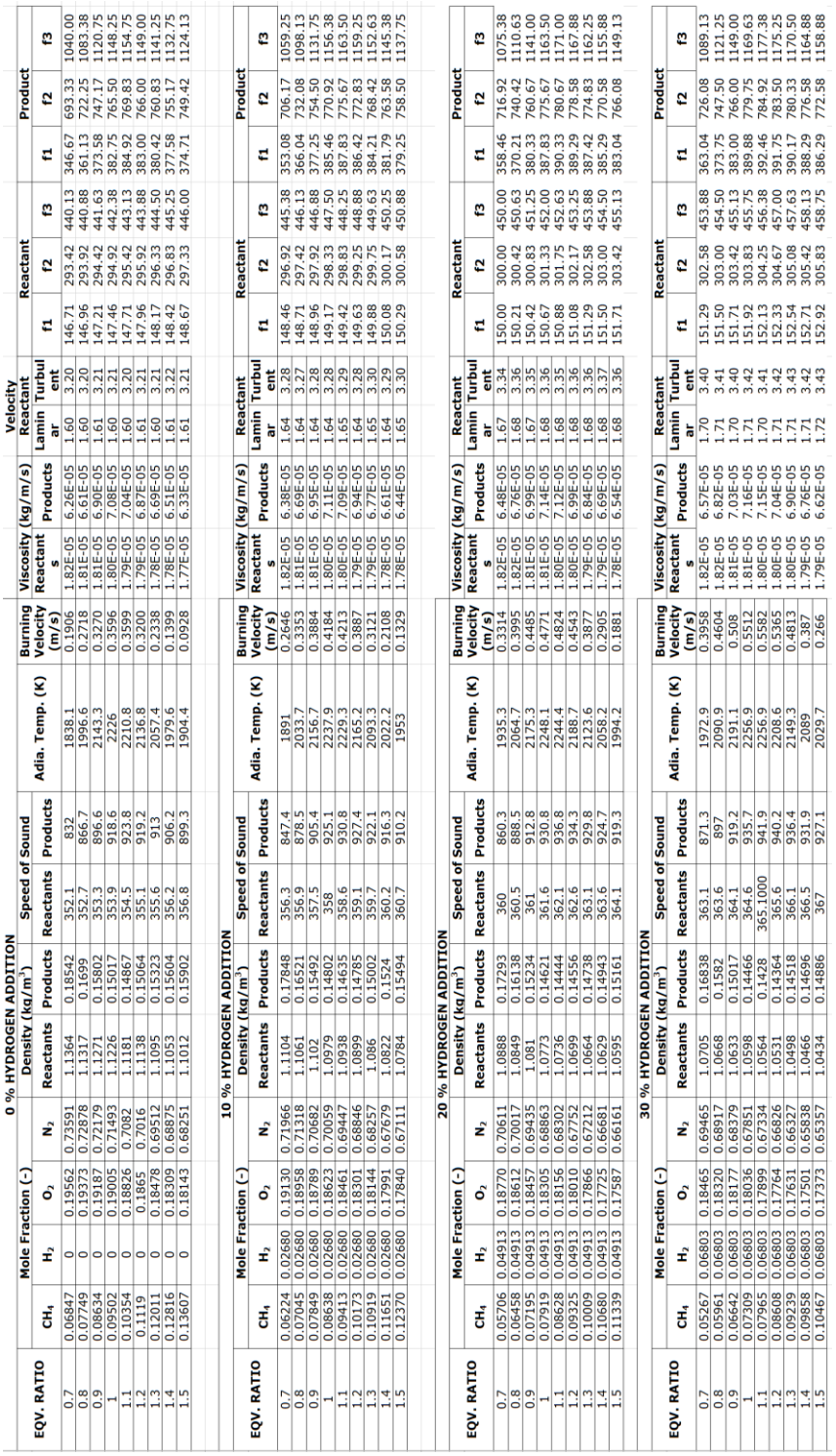

0 % HYDROGEN ADDITION

EQV. RATIO	Mole Fraction (-)				Density (kg/m³)		Speed of Sound		Adia. Temp. (K)	Burning Velocity (m/s)	Viscosity (kg/m/s)		Velocity		Reactant			Product		
	CH_4	H_2	O_2	N_2	Reactants	Products	Reactants	Products			Reactants	Products	Laminar	Turbulent	f1	f2	f3	f1	f2	f3
0.7	0.06847	0	0.19562	0.73591	1.1364	0.18542	352.1	832	1838.1	0.1906	1.82E-05	6.26E-05	1.60	3.20	146.71	293.42	440.13	346.67	693.33	1040.00
0.8	0.07749	0	0.19373	0.72878	1.1317	0.1699	352.7	866.7	1996.6	0.2718	1.81E-05	6.61E-05	1.60	3.20	146.96	293.92	440.88	361.13	722.25	1083.38
0.9	0.08634	0	0.19187	0.72179	1.1271	0.15802	353.3	896.6	2143.3	0.3270	1.81E-05	6.90E-05	1.61	3.21	147.21	294.42	441.63	373.58	747.17	1120.75
1	0.09502	0	0.19005	0.71493	1.1226	0.15017	353.9	918.6	2226	0.3596	1.80E-05	7.08E-05	1.60	3.21	147.46	294.92	442.38	382.75	765.50	1148.25
1.1	0.10354	0	0.18826	0.7082	1.1181	0.14867	354.5	923.8	2210.8	0.3599	1.79E-05	7.04E-05	1.60	3.20	147.71	295.42	443.13	384.92	769.83	1154.75
1.2	0.1119	0	0.1865	0.7016	1.1138	0.15064	355.1	919.2	2136.8	0.3200	1.79E-05	6.87E-05	1.61	3.21	147.96	295.92	443.88	383.00	766.00	1149.00
1.3	0.12011	0	0.18478	0.69512	1.1095	0.15323	355.6	913	2057.4	0.2338	1.78E-05	6.69E-05	1.60	3.21	148.17	296.33	444.50	380.42	760.83	1141.25
1.4	0.12816	0	0.18309	0.68875	1.1053	0.15604	356.2	906.2	1979.6	0.1399	1.78E-05	6.51E-05	1.61	3.22	148.42	296.83	445.25	377.58	755.17	1132.75
1.5	0.13607	0	0.18143	0.68251	1.1012	0.15902	356.8	899.3	1904.4	0.0928	1.77E-05	6.33E-05	1.61	3.21	148.67	297.33	446.00	374.71	749.42	1124.13

10 % HYDROGEN ADDITION

EQV. RATIO	Mole Fraction (-)				Density (kg/m³)		Speed of Sound		Adia. Temp. (K)	Burning Velocity (m/s)	Viscosity (kg/m/s)		Velocity		Reactant			Product		
	CH_4	H_2	O_2	N_2	Reactants	Products	Reactants	Products			Reactants	Products	Laminar	Turbulent	f1	f2	f3	f1	f2	f3
0.7	0.06224	0.02680	0.19130	0.71966	1.1104	0.17848	356.3	847.4	1891	0.2646	1.82E-05	6.38E-05	1.64	3.28	148.46	296.92	445.38	353.08	706.17	1059.25
0.8	0.07045	0.02680	0.18958	0.71318	1.1061	0.16521	356.9	878.5	2033.7	0.3353	1.81E-05	6.69E-05	1.64	3.27	148.71	297.42	446.13	366.04	732.08	1098.13
0.9	0.07849	0.02680	0.18789	0.70682	1.102	0.15492	357.5	905.4	2156.7	0.3884	1.81E-05	6.95E-05	1.64	3.28	148.96	297.92	446.88	377.25	754.50	1131.75
1	0.08638	0.02680	0.18623	0.70059	1.0979	0.14802	358	925.1	2237.9	0.4184	1.80E-05	7.11E-05	1.64	3.28	149.17	298.33	447.50	385.46	770.92	1156.38
1.1	0.09413	0.02680	0.18461	0.69447	1.0938	0.14635	358.6	930.8	2229.3	0.4213	1.80E-05	7.09E-05	1.65	3.29	149.42	298.83	448.25	387.83	775.67	1163.50
1.2	0.10173	0.02680	0.18301	0.68846	1.0899	0.14785	359.1	927.4	2165.2	0.3887	1.79E-05	6.94E-05	1.64	3.28	149.63	299.25	448.88	386.42	772.83	1159.25
1.3	0.10919	0.02680	0.18144	0.68257	1.086	0.15002	359.7	922.1	2093.3	0.3121	1.79E-05	6.77E-05	1.65	3.30	149.88	299.75	449.63	384.21	768.42	1152.63
1.4	0.11651	0.02680	0.17991	0.67679	1.0822	0.1524	360.2	916.3	2022.2	0.2108	1.78E-05	6.61E-05	1.64	3.29	150.08	300.17	450.25	381.79	763.58	1145.38
1.5	0.12370	0.02680	0.17840	0.67111	1.0784	0.15494	360.7	910.2	1953	0.1329	1.78E-05	6.44E-05	1.65	3.30	150.29	300.58	450.88	379.25	758.50	1137.75

20 % HYDROGEN ADDITION

EQV. RATIO	Mole Fraction (-)				Density (kg/m³)		Speed of Sound		Adia. Temp. (K)	Burning Velocity (m/s)	Viscosity (kg/m/s)		Velocity		Reactant			Product		
	CH_4	H_2	O_2	N_2	Reactants	Products	Reactants	Products			Reactants	Products	Laminar	Turbulent	f1	f2	f3	f1	f2	f3
0.7	0.05706	0.04913	0.18770	0.70611	1.0888	0.17293	360	860.3	1935.3	0.3314	1.82E-05	6.48E-05	1.67	3.34	150.00	300.00	450.00	358.46	716.92	1075.38
0.8	0.06458	0.04913	0.18612	0.70017	1.0849	0.16138	360.5	888.5	2064.7	0.3995	1.82E-05	6.76E-05	1.68	3.36	150.21	300.42	450.63	370.21	740.42	1110.63
0.9	0.07195	0.04913	0.18457	0.69435	1.081	0.15234	361	912.8	2175.3	0.4485	1.81E-05	6.99E-05	1.67	3.35	150.42	300.83	451.25	380.33	760.67	1141.00
1	0.07919	0.04913	0.18305	0.68863	1.0773	0.14621	361.6	930.8	2248.1	0.4771	1.81E-05	7.14E-05	1.68	3.36	150.67	301.33	452.00	387.83	775.67	1163.50
1.1	0.08628	0.04913	0.18156	0.68302	1.0736	0.14444	362.1	936.8	2244.4	0.4824	1.80E-05	7.12E-05	1.68	3.35	150.88	301.75	452.63	390.33	780.67	1171.00
1.2	0.09325	0.04913	0.18010	0.67752	1.0699	0.14556	362.6	934.3	2188.7	0.4543	1.80E-05	6.99E-05	1.68	3.36	151.08	302.17	453.25	389.29	778.58	1167.88
1.3	0.10009	0.04913	0.17866	0.67212	1.0664	0.14738	363.1	929.8	2123.6	0.3877	1.79E-05	6.84E-05	1.68	3.36	151.29	302.58	453.88	387.42	774.83	1162.25
1.4	0.10680	0.04913	0.17725	0.66681	1.0629	0.14943	363.6	924.7	2058.2	0.2905	1.79E-05	6.69E-05	1.68	3.37	151.50	303.00	454.50	385.29	770.58	1155.88
1.5	0.11339	0.04913	0.17587	0.66161	1.0595	0.15161	364.1	919.3	1994.2	0.1881	1.78E-05	6.54E-05	1.68	3.36	151.71	303.42	455.13	383.04	766.08	1149.13

30 % HYDROGEN ADDITION

EQV. RATIO	Mole Fraction (-)				Density (kg/m³)		Speed of Sound		Adia. Temp. (K)	Burning Velocity (m/s)	Viscosity (kg/m/s)		Velocity		Reactant			Product		
	CH_4	H_2	O_2	N_2	Reactants	Products	Reactants	Products			Reactants	Products	Laminar	Turbulent	f1	f2	f3	f1	f2	f3
0.7	0.05267	0.06803	0.18465	0.69465	1.0705	0.16838	363.1	871.3	1972.9	0.3958	1.82E-05	6.57E-05	1.70	3.40	151.29	302.58	453.88	363.04	726.08	1089.13
0.8	0.05961	0.06803	0.18320	0.68917	1.0668	0.1582	363.6	897	2090.9	0.4604	1.82E-05	6.82E-05	1.71	3.41	151.50	303.00	454.50	373.75	747.50	1121.25
0.9	0.06642	0.06803	0.18177	0.68379	1.0633	0.15017	364.1	919.2	2191.1	0.508	1.81E-05	7.03E-05	1.70	3.40	151.71	303.42	455.13	383.00	766.00	1149.00
1	0.07309	0.06803	0.18036	0.67851	1.0598	0.14466	364.6	935.7	2256.9	0.5512	1.81E-05	7.16E-05	1.71	3.42	151.92	303.83	455.75	389.88	779.75	1169.63
1.1	0.07965	0.06803	0.17899	0.67334	1.0564	0.1428	365.1000	941.9	2256.9	0.5582	1.80E-05	7.15E-05	1.70	3.41	152.13	304.25	456.38	392.46	784.92	1177.38
1.2	0.08608	0.06803	0.17764	0.66826	1.0531	0.14364	365.6	940.2	2208.6	0.5365	1.80E-05	7.04E-05	1.71	3.42	152.33	304.67	457.00	391.75	783.50	1175.25
1.3	0.09239	0.06803	0.17631	0.66327	1.0498	0.14518	366.1	936.4	2149.3	0.4813	1.80E-05	6.90E-05	1.71	3.43	152.54	305.08	457.63	390.17	780.33	1170.50
1.4	0.09858	0.06803	0.17501	0.65838	1.0466	0.14696	366.5	931.9	2089	0.387	1.79E-05	6.78E-05	1.71	3.42	152.71	305.42	458.13	388.29	776.58	1164.88
1.5	0.10467	0.06803	0.17373	0.65357	1.0434	0.14886	367	927.1	2029.7	0.266	1.79E-05	6.62E-05	1.72	3.43	152.92	305.83	458.75	386.29	772.58	1158.88

Figure 10-1 Fuel Calculator and Characteristics of 0%,10%,20%,30% Hydrogen Addition.

40 % HYDROGEN ADDITION

EQV. RATIO	Mole Fraction (-)				Density (kg/m³)		Speed of Sound		Adia. Temp. (K)	Burning Velocity (m/s)	Viscosity (kg/m/s)		Reactant			Reactant			Product		
	CH_4	H_2	O_2	N_2	Reactants	Products	Reactants	Products			Reactants	Products	Laminar	Turbulent	f1	f2	f3	f1	f2	f3
0.7	0.04891	0.08422	0.18204	0.68483	1.0548	0.1646	365.9	880.8	2005.2	0.4572	1.82E-05	6.64E-05	1.73	3.45	152.46	304.92	457.38	367.00	734.00	1101.00
0.8	0.05535	0.08422	0.18069	0.67974	1.0514	0.15553	366.3	904.4	2113.3	0.5267	1.82E-05	6.87E-05	1.73	3.46	152.63	305.25	457.88	376.83	753.67	1130.50
0.9	0.06167	0.08422	0.17936	0.67474	1.0481	0.14831	366.8	924.8	2204.6	0.5788	1.81E-05	7.06E-05	1.73	3.45	152.83	305.67	458.50	385.33	770.67	1156.00
1	0.06787	0.08422	0.17806	0.66984	1.0449	0.14331	367.3	940	2264.6	0.6103	1.81E-05	7.18E-05	1.73	3.46	153.04	306.08	459.13	391.67	783.33	1175.00
1.1	0.07396	0.08422	0.17678	0.66504	1.0417	0.14148	367.8	946.2	2267.3	0.6179	1.81E-05	7.18E-05	1.74	3.48	153.25	306.50	459.75	394.25	788.50	1182.75
1.2	0.07993	0.08422	0.17553	0.66032	1.0386	0.14202	368.2	945.3	2225.4	0.599	1.80E-05	7.08E-05	1.73	3.47	153.42	306.83	460.25	393.88	787.75	1181.63
1.3	0.08579	0.08422	0.17430	0.65569	1.0356	0.14333	368.7	942.1	2171.4	0.5506	1.80E-05	6.95E-05	1.74	3.48	153.63	307.25	460.88	392.54	785.08	1177.63
1.4	0.09154	0.08422	0.17309	0.65114	1.0326	0.14488	369.1	938.1	2115.7	0.4709	1.79E-05	6.82E-05	1.73	3.47	153.79	307.58	461.38	390.88	781.75	1172.63
1.5	0.09719	0.08422	0.17190	0.64668	1.0296	0.14656	369.6	933.9	2060.4	0.3581	1.79E-05	6.69E-05	1.74	3.48	154.00	308.00	462.00	389.13	778.25	1167.38

50 % HYDROGEN ADDITION

EQV. RATIO	Mole Fraction (-)				Density (kg/m³)		Speed of Sound		Adia. Temp. (K)	Burning Velocity (m/s)	Viscosity (kg/m/s)		Reactant			Reactant			Product		
	CH_4	H_2	O_2	N_2	Reactants	Products	Reactants	Products			Reactants	Products	Laminar	Turbulent	f1	f2	f3	f1	f2	f3
0.7	0.04565	0.09826	0.17978	0.67631	1.0411	0.1614	368.3	889.1	2033.1	0.52	1.82E-05	6.70E-05	1.75	3.50	153.46	306.92	460.38	370.46	740.92	1111.38
0.8	0.05166	0.09826	0.17852	0.67156	1.038	0.15323	368.8	910.9	2132.7	0.5874	1.82E-05	6.91E-05	1.75	3.51	153.67	307.33	461.00	379.54	759.08	1138.63
0.9	0.05756	0.09826	0.17728	0.66690	1.0349	0.1467	369.2	929.7	2116.4	0.638	1.82E-05	7.09E-05	1.76	3.52	153.83	307.67	461.50	387.38	774.75	1162.13
1	0.06335	0.09826	0.17606	0.66233	1.0319	0.14213	369.7	943.8	2271.4	0.6687	1.81E-05	7.20E-05	1.75	3.51	154.04	308.08	462.13	393.25	786.50	1179.75
1.1	0.06903	0.09826	0.17487	0.65784	1.029	0.14031	370.1	950.1	2276.1	0.6768	1.81E-05	7.20E-05	1.76	3.52	154.21	308.42	462.63	395.88	791.75	1187.63
1.2	0.07460	0.09826	0.17370	0.65344	1.0261	0.14064	370.6	949.7	2239.8	0.6601	1.80E-05	7.11E-05	1.75	3.51	154.42	308.83	463.25	395.71	791.42	1187.13
1.3	0.08007	0.09826	0.17255	0.64912	1.0232	0.14174	371	947	2190.5	0.6162	1.80E-05	7.00E-05	1.76	3.52	154.58	309.17	463.75	394.58	789.17	1183.75
1.4	0.08544	0.09826	0.17142	0.64488	1.0204	0.1431	371.4	943.5	2138.8	0.545	1.80E-05	6.88E-05	1.76	3.53	154.75	309.50	464.25	393.13	786.25	1179.38
1.5	0.09071	0.09826	0.17032	0.64071	1.0177	0.14458	371.8	939.7	2087.4	0.4481	1.79E-05	6.76E-05	1.76	3.52	154.92	309.83	464.75	391.54	783.08	1174.63

60 % HYDROGEN ADDITION

EQV. RATIO	Mole Fraction (-)				Density (kg/m³)		Speed of Sound		Adia. Temp. (K)	Burning Velocity (m/s)	Viscosity (kg/m/s)		Reactant			Reactant			Product		
	CH_4	H_2	O_2	N_2	Reactants	Products	Reactants	Products			Reactants	Products	Laminar	Turbulent	f1	f2	f3	f1	f2	f3
0.7	0.04279	0.11054	0.17780	0.66887	1.0292	0.15876	370.5	896.4	2057.3	0.5813	1.83E-05	6.75E-05	1.78	3.56	154.38	308.75	463.13	373.50	747.00	1120.50
0.8	0.04843	0.11054	0.17662	0.66441	1.0263	0.15126	370.9	916.7	2149.5	0.647	1.82E-05	6.95E-05	1.77	3.55	154.54	309.08	463.63	381.96	763.92	1145.88
0.9	0.05396	0.11054	0.17545	0.66004	1.0234	0.1453	371.4	934.1	2226.7	0.6961	1.82E-05	7.11E-05	1.78	3.56	154.75	309.50	464.25	389.21	778.42	1167.63
1	0.05939	0.11054	0.17431	0.65575	1.0206	0.14109	371.8	947.3	2277.5	0.7261	1.81E-05	7.21E-05	1.77	3.55	154.92	309.83	464.75	394.71	789.42	1184.13
1.1	0.06471	0.11054	0.17320	0.65155	1.0178	0.13929	372.2	953.5	2283.7	0.7347	1.81E-05	7.22E-05	1.78	3.56	155.08	310.17	465.25	397.29	794.58	1191.88
1.2	0.06994	0.11054	0.17210	0.64742	1.0151	0.13945	372.6	953.6	2252.1	0.7198	1.81E-05	7.14E-05	1.78	3.57	155.25	310.50	465.75	397.33	794.67	1192.00
1.3	0.07507	0.11054	0.17102	0.64337	1.0124	0.14038	373	951.3	2207.1	0.6797	1.80E-05	7.04E-05	1.78	3.56	155.42	310.83	466.25	396.38	792.75	1189.13
1.4	0.08010	0.11054	0.16996	0.63939	1.0098	0.14157	373.5	948.3	2159.1	0.6144	1.80E-05	6.92E-05	1.78	3.57	155.63	311.25	466.88	395.13	790.25	1185.38
1.5	0.08504	0.11054	0.16893	0.63549	1.0073	0.14289	373.9	944.8	2111	0.5269	1.79E-05	6.81E-05	1.78	3.55	155.79	311.58	467.38	393.67	787.33	1181.00

70 % HYDROGEN ADDITION

EQV. RATIO	Mole Fraction (-)				Density (kg/m³)		Speed of Sound		Adia. Temp. (K)	Burning Velocity (m/s)	Viscosity (kg/m/s)		Reactant			Reactant			Product		
	CH_4	H_2	O_2	N_2	Reactants	Products	Reactants	Products			Reactants	Products	Laminar	Turbulent	f1	f2	f3	f1	f2	f3
0.7	0.04028	0.12138	0.17605	0.66229	1.0187	0.15629	372.4	902.9	2078.8	0.6414	1.83E-05	6.80E-05	1.80	3.59	155.17	310.33	465.50	376.21	752.42	1128.63
0.8	0.04558	0.12138	0.17494	0.65810	1.016	0.14953	372.9	921.7	2164.4	0.7052	1.82E-05	6.98E-05	1.79	3.58	155.38	310.75	466.13	384.04	768.08	1152.13
0.9	0.05079	0.12138	0.17384	0.65399	1.0133	0.14406	373.3	938	2235.8	0.7531	1.82E-05	7.13E-05	1.80	3.59	155.54	311.08	466.63	390.83	781.67	1172.50
1	0.05590	0.12138	0.17277	0.64995	1.0106	0.14017	373.7	950.3	2282.9	0.7826	1.81E-05	7.23E-05	1.79	3.58	155.71	311.42	467.13	395.96	791.92	1187.88
1.1	0.06091	0.12138	0.17172	0.64599	1.008	0.13839	374.1	956.4	2290.3	0.7915	1.81E-05	7.24E-05	1.80	3.59	155.88	311.75	467.63	398.50	797.00	1195.50
1.2	0.06582	0.12138	0.17069	0.64211	1.0054	0.13841	374.5	957	2262.9	0.7783	1.81E-05	7.17E-05	1.80	3.60	156.04	312.08	468.13	398.75	797.50	1196.25
1.3	0.07065	0.12138	0.16967	0.63830	1.0029	0.13919	374.9	955.2	2221.7	0.7414	1.80E-05	7.07E-05	1.79	3.59	156.21	312.42	468.63	398.00	796.00	1194.00
1.4	0.07539	0.12138	0.16868	0.63455	1.0005	0.14024	375.3	952.5	2177.1	0.6809	1.80E-05	6.97E-05	1.80	3.60	156.38	312.75	469.13	396.88	793.75	1190.63
1.5	0.08004	0.12138	0.16770	0.63088	0.998	0.14143	375.7	949.4	2131.8	0.5994	1.80E-05	6.86E-05	1.80	3.61	156.54	313.08	469.63	395.58	791.17	1186.75

Figure 10-2 Fuel Calculator and Characteristics of 40%,50%,60%,70% Hydrogen Addition.

10.4 Pure Methane Flame Propagation in Vertical Tube at Equivalence Ratio 1.1, 1.2 and 1.3.

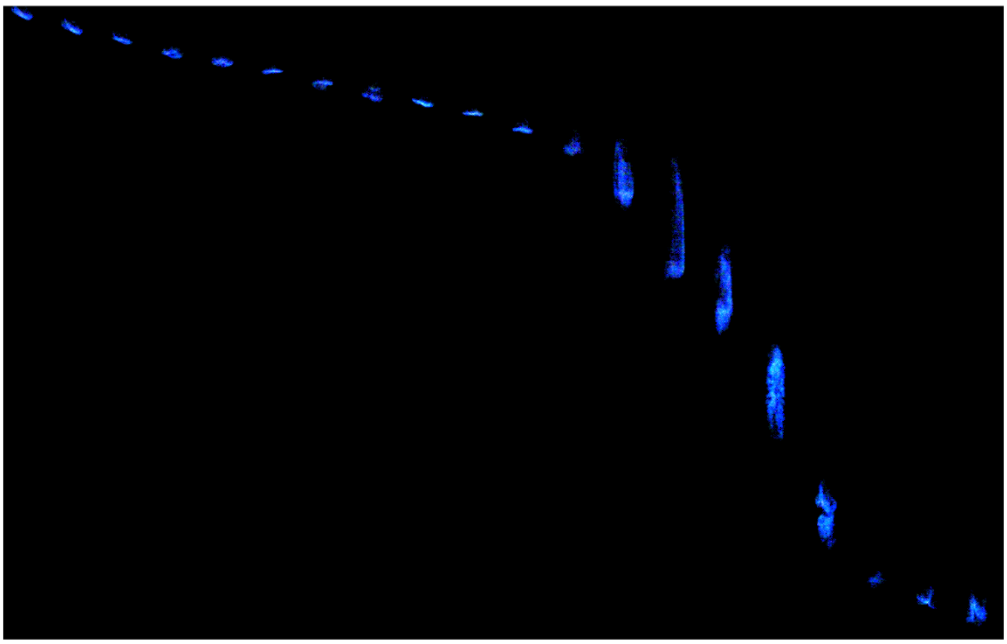

Figure 10-3 1.1 Methane without hydrogen.

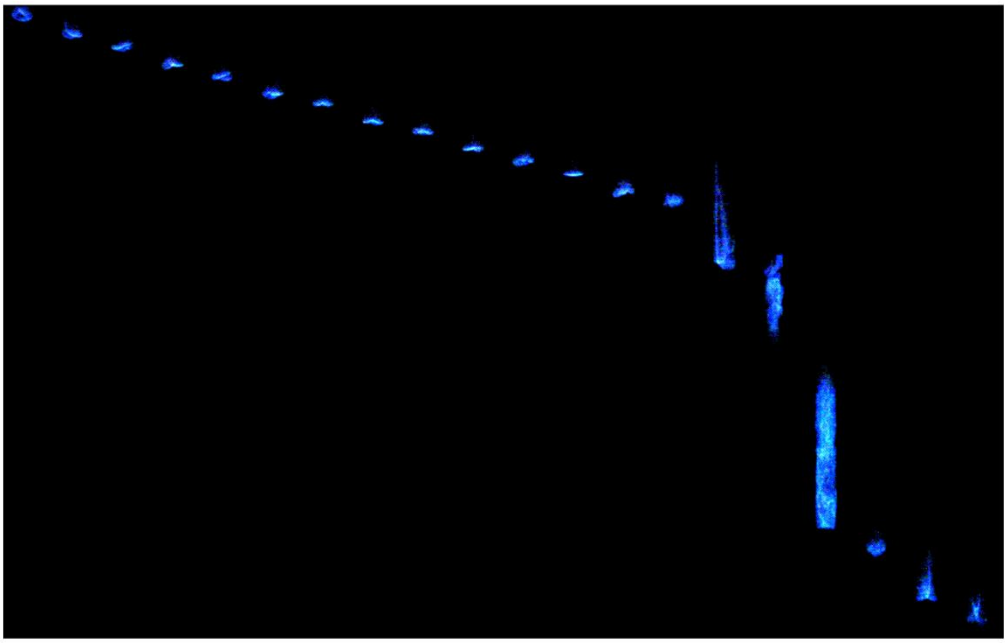

Figure 10-4 1.2 Methane without hydrogen.

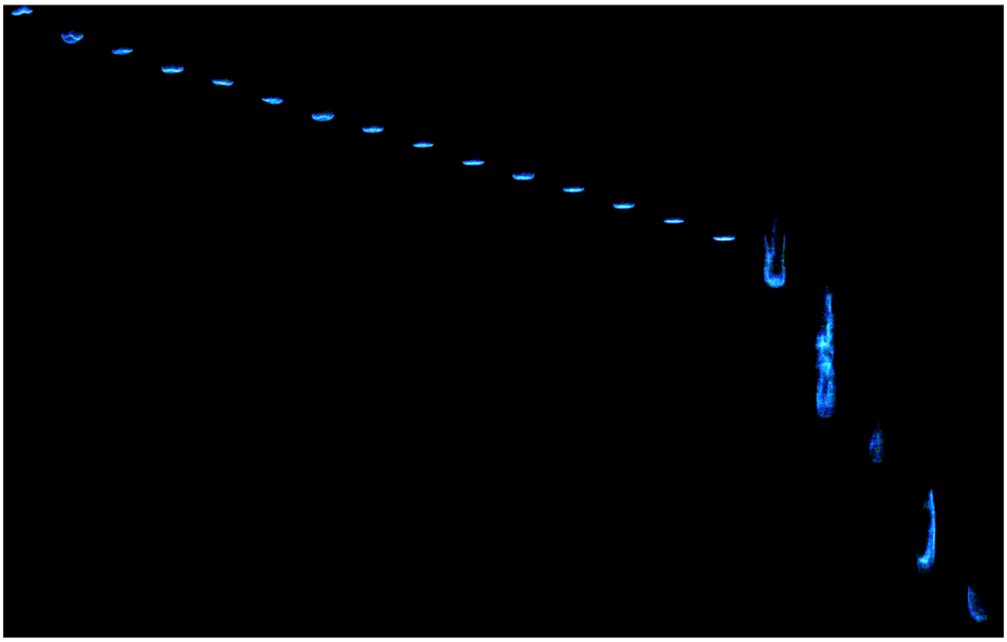

Figure 10-5 1.4 Methane without Hydrogen.

10.5 Camera Spectrum Setup

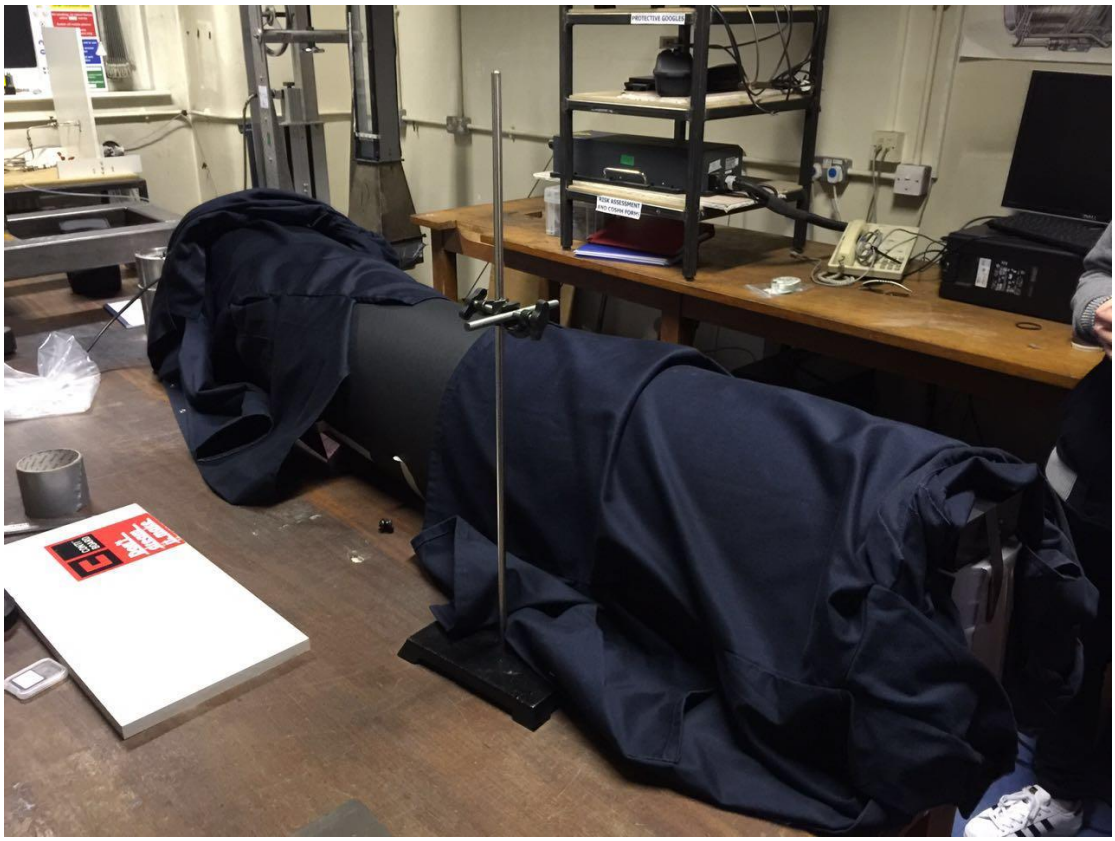

Figure 10-6 Setup of Spectrum testing

10.6 Real Experiment Rig for Chapter 7

Figure 10-7 Real experiment rig photo.

Figure 10-8 Real experiment rig-2.